NUMERICAL MODELING OF ACCELERATED CHARGED PARTICLES BY MAGNETIC RECONNECTION IN SOLAR FLARES

A thesis submitted to the University of Manchester
for the degree of Master of Science
in the Faculty of Engineering and Physical Sciences

2012

By
MOHAMMAD HUSSEIN HUSSEIN
School of Physics and Astronomy

Contents

Word count: $\sim$ 35000

List of Tables

List of Figures

Abstract

In this thesis we introduce the fundamental theory leading to the occurrence of solar flares. Observations from different missions support theoretical postulates concerning the mechanism proposed for such events, "magnetic reconnection", where we illustrates its basic theory, and consider one of its most important consequences, "particle acceleration". DC electric field associated with magnetic reconnection is now widely studied as one of the primary processes of particle acceleration in solar flares. Individual particle trajectories and acceleration due to direct DC electric mechanism in solar flares are modelled here using two approaches. The first is the full particle trajectory approach by solving Lorentz equation of motion that fully describe particle's motion. To do so we wrote what we call the "Full Code" that solves numerically, using different methods, the Lorentz equation. The second approach, known by Guiding Centre Approximation (GCA) Theory, is widely used when particles behave adiabatically. For this approach we used an existing code called "GCA" to simulate particle trajectories. A full comparison is presented to show the applicability of the GCA theory and its efficiency and when it can be used. Both approaches operate on an analogous model trying to simulate magnetic reconnection leading to the formation of a current sheet where particles are primarily accelerated and gain sufficient energy allowing them to be ejected to the outer space or come back to the Sun's surface. We consider the 2-Dimensional MagnetoHydroDynamic "MHD" model generating data files for background fields which serve as an input for our particle trajectory codes. We extract some limitations for important parameters such as mass-to-charge ratio and grid size and perform experiments at different locations at the current sheet (at the centre, far away from the centre, and at magnetic islands) to fully discuss differences between the 2 approaches. This coupling between particle trajectory models and data on grid arising from finite difference models is studied numerically and analytically. Different numerical methods, relativistic effects, analytical configurations, particle specie and mass effects and some others are taken into account.

University of Manchester,
Mohammad Hussein
Master of Science
NUMERICAL MODELLING OF ACCELERATED CHARGED PARTICLES BY MAGNETIC RECONNECTION IN SOLAR FLARES
03 September 2012

Declaration

No portion of the work referred to in this thesis has been submitted in support of an application for another degree or qualification of this or any other university or other institution of learning.

Mohammad Hussein

Jodrell Bank Centre For Astrophysics

Alan Turing Building

The University of Manchester

Manchester

M13 9PL

U.K.

Supervisor : Prof. Philippa Browning

Advisor: Dr. Benjamin Stappers

Copyright

The Author

The author obtained a B.Sc. degree in General Physics at the Lebanese University, graduating in July 2011. In September 2011 he began studying for an M.Sc. by Research in Astronomy and Astrophysics at the Jodrell Bank Centre for Astrophysics, University of Manchester. The results of this work are presented in this thesis.

Acknowledgements

First and foremost, before thanking any creature, I should thank our great creator "**God (Allah)**" for all his support, care, and mercy. In all that lonely nights, he was my companion directing me to the truth. Second to thank, my inspiration, "**the Redeemer (Al-Mahdi)**" who is the guider for all my life and to whom I dedicate this humble work.

I would like deeply to thank Dad for his unlimited emotional and financial support, my mum for just being as she is, my lovely brother who sweat to let me complete my studies, and my whole family for always believing in me.

I am very grateful for my supervisor, **Prof. Philippa Browning**, for her support, expert guidance, and comments. I really enjoyed being a member of her group and like her intelligent way of supervision who teaches me how to be a beginner researcher. Many thanks for **Dr. Mykola Grodovskyy** for his patience on my "just one more question" emails and meetings. To **Adam Stanier** I would say that it was going to be very very difficult to finish this thesis without your unbelievable help. I would not expect in my life to meet a person who could answer all my endless questions at any time and under any situation in a perfect way as you always did. I would like also to thank all the staff and students at JBCA especially M.Sc. students for our funny moments.

Finally, thanks to "**Hamza**" who draws all that smiles on my face, who made me really enjoy my stay here in the U.K. I would never ever forget all our funny going outs, our non-eatable homemade food, our long long conversations, and our brotherhood promises to each other. You really taught me what does friendship means.

List Of Abbreviations

HXR: Hard X-Ray

SXR: Soft X-Ray

EUV: Extreme Ultra Violet

HXT: Hard X-Telescope

SXT: Soft X-Telescope

SOHO: SOlar and Heliospheric Observatory

TRACE: Transition Region And Coronal Explorer

RHEESI: Reuven Ramaty High Energy Solar Spectroscopic Imager

SDO: Solar Dynamics Observatory

EVE: Extreme ultraviolet Variability Experiment

STEREO: Solar TErrestrial RElations Observatory

EM: Electro-Magnetic

CME: Solar Mass Ejection

SEP: Solar Energetic Particles

PIC: Particle In Cell

MHD: MagnetoHydroDynamics

GCA: Guiding Centre Approximation

2D: 2-Dimensional

3D: 3-Dimensional

RK4: 4th order Runge-Kutta numerical method

A-B4: 4th order Adams-Bashforth numerical method

§: section, subsection, or sub-subsection

Science without religion is lame. Religion without science is blind.

Albert Eistein

For the Redeemer

Al-Mahdi

869-Present

Chapter 1

Introduction

Solar flares are the most energetic explosions in our solar system. They seem to be far away events, but they can damage satellites and even ground based technology and power grids as they generate electromagnetic radiation and accelerate particles (ions and electrons) to very high energies and relativistic speeds influencing the atmosphere of our Earth. Much research has explored the hidden features of flares and the particle-energising mechanisms. Magnetic reconnection is the most likely candidate for such a mechanism. Magnetic loops stretching from the inner to the outer surface of the Sun, for millions of meters in the corona, come close to each other under the influence of plasma and foot-point motion to experience reconnection. While they are reconnecting they form a very narrow current sheet of high electric field at the centre. This current sheet has been an issue of debate for a long time concerning its shape, length scale and how it may energise particles to the extent they become non-thermal and emit radiation in the hard X-ray spectrum.

1.1 The Corona

As the events of this project ”solar flares and particle acceleration” occur in this region of the Sun, it is important first to describe some features and characteristics about the solar corona.

The solar corona (Figure 1.1) is the upper atmosphere of the Sun which extends

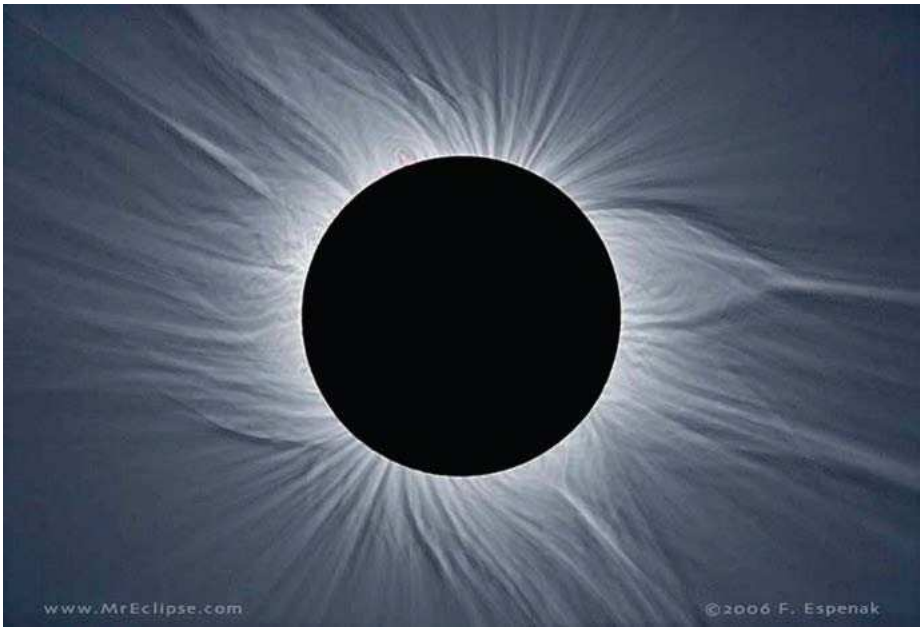

Figure 1.1: The solar corona at the total eclipse of 26 February 1998 observed from Oranjested, Aruba extending deeply to the space and showing beautiful bright fine rays (Lang, 2000).

to millions of kilometres into space. It is characterised by a high temperature 1-2 MK, while the photosphere which is at the Sun's surface has a temperature of $\sim$5800K; it remains until now an unsolved problem in astrophysics to explain what causes the corona to be as hot as it is. The corona has a low density $\sim 10^{14}$-10^{15} m^{-3} compared to 10^{23} m^{-3} for the photosphere. It consists entirely of plasma and can be seen during a total eclipse or by using a corona-graph to obscure the light from the Sun's photosphere. It mainly emits in X-rays and Extreme Ultra Violet (EUV) with an optically thin layer where its radiation does not penetrate the Earth's atmosphere (Mullan, 2010). Many solar space observations have been taken to discover the hidden features of the corona and detect its radiation. These observations were taken by SOHO (1995), TRACE (1998), RHESSI (2002), Hinode (2006), and Stereo (2006). One of the most important characteristics of the solar corona are the loops known as "coronal loops" (Figure 1.2). These loops extend from the photosphere to the corona. They are mainly generated at magnetic Active Regions where sunspots are located and are the main reason for the occurrence of flares and Coronal Mass Ejections (CMEs).

The well known coronal heating problem is summarised by the following question.

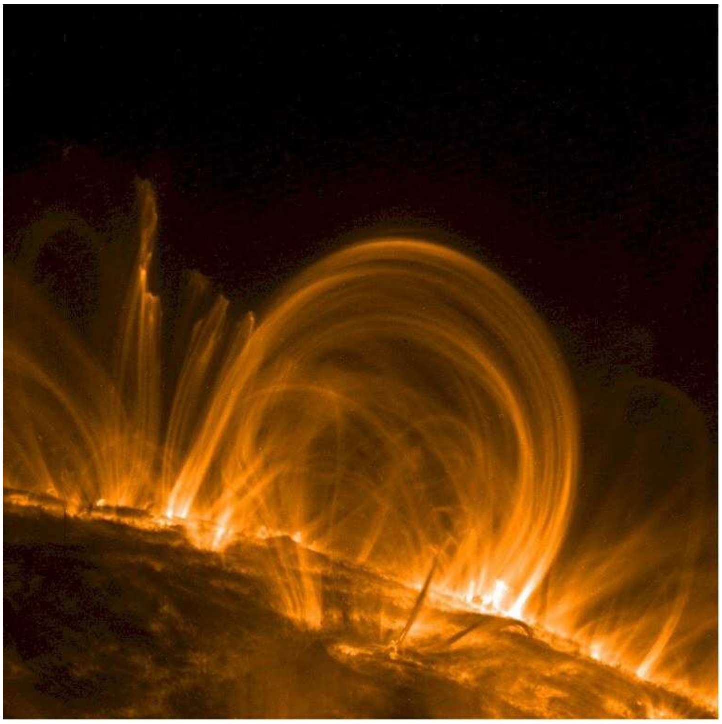

Figure 1.2: Extreme UV image at a wavelength of 17.1 nm from (TRACE) for Coronal loops extending to millions of meters from the Sun's surface to the corona ($http://www.nasa.gov/images/content/113853main\_trace4\_lg.jpg$).

"How does the solar corona reach to temperatures of millions of degrees Kelvin?" Two main mechanisms were proposed to answer this question. The first is by wave heating where several types of waves, such as magneto-acoustic waves and Alfven waves, carry energy from the solar interior to the solar corona crossing the different solar layers. The second mechanism, which will be discussed later, is magnetic reconnection where coronal loops reconnect, releasing their hidden magnetic energy to the outer corona. One of the features suggesting this theory is the existence of small scale flare events known as micro-flares. These occur in the lower corona at a height of 200 km from the photosphere and releasing up to 10^{22} J of magnetic energy (Jess et al., 2010). Micro-flares occur more frequently than large flares, that's why they could account for the energy needed to heat the corona although even smaller and more frequent events known as "nano-flares" are required to dominate the heating rule (Parker, 1988). Also a combination of the above two mechanisms is proposed. For more information about solar corona and solar Active Regions refer to Güdel (2007), Nakariakov & Verwichte (2005), Borrero & Ichimoto (2011), Mullan (2010) and references therein.

1.2 Solar Flares

Solar flares (Figure 1.3) are the most dramatic, energetic events in our solar system. They release up to $\sim 10^{26}$ J of stored magnetic energy in a very small period of time. That time varies between one flare and another from a few seconds to a few minutes and could in some cases (long duration events) extend to hours. The spatial size also varies from one flare to another. In small events it is less than 10^4 km whereas in large ones it reaches 10^5 km (Shibata & Magara, 2011). The size of a flare together with its duration and amount of released energy are all related. The huge energetic release causes the plasma in the corona to be heated up to tens of millions of degrees Kelvin and accelerates particles (ions and electrons) to very high energies and relativistic speeds (a few GeV in the case of ions, and tens of MeV in the case of electrons). A great fraction of flare energy goes to such acceleration processes (up to 50% in some flares). These high energy particles may be emitted into space or reach the chromosphere when they are sent downwards, producing electromagnetic radiation along the whole spectrum from radio to gamma rays (Lang, 2000).

Flares were originally discovered in white light by R.C. Carrington and R. Hodgson in September 1, 1858 (Carrington (1859); Hodgson (1859)). Later on, when filters and detectors where invented, H_α, coronal radio, and X-ray emissions were observed, demonstrating that these events are coronal phenomena and not a chromospheric one as was thought for a long time.

Mainly solar flares occur in solar magnetically Active Regions (AR), above sunspots where magnetic fields are so concentrated and complicated in structure. Magnetic fields were first discovered on the Sun by Hale (1908) and from then theoretical studies developed the relation between them and solar flares. The notion of neutral points were first reported by Giovanelli (1946) as where energy release occurs and the theory of magnetic reconnection as a process related to flares was first pointed out by Hoyle (1949). Zwaan (1985) reported that the Sun's interior is

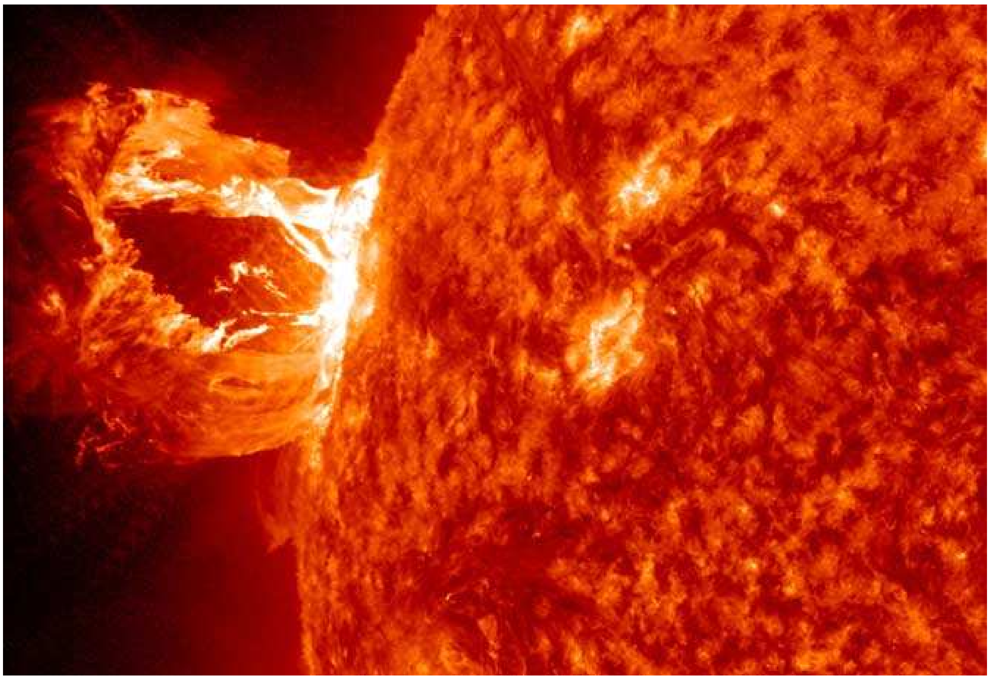

Figure 1.3: A fine Solar Dynamics Observatory (SDO) image of an erupting prominence (eruptive event) associated with a medium sized solar flare at the same time directed off the earth at the east limb (left side) of the Sun on April 16 2012. *http://www.nasa.gov/mission_pages/ sdo/multimedia/potw/index.html*.

a dynamo for magnetic fields where they cross the Sun's layers surrounded by high pressure plasma (Parker, 1979) resembling a twisted flux tube (Fan, 2009) to the outer surface and providing energy source for flares. The flare scenario begins when flux emergence starts and magnetic fields emerge to the surface carrying the interior magnetic energy. Electric current crossing magnetic fields (cross-field currents) enhance expansion, as it generates Lorentz forces, and causes part of the magnetic energy to be dissipated immediately. The remaining part of electric current flowing along magnetic field is force-free. An important coronal feature which helps magnetic energy to be stored is that the corona is a highly conductive medium. This inhibits field-aligned electric current dissipation, thus free energy builds up and serves as a reservoir for the coming event (Shibata & Magara, 2011). Of course this energy will not accumulate indefinitely but rather different postulated scenarios may interfere to release this tremendous stored energy. In fact a solar flare occurs when an instability or a loss of equilibrium, triggered by a specific mechanism to be explained later, suddenly takes place. Thus the system erupts causing an immediate release of magnetic stored energy and then relaxes to approach a potential field situation.

Pre-flare events take place before the onset of a flare and are known as precursors which are worth discussing. Magnetic flux tubes could interact with newly emerging bipolar regions or magnetic flux tubes triggering a flare (Heyvaerts et al. (1977); Martin et al. (1982); Feynman & Martin (1995)). Also, eruptive filaments are considered as primary precursors, here cool plasma emerge into the hot corona and due to several forces (e.g. magnetic pressure gradient force, magnetic tension, and gravitational force), filaments may lose equilibrium and erupt (Yan et al., 2011).

The most likely energy release process in flares is magnetic reconnection where oppositely directed magnetic field lines are pushed by plasma flow toward each other forming a narrow current sheet where they reconnect at an X-point (a neutral point or null point where magnetic field vanishes (Birn & Priest, 2007)). See § 2.1.2 for details about magnetic reconnection. Part of the released energy finds its way upward in the form of a plasma "blob" called a plasmoid. This process is important to our research as particles are accelerated to become non-thermal and energetic. This allow them to leave the Sun and make their way toward us or to the interplanetary space (Ramaty & Murphy, 1987). Some particles are also accelerated downward to the Sun where they hit the dense chromosphere at the foot-points emitting Hard X-Rays (HXRs) due to Bremsstrahlung, that's why foot-points are HXR sources. This also causes the chromosphere to be heated and to emit H_α radiation and in turn to fill the loops by dense super-hot plasma (20-40MK) emitting Soft X-Ray (SXR) (thermal emission), this process is known as "evaporation" ((Birn & Priest, 2007); (Lang, 2000)). In some flares coronal HXRs were observed above coronal loops which could be interpreted as thermal Bremsstrahlung from a thin target (see Meroun Thick Target Model for Brown (1971)). Figure 1.4 demonstrates almost all flare processes. A point worth mentioning here is the existence of a physical relation between coronal mass ejections CME's and solar flares. CME's are large-scale eruption of solar mass to outer space with a huge amount of plasma (up

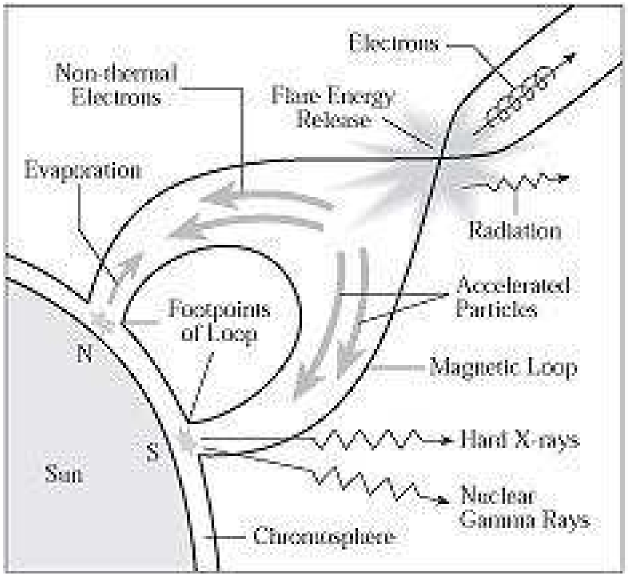

Figure 1.4: A schematic drawing of different processes of a solar flare model where energy is released at the X-point generating radio burst waves and particles are accelerated either up to space or down hitting the chromosphere and releasing HXR and γ-rays leading to the evaporation process (Lang, 2000).

to 10^{10} tons). Several flare events are observed when CMEs occur which could be interpreted as flares being sub events of these huge eruptions especially as magnetic loops with solar radius sizes are observed moving away with high velocities 30-2500 $km\ s^{-1}$ from the Sun causing shock waves to interfere in CME events (Yashiro et al., 2004).

Flares or eruptive events can be decomposed and set into many different categories. Mainly we consider 3 types of events which are well known, Long Duration Flares, Giant Arcade, and Impulsive Flares. Long duration flares are characterised by their cusp-shaped loop structure accompanied by coronal mass ejection creating a helmet streamer-like configuration which give a clue that a current sheet is formed [Lang (2000); Tsuneta et al. (1992a); Tsuneta (1996)]. Magnetic reconnection is proposed to occur due to the increase in the separation between the foot-points. The temperature is observed to increase near the cusp-shaped loop (Veronig et al., 2006).

Some observations have revealed the formation of giant arcades as also having a cusp-shaped loop, however these are much larger spatially than long durational flares and mostly associated with a filament disappearance as such they are not considered as typical flares. Their temperature also increases near the cusp-shaped loop but their soft X-ray emission is low, and their time scale and released energy are different from that of a typical flare due to the difference in magnetic strength (Tsuneta et al. (1992b); McAllister et al. (1992); Watanabe et al. (1992); Shiota et al. (2005)). Additionally, giant arcades experience what is called *dimming* where SXR flux decreases with time outside the loops (Sterling & Hudson, 1997) due to field lines eruptions (Harra & Sterling, 2001), or inflow of plasma toward the current sheet so decreasing the density in its surrounding (Tsuneta, 1996).

Impulsive flares have a simple loop structure emitting in SXR and they do not show any cusp-shaped structure. Some observations show that such flares have an extra X-ray source on top of the SXR loop emitting in hard X-ray and behaving like HXR sources at the foot-points [Masuda et al. (1994); Masuda et al. (1996)]. Shibata et al. (1995) pointed out that magnetic reconnection may occur in impulsive flares outside SXR loops associated with plasmoid ejection.

Finally, as flares are linked to solar active regions which themselves vary in an 11-year Sun cycle from minima to maxima, the frequency of flare occurrence and strength vary within this cycle. At solar maxima, several flares eruptions may happen per day, while it decreases to one per week at solar minima.

1.3 Origins Of Electromagnetic Radiation

Solar flares cause the emission of electromagnetic (EM) waves across the whole spectrum (from radio to gamma rays). In flares, particles are accelerated to different energies within the same species (ion or electron) according to their position when the flare is triggered. This difference causes particles to emit at different wavelengths when interacting with the outer space or with the chromosphere layer. There are 6 main types of emission as follows:

1. Radio bursts: due to energetic and eruptive characteristics of a solar flare like electrons accelerated to modest energies of a few keV (Type I Bursts), shock waves with an outward motion at about a million meters per second

(Type II Bursts), beams of electrons thrown out from the Sun with kinetic energy of 10 to 100 keV (Type III Bursts), synchrotron emission from energetic electrons trapped within magnetic clouds (Type IV Bursts), and some other mechanisms.

2. Microwaves: due to synchrotron radiation caused by gyrating high energy electrons around magnetic field lines.

3. H_α: due to the impact of high energy particles accelerated at the X-point with the dense chromosphere.

4. SXRs: due to hot plasma in the chromosphere filling the coronal loops after the impact (thermal radiation).

5. HXRs: due to deceleration of high energy particles, (non-thermal) at the chromosphere (free-free emission) and from coronal sources.

6. Gamma-rays: due to collision of high energy protons and ions (nuclear reactions) (Lang, 2000).

1.4 Flare Observations

Flare observations have passed through different stages influenced by the technological progress. After the invention of H_α filters, Moreton (1964) reported the variations of source sizes, ejection of plasma blobs into interplanetary space, and blast waves. Later, Hey (1983) revealed the presence of non-thermal electrons in the corona using meter wave radio emission first detected in 1942. The hard X-ray instruments were a break-through in flare observations and Peterson & Winckler (1959) were the first to detect HXR emissions during a flare in 1958. Brown (1971) noted that the emission gave a clue that energetic particles hold a substantial amount of flare energy. Continuing, technological progress allowed gamma-ray lines to be discovered for heavy nuclei and energetic protons (Chupp et al., 1973). The final flare scenario was established when the full spectrum was observed with millimetre, Extreme Ultra Violet (EUV), and soft X-ray emissions noting that flare heat the plasma in coronal loops to emit thermal radiation.

From an observational point of view, a flare can be decomposed into 3 main phases according to the type and strength of emission (Figure 1.5). These phases are the early or pre-flare phase, impulsive phase, and gradual decay phase.

1. Early phase: It is often interpreted as preheating, where SXR and EUV emissions are seen to increase gradually due to the plasma being heated slowly. No foot-point HXR and γ-ray emissions are detected above background, but the interesting feature is the detection of coronal HXR emission from a coronal HXR source above the SXR loops, which till now is not fully understood (Battaglia et al., 2009).

2. Impulsive Phase: This is the main flare phase where acceleration of particles occurs and energy is released. HXR, microwave-millimetre waves and γ-rays increase impulsively in spiky bursts lasting for a few or tens of seconds due to Bremsstrahlung, gyro-synchrotron emission (1 GHz to beyond 100 GHz), and ion's nuclear reaction respectively. Non-thermal electrons show a power law spectrum, with some electrons being accelerated to the MeV range. HXR footpoint sources at chromosperic heights are detected for all flares at this phase (Hoyng et al., 1981). SXR emmision continues to rise due to the evaporation process from the super-hot thermal plasma (20-40MK).

3. Gradual decay phase: This is the post-flaring phase, where everything begins to return to a simpler configuration. HXR and γ-ray emission decay exponentially with a time constant of minutes. SXR emission reaches a peak value and after that decays exponentially very slowly and can be detected in the next day following the flare. Particles continue to be accelerated by different methods e.g. direct DC electric and magnetic reconfiguration process, plasma ejection, and shock waves emitting radio bursts in meter waves [(Hudson, 2011); (Lin, 2006)].

Observations of solar flares are essential to diagnose the different features of

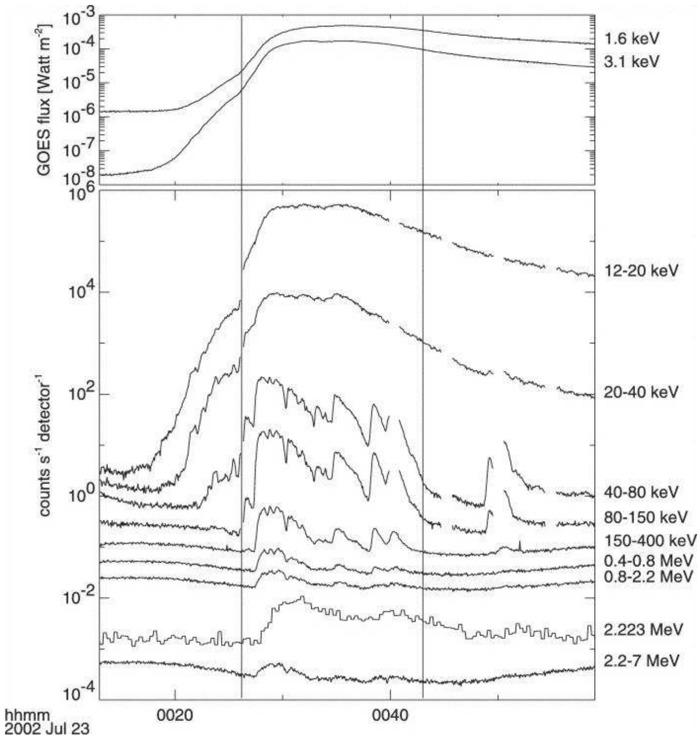

Figure 1.5: SXR, HXR, and γ-ray count rates by RHESSI for the 2002 July 23 flare showing the 3 different phases of a flare [phase 1:$\sim$00:18 to $\sim$00:27 UT, phase 2:$\sim$00:27 to $\sim$00:43 UT, and phase 3:$\gtrsim$00:43 UT] as discussed in §1.4 (Lin, 2006).

flares. Different spacecraft are used for such observations like “Hinode”, “Yohkoh” with its HXR and SXR telescopes, HXT and SXT, (but they are out of service now), “SOHO”, “STEREO”, “SDO” with its “EVE” instrument for EUV detection, and the most powerful capabilities spacecraft “RHESSI” (see §2 in Lin (2006) for details on RHESSI structure and capabilities). This spacecraft can detect emission from flares and make spectroscopic images for HXR and γ-ray which are produced from high energy electrons and ions respectively. Such observations have revealed new facts and surprises. Examples of these new features are coronal sources that appear before chromospheric foot-point HXR emission, the relation between flares and CMEs does not seem to be in correlation at major flare acceleration sites, electrons and ions may be accelerated and ejected at different separatrices, and magnetic topology varies from small to large events (Benz, 2008). Observations now go deeply into flares and locate energy release sites allowing us to test our main interest in this project, particle acceleration theory together with the processes behind such events. It is now generally accepted from observations that reconnection is the trigger of energy release in flares but what remains uncertain is how such a release scenario converts a high proportion of the released energy into non-thermal particles?

Solar flares are now observed at a wide range of wavelengths from decametre radio to gamma-rays. The HXR or the non-thermal emission which have a photon energy range greater than 12 KeV and less than 500 KeV is caused by the free-free collision of high energy and fast electrons with ions known as Bremsstrahlung. Measurements of the time of flight support the idea that particles are accelerated near the X-point above the SXR loops as shown in Figure 1.4. For large flares, and deducing from the HXR fluxes, 10^{36}-10^{37} electron s^{-1} must be accelerated into the non-thermal energies which means that the coronal loops will be depleted from electrons in a timescale of seconds which could be regarded as a "Number Problem" (Birn & Priest, 2007).

Thermal emission or SXR which have an energy range from 1.2 to 12 KeV are also observed due to the hot thermal plasma filling the loops in the evaporation phase. The X-ray observed spectrum can be inverted to produce the source-averaged spectrum of accelerated electrons producing such emission (Figure 1.6). The spectrum shows an exponential form for the thermal emission and a broken power law for the non-thermal emission (higher energies) (Birn & Priest, 2007).

Accelerated protons and α-particles undergo collisions with other heavy ions which are excited to higher nuclear state. Of course after any nuclear excitation, a rapid de-excitation happens releasing photons detected as γ-ray emission of energies between 4-7 MeV. There are a lot of heavy ions that present in the Solar atmosphere as Oxygen, Carbon, Neon, Silicon, Magnesium, and Iron. Neutrons produced in nuclear reactions lose energy and slow down after a long time, so that they can be captured by protons (^{1}H), forming deuterium (^{2}D) at an excited state. When de-excited, deuterium release energy detected as γ-rays at a line of 2.223 MeV. Pair annihilation also occurs between positrons and electrons producing 2 γ's at 0.511 MeV (See table 1.1) (Lang, 2000).

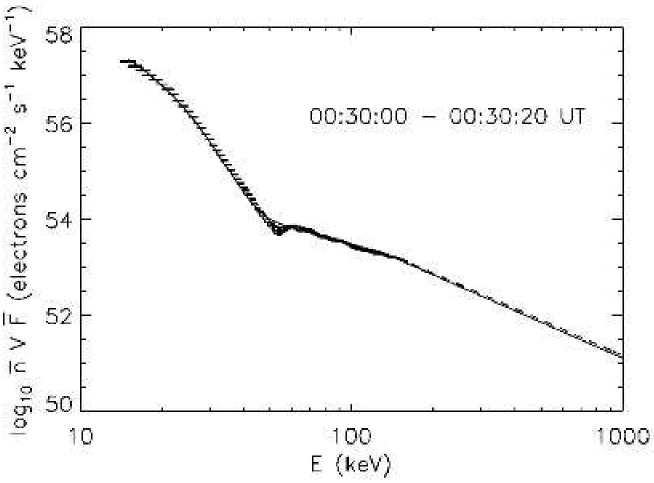

Figure 1.6: Electron energy spectrum of the July 23, 2002 flare upon inversion its Bremsstrahlung spectrum showing a Maxwellian distribution for the thermal part, where most of the particles are within this region, and a power law for the higher energy particles extending to MeV (Piana et al., 2003).

Element	Energy(MeV)
$e^+ + e^-$	0.511
$^2H \equiv {}^2D$	2.223
^{12}C	4.438
^{16}O	6.129, 6.917, 7.117
^{7}Be	0.431
^{7}Li	0.478
^{14} N	5.105
^{20}Ne	1.634
^{24}Mg	1.369
^{28}Si	1.779
^{56}Fe	0.847

Table 1.1: Most important gamma-ray lines from solar flares (Lang, 2000).

1.5 Aims and Outline

A Test particle model used to calculate particle trajectories using magnetic and electric fields distributed in a finite grid is studied in our work. A Test particle is an idealised model of an object whose physical properties are assumed to be negligible except for the property being studied, which is considered to be insufficient to alter the behaviour of the rest of the system. This dissertation aims to compare the two test particle approaches, Full Trajectory and Guiding Centre to discuss where they coincide and where they do not (see § 2.3.1 for details about the test particle model and its different approaches). This will allow us to say if it is worthwhile to study particle trajectories using the approximate guiding centre theory. We aim to find limitations of numerical trajectories when using field values given in discrete grids. We also compare different numerical methods for solving differential equations for particle trajectories. Relativistic effects and how they influence on particle motion and when they are important are also one of our aims. We wrote the full trajectory code which first is tested against analytical solutions and later on compared with an already written GCA code for analytical and numerical fields.

In the next chapter we will introduce some basic MHD theory and the test particle approach that serves as a review of previous work in this context. Chapter 3 describe our own full trajectory code and the testing procedure, also in this chapter we study the particle drift theory from both theoretical and numerical points of view and compare results. In chapter 4 we use analytical field forms distributed in a discrete grid and discuss the results. The full comparison between the 2 approaches for realistic models and numerical MHD data is presented in chapter 5. Finally we end our thesis with a conclusion chapter and a section about further work that could be done in future.

Chapter 2

Background Theory

2.1 Basic Theory of MHD 2D Reconnection

2.1.1 MHD Theory and Numerical Application

Magnetohydrodynamics (MHD) theory treats the plasma as an electrically conducting fluid filled by magnetic field lines where it interacts with them. The MHD equations are a set of nonlinear equations describing 15 quantities on the full system: the velocity of a plasma fluid element, $\boldsymbol{v}$; the magnetic field, $\boldsymbol{B}$; the current, $\boldsymbol{J}$; the electric field, $\boldsymbol{E}$; the density, ρ; the pressure, P; and the temperature, T. These equations are derived from a combination of fluid mechanics and Maxwell's equations. Some important parameters in MHD theory are plasma beta (β) measuring which dominates, thermal or magnetic pressure, magnetic Reynolds number (R_n) giving information about resistivity and Ohmic dissipation effect, Alfven speed (V_A) is the speed at which magnetic information propagates within the plasma, Alfven time (t_A) is the timescale of Alfven wave propagation, diffusion timescale τ_d, and Lundquist number (L_u) defined as the ratio of the 2 mentioned timescales. Equations for these quantities are presented in Appendix A.1. For a complete introduction about MHD theory, see Priest & Forbes (2000).

We will work out the estimated values for β, R_n, τ_d, V_A, t_A, and L_u for coronal plasma by importing typical coronal values of B (magnetic field), n_e (electron density), T (temperature), and L_0 (length scale). Our choice of values is as follows: B

= 300 Gauss (1 Gauss = 10^{-4} Tesla), $n_e = 10^{15} m^{-3}$, $T = 1.5 \times 10^6$ K, and $L_0 = 10^7$ m.

This gives the pressure, $p = 2n_e k_b T = 0.0414$ Nm^{-2}, and $B = 300 \times 10^{-4} = 0.03$ Tesla, so $\beta = 2\mu_0 p/B^2 = 1.16 \times 10^{-4}$ which is a very small number as expected (the corona is a low beta region as magnetic pressure dominates). Next we derive the diffusivity, η, in order to calculate R_n. It is given as $\eta = \frac{1}{\mu_0 \sigma}$ where σ is the conductivity given as $\sigma = 7 \times 10^{-4}\ T^{3/2}$ so at our given temperature $\sigma = 1.29 \times 10^6$ Ohm^{-1}m^{-1}, thus $\eta = 0.618$ Ohm.m^2. This gives $R_n = 1.61 \times 10^{11}$, also as expected a large number (low resistivity effects). Now $\tau_d = L_0^2/\eta = 1.6 \times 10^{14}$ s, which is $\sim$ 5 million years and hence Ohmic diffusion could be neglected given that we are in a high conductive case ($R_n \gg 1$), but it is not always the case. In order to calculate V_A, we calculate the density $\rho = n_e m_p = 1.67 \times 10^{-12}$ kgm^{-3}. Following from theory, $V_A = \sqrt{B^2/\mu_0 \rho}$, so $V_A = 2 \times 10^7$ ms^{-1} and $t_A = L_0/V_A = 0.5$ s. Finally $L_u = \tau_d/t_A = 3.2 \times 10^{14}$ as expected also a large number.

2.1.2 Magnetic Reconnection

Magnetic reconnection is a process that occurs in highly magnetised plasma by changing the magnetic topology of the field lines by breaking some and reconnecting others of opposite polarity causing stored magnetic energy inside and outside the current sheet to be converted to thermal and kinetic energy (Schrijver & Siscoe, 2009). Jain et al. (2005b) discussing forced reconnection states that "reconnection occurs when a sheared force-free field is perturbed by a slow disturbance (pulse) at the boundary which is representative of the solar corona where the reconnection is induced by the photospheric motions", or newly emerging flux, or by any kind of coronal disturbances such as coronal waves. In the simplest model magnetic field lines are straight and divided into 2 sets of opposite polarity. Electric current crossing magnetic field lines (cross-field current) is dissipated under the action of a finite value of resistivity causing Ohmic dissipation near the current sheet. This sudden perturbation causes a change in the magnetic topology where field lines relax to lower energy states and are driven by plasma flow to an X-point (where magnetic field vanishes) and thus reconnection takes place. An important consequence of reconnection is the generation of strong convective electric field in the sheet surrounding, which accelerate particles.

Magnetic reconnection can either be steady or unsteady and driven (forced) or spontaneous. Two main steady models were proposed, the Sweet-Parker (1958) and Petschek (1964) models which are presented below. Unsteady reconnection known by "Tearing Mode" or "Tearing Instability" is related to locally enhanced resistivity and non-uniformity introduced to the current sheet associated with magnetic islands coalescence. Spontaneous reconnection occurs due to resistive MHD instability like tearing instability. In our simulations we use driven-type reconnection known as "Forced Reconnection" which is presented below.

Sweet-Parker model

Figure 2.1 illustrate the geometry for Sweet-Parker model in which the magnetic diffusion layer has the same length as the global external length scale. Assuming incompressible flow and neglecting viscosity, Sweet and Parker (1958) determined the inflow rate as:

$$V_{in} = V_A L_u^{-1/2} \tag{2.1}$$

and the outflow as:

$$V_{out} = V_A \tag{2.2}$$

Reconnection is associated with an electric field perpendicular to the current sheet. This electric field in 2-dimensional steady-state models is uniform in space in the invariant direction influencing the rate of reconnection which measures the magnetic flux reconnecting per unit time as this rate is normalised to the characteristic electric field defined as, $E_0 = v_A B_0$, where B_0 is the characteristic magnetic field. Defining the Alfven Mach number M_{Ae} (rate of reconnection) as:

$$M_{Ae} = \frac{V_{in}}{V_{out}} = L_u^{-1/2}, \tag{2.3}$$

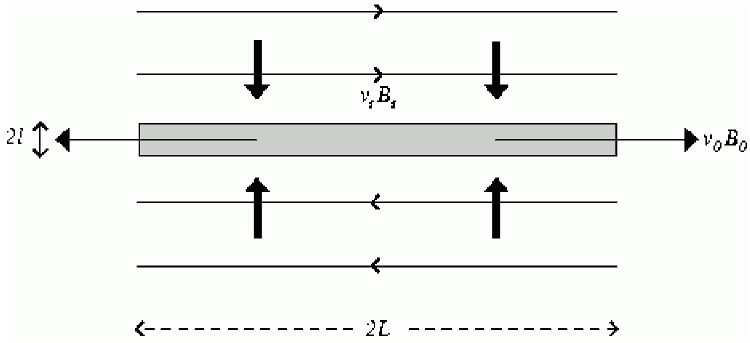

Figure 2.1: Sweet-Parker reconnection model showing a wide diffusion region (shaded) where inflowing plasma (thick arrows) drifte to the current sheet with low velocities $V_A L_u^{-1/2}$ and outflows (long arrows) with high velocities V_A (Priest & Forbes, 2000).

the typical coronal value for Lundquist number is of order 10^{14}, so $M_{Ae} = 10^{-7}$, and the reconnection time would be of orders $10^8 - 10^9$ s. From observations, the time scale of a flare is $10^2 - 10^4$ s which is much smaller than the reconnection time, so how could a fast energy release occur with such model (Schrijver & Siscoe, 2009)?

Petschek Model

This model (Figure 2.2) has a higher reconnection rate by dramatically reducing the length of the current sheet. Also Petschek(1964) added two outward slow shocks that accelerate and heat the plasma. Assuming current-free inflow magnetic fields and no sources of field at large distances (Schrijver & Siscoe, 2009), leads to an increase in the reconnection rate such that:

$$M_{Ae} = \frac{\pi}{8ln(L_u)}, \tag{2.4}$$

giving values between 0.01-0.1 for the case of the corona (Petschek, 1964). The reconnection time for such a model is comparable with flare time scale. Forbes & Priest (1987) later on extended the model and pointed out that speed of reconnection is controlled by the spatial pattern of flow (converging or diverging) in the inflow region. With the aid of numerical simulations, it was shown that Petschek's model is likely to occur. Sato & Hayashi (1979) showed using forced reconnection that the Petschek model occurs when the resistivity in the current sheet is locally

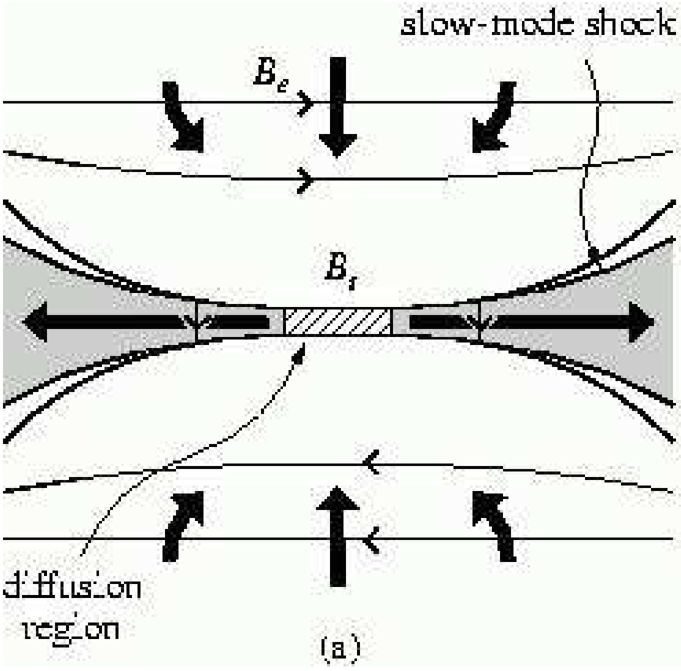

Figure 2.2: Petschek reconnection model with a very narrow diffusion region (central shaded region). 2 slow-mode shocks (the other 2 shaded regions) are added by Petschek that heat and accelerate the plasma with other assumptions leads to a higher reconnection rate (Priest & Forbes, 2000).

enhanced. Biskamp (1986) perform simulations with a uniform resistivity distribution and showed that in this case Petschek model does not arise, but instead Sweet-Parker is formed. Ugai & Tsuda (1977) and Scholer (1989) reproduce using spontaneous reconnection (no plasma inflow toward the current sheet to produce perturbations) the Petschek model by locally enhancing resistivity in the current sheet, thus locally enhanced resistivity is essential for the Petschek model to occur.

Forced Reconnection

Hahm & Kulsrud (1985) proposed the forced magnetic reconnection model as a simple analytically tractable model of a reconnection event triggered by an external perturbation, which could be due to photospheric foot-point motions, newly emerging magnetic flux, or any type of coronal disturbance like coronal waves in case of coronal eruptive events. Initially an incompressible plasma in equilibrium with a magnetic field of uniform gradient in x-direction is considered. The domain is defined such that x $\in [-a, +a]$, where a is a constant, and conducting walls exist at the boundaries. The magnetic field is given by: $\vec{B} = B_0 x/a\,\vec{j} + B_T\,\vec{k}$, where B_0 and B_T are constants. The authors studied the time evolution of the magnetic field islands by perturbing the boundary surrounding the incompressible plasma with a transient-disturbance having spatial dependence of the form: $x = \pm(a - \delta cosky)$, where δ is the perturbation amplitude (see Figure 2.3). The amplitude of the boundary disturbances affects the size of the islands as well as the time scale for reconnection and island formation. they pointed out that, for sufficiently small perturbations, the tearing mode time scale applies and small islands are formed, whereas for larger perturbations, nonlinear time scales operate with larger islands forming. There exist two natural equilibrium states which are noticeably different by their behaviour near the resonant surface i.e. the centre of system where the current sheet is located. Equilibrium (I) contains surface current (a discontinuity in magnetic field) on the resonant surface, while equilibrium (II), which has lower energy than (I), possesses magnetic islands and has finite current density. The whole process can be decomposed into four time phases, A, B, C, and D when considering the case of small boundary perturbation with tearing mode time scale as postulated by Hahm & Kulsrud (1985). Phase A corresponds to the ideal MHD theory where after the initial change in boundary occurs, the plasma behaves ideally approaching equilibrium (I). Phase B corresponds to ideal MHD with small resistive corrections, where magnetic field lines begin to reconnect and build up a concentration of current near the resonant surface, but the dynamics of the plasma are unaffected by the resistivity. In phase C (the major phase), finite resistivity is applied and reconnection of flux across the resonant surface occurs, affecting plasma dynamics; thus a full resistive theory and tearing mode analysis with non-constant perturbed flux function is invoked. As a result, magnetic islands start to form. Reconnection proceeds for a relatively long time, decreasing the surface current, while the perturbed flux function simplifies to a constant and the plasma approaches equilibrium (II). These are the features for the final phase, phase D, concluding the evolution of the reconnected flux. Figure 2.4 demonstrates the amount of reconnected flux with time during the four phases. Vekstein & Jain (1998) investigated forced magnetic reconnection in a

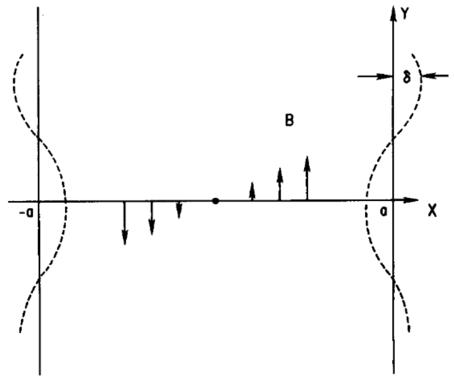

Figure 2.3: Rapid perturbation at the boundary caused mainly by photospheric motions leading to topological changes in magnetic field, thus triggering reconnection and then approaching equilibrium state (Hahm & Kulsrud, 1985).

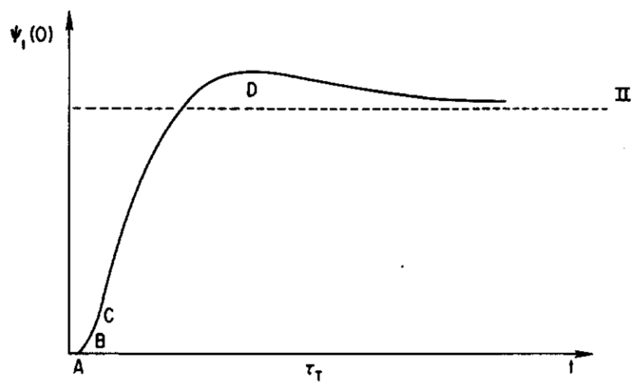

Figure 2.4: The amount of reconnected flux, $\psi_1(0)$, during the four phases of reconnection. The dashed line represent equilibrium (II) which is stable to the tearing mode.

sheared force-free magnetic field. They found that for such field, the response for external perturbation becomes very strong near the marginal stability of the tearing mode, so that any weak perturbation can cause high relaxation. Figure 2.5a shows deformation of force free magnetic fields in an ideal MHD equilibrium corresponding to phase B, and figure 2.5b corresponds to phase C where reconnection takes place and magnetic islands are formed.

2.2 Particle Motion in Electric and Magnetic Fields

One of the main issues in plasma physics is to understand how particles move in electric and magnetic fields with different configurations. The basic equation of

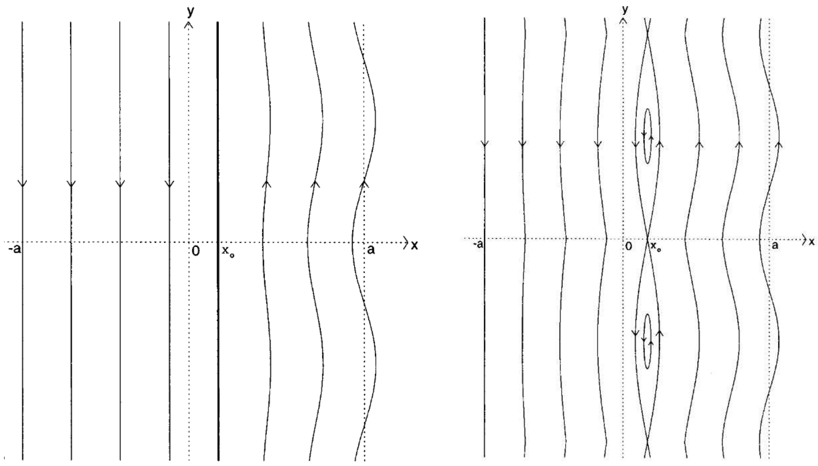

(a) Ideal MHD state deforming field lines preparing the system for reconnection. The current sheet is located at $x = x_0$.

(b) Reconnection state associated with magnetic islands formation.

Figure 2.5: The main two states of evolution, ideal (a) and reconnected (b) (Vekstein & Jain, 1998).

motion is the Lorentz equation:

$$m\frac{d\mathbf{v}}{dt} = q(\mathbf{E} + \mathbf{v} \times \mathbf{B}). \tag{2.5}$$

We will present key points, therefore, for a full discussion there are many textbooks and review papers for example Chen (2010), Northrop (1966), Cary & Brizard (2009), and references therein.

2.2.1 Uniform E and B Fields

E=0

This is the simplest case, particles gyrate around the magnetic field lines in a harmonic motion with a cyclotron frequency ω_c given as:

$$\omega_c = \frac{|q|B}{m}, \tag{2.6}$$

so electrons gyrate more rapid than protons. The gyration radius (Larmor radius) r_l is given by:

$$r_l = \frac{mv_\perp}{|q|B}, \tag{2.7}$$

hence, an electron's Larmor radius is smaller than that of protons. Typical values of Larmor radius for particles can be calculated when their velocities are known. Thermal velocities for particles with mass m_i and temperature T_i can be calculated from the following equation:

$$V_{Ti} = \sqrt{\frac{3k_bT_i}{m_i}} \tag{2.8}$$

substituting for protons and electrons mass and with typical coronal temperature of 1.5×10^6 K, we get:

$$V_{Tp} = 1.92 \times 10^5 ms^{-1}$$

$$V_{Te} = 8.25 \times 10^6 ms^{-1}$$

using Equations 2.6 and 2.7 and setting $B = 300$ Gauss we get:

$$\omega_{cp} = 9.58 \times 10^3 rad.s^{-1}$$

$$\omega_{ce} = 1.75 \times 10^7 rad.s^{-1}$$

$$r_{lp} = 6.7cm$$

$$r_{le} = 0.15cm$$

Electrons and protons always gyrate in opposite directions as the Larmor radius depends on the particle charge as shown in Figure 2.6.

Finite E

The parallel component ($E_\parallel$) will accelerate particles along the field lines and perpendicular one ($E_\perp$) will generate the ordinary gyro-motion around **B**. A new term,

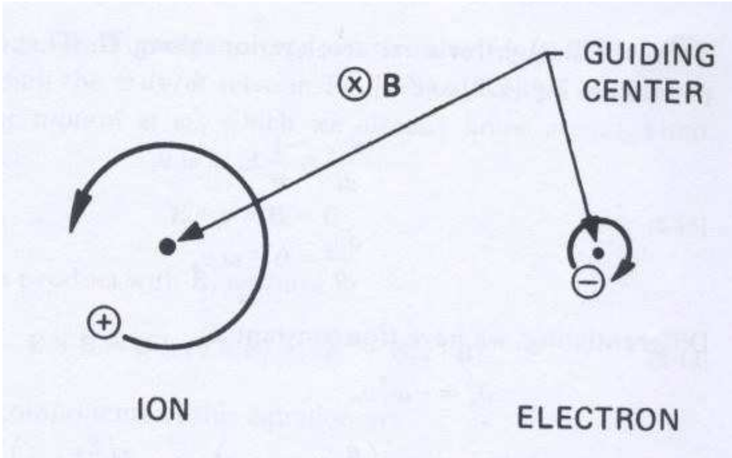

Figure 2.6: Particle motion in uniform B and E=0 fields where particles gyrate around magnetic field lines. Ions and electrons gyrate in opposite clockwise direction in a way that the magnetic field created by the gyrating particles should always be opposite to that externally imposed (Chen, 2010).

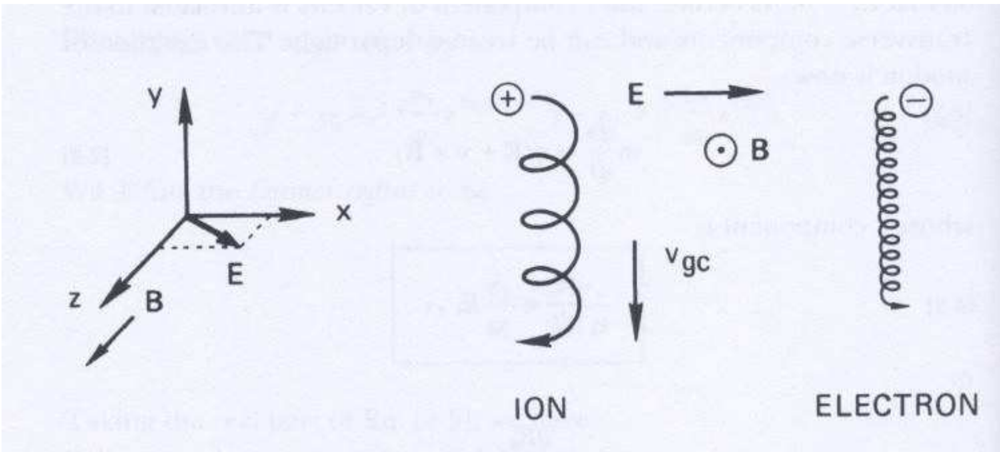

Figure 2.7: $\vec{E} \times \vec{B}$ drift, where particles of opposite charges are drifted in the same direction but with opposite clockwise orientation (Chen, 2010).

known as the electric drift or ($\mathbf{E}\times\mathbf{B}$) drift is established, such that:

$$\mathbf{v_e} = \frac{\mathbf{E} \times \mathbf{B}}{B^2}, \tag{2.9}$$

which is independent of q, so electrons and protons drifts in the same direction (Figure 2.7).

2.2.2 Inhomogeneous B and E Fields

Introducing inhomogeneity into the system makes it impossible to get exact solutions, thus approximation is needed. This approximation is known as the Guiding

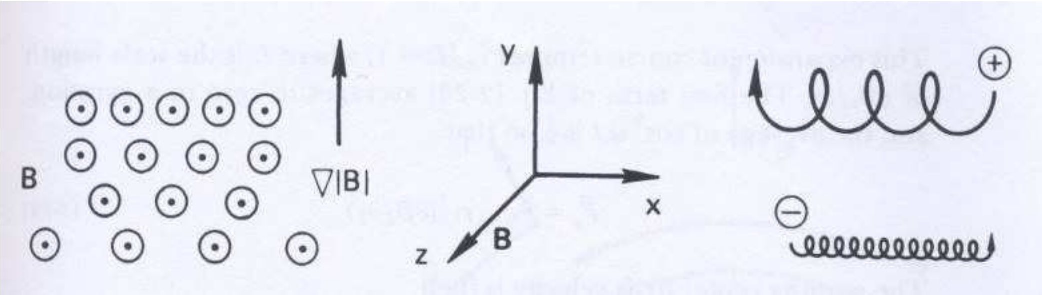

Figure 2.8: A z-directed magnetic field varying in the y-direction causing a grad-drift where particles of opposite charges drift in opposite directions (Chen, 2010).

Centre Theory. "Guiding Centre theory provides the reduced dynamical equations for the motion of charged particles in slowly varying electromagnetic fields, when the fields have weak variations over a gyration radius (or gyro-radius) in space and a gyration period (or gyro-period) in time" (Cary & Brizard, 2009), thus it is valid when $r_l \ll L_0$ (length scale) or gyration period $p \ll t_0$ (time scale of variations).

∇ B $\perp$ B, Grad Drift

Expanding **B** along the direction where it is varying and averaging over gyrations yields:

$$\mathbf{v_{grad}} = \pm\frac{1}{2}v_\perp r_l \frac{\mathbf{B}\times\nabla B}{B^2}, \tag{2.10}$$

where electrons and protons drift in opposite directions (Figure 2.8).

Curved B, Curvature Drift

Curved field lines of curvature radius $R_c \gg r_l$ cause centrifugal force such that:

$$\mathbf{v_R} = \frac{mv_\parallel^2}{qB^2}\frac{\mathbf{R_c}\times\mathbf{B}}{R_c^2}. \tag{2.11}$$

∇ B $\parallel$ B, Magnetic Mirroring

Figure 2.9 show fields converging toward stronger regions, which generate a force when acting on particles, causing them to bounce backward. This force is given as:

$$\mathbf{F_z} = -\mu\nabla_\parallel\mathbf{B}, \tag{2.12}$$

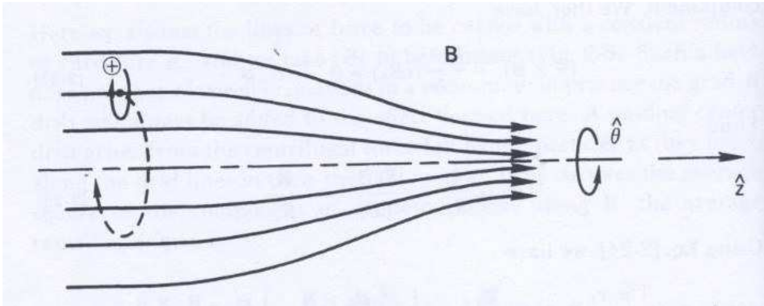

Figure 2.9: Converging magnetic field lines where particles move from weak to strong field regions thus experiencing a mirroring effect that they can escape from or be trapped in depending on their pitch angle (Chen, 2010).

where μ is the magnetic moment given by:

$$\mu = \frac{1}{2}\frac{mv_\perp^2}{B} \tag{2.13}$$

Derivation on μ shows that it is adiabatic invariant. Adiabatic invariance is the constant of the motion (action integral taken over one period) which does not change even if the motion becomes not quite periodic when the system slightly changes. μ is one of three adiabatic invariants in plasma physics. This invariance in μ allows particles to be reflected when moving from weak to strong field.

Other Drifts

A non-uniform **E** field causes a drift such that:

$$\mathbf{v_E} = (1 + \frac{1}{4}r_l^2\nabla^2)\frac{\mathbf{E}\times\mathbf{B}}{B^2} \tag{2.14}$$

and a time varying **E** field causes polarisation drift given by:

$$\mathbf{v_p} = \pm\frac{1}{w_c B}\frac{d\mathbf{E}}{dt} \tag{2.15}$$

2.3 Particle Acceleration and Test Particle Model

2.3.1 Basic Concepts

A substantial fraction, 10-30 %, of flare released energy is transformed to kinetic energy in non-thermal electrons and ions ((Aschwanden, 2002); (Klein & MacKinnon, 2007)). A characteristic length scale for the kinetic process is the ion Larmor radius which is of the order one meter in the corona. Thus it is very difficult to study particle acceleration and motion during flare evolution as the global structure has much larger typical size. The transformation from magnetic to kinetic energy can be divided into 2 phases, primary and secondary. The primary phase occurs during the impulsive phase of the flare where electrons, for instance, with coronal thermal energies (about 0.1 keV) gain energy of more than 2 orders of magnitude in less than 1 second known as *bulk energisation*. This is observed in hard X-ray (Kiplinger et al., 1984). The secondary phase could be interpreted as a result of the primary, accelerating particles by shock waves associated with flares or CMEs. It is less efficient than the first, in the context of particle acceleration in solar flares, but important in the context of SEPs (solar energetic particles) accelerated into interplanetary space. Our main interest is in the primary phase and shocks are beyond the scope of this thesis; however, a point worth mentioning here related to flares are the shocks produced by magnetic reconnection. Aurass et al. (2002) and Mann et al. (2006) detected radio signatures of such shocks, reporting that they are extremely rare. These shocks, which may be slow or fast at inflow or outflow regions, could accelerate ions, for example, to high energies (100 MeV) in less than 1 sec (Ellison & Ramaty (1985); Tsuneta & Naito (1998)).

Several processes may be involved in the conversion of magnetic energy into kinetic energy of non-thermal particles in flares with variable priority depending in the event itself. The most accepted processes are ((Melrose, 1990); (Benz, 2002)):

1. Stochastic acceleration.

2. Electric field parallel to magnetic field.

3. Fermi acceleration by shocks.

In our thesis we concentrate on the second, despite the first being preferred when dealing with resonant acceleration by magnetic field of low frequency waves ((Miller et al., 1997); (Schlickeiser & Miller, 1998); (Petrosian et al., 2006)). The convective electric field associated with reconnection, which plays an essential role in particle acceleration, can be estimated in Gaussian units as follows (Shibata & Magara, 2011):

$$E \sim \frac{v_i}{c} B_i \sim \frac{v_{jet}}{c} B_{jet}$$

$$E \sim 3 \times 10^3 \Big(\frac{M_A}{0.1}\Big)\Big(\frac{B}{100G}\Big)^2 \Big(\frac{n_{jet}}{10^{10} cm^{-3}}\Big)^{-1/2} V m^{-1} \tag{2.16}$$

This formula explains why acceleration by electric field is efficient in the impulsive phase and less important in the decay phase as v_{jet}, which is the plasma inflow speed, decreases significantly in the final phase of a flare. In addition for the above estimation, we could define a critical parameter in the solar corona (in the context of electric field responsible for particle acceleration) termed as the Dreicer electric field which is related to Coulomb collisions. Above the Dreicer value, where Coulomb collisions become unimportant, particles are freely accelerated. The equation for the Dreicer electric field is:

$$E_d = \frac{e ln\Lambda}{4\pi\epsilon_0\lambda_D^2} \propto \frac{n}{T} \tag{2.17}$$

where $\ln \Lambda \approx 20$ is the coulomb logarithm and λ_D is the Debye length having the formula:

$$\lambda_D = \sqrt{\frac{\epsilon_0 k_b T}{ne^2}} \tag{2.18}$$

Observations and studies of particle acceleration show that electric fields present in flares are super Dreicer by many orders of magnitude. Working out typical coronal value of E_d where, $n = 10^{14}\mathrm{m}^{-3}$, and $T = 1.5 \times 10^6$ K, yields that $E_d \sim 4 \times 10^{-4}$ Vm^{-1}.

Particles which are driven to the current sheet by the $\mathbf{E} \times \mathbf{B}$ drift become closer to the X-point (or more precisely when talking in 3D to the X-line) where the magnetic field vanishes and so particles are no longer magnetised and can be directly accelerated by the electric field. Of course, any particle that manages to become close to the X-line acquires more energy. Besides particles that remain in the current sheet for longer times before being ejected out also acquire more energy; that is why protons acquire more energy than electrons as the latter are ejected more quickly from the current sheet (Speiser, 1965). For a particle to be accelerated to a specific E_{kin}, this should happen in a time less than the collision time for energy loss, $\tau_{coll}(E_{kin})$, given in the following formula for an electron with velocity v_T^3 and electron density n_e (Benz, 2008):

$$\tau_{coll}(E_{kin}) = 0.31\Big(\frac{v_T}{10^{10}cms^{-1}}\Big)^3\Big(\frac{10^{11}cm^{-3}}{n_e}\Big)s \tag{2.19}$$

Substituting typical coronal values yields that electrons are accelerated within less than 1 sec and high densities make particle acceleration inefficient. Electron acceleration is more likely to occur in every major coronal eruptive event than ion acceleration due to the difference in inertia between electrons and ions, which allows electrons to move more freely. These high energy electrons could contribute to the formation of HXR sources at the foot-points and loop-top above SXR source and some could manage to escape to the outer space driving plasma oscillations observed in type III radio bursts. One thing to add here is that when a strong electron beam is formed due to large amounts of electrons being accelerated, a reverse or a return current is formed which could contribute to atmosphere heating (Karlicky, 2008); however as Holman (1985) and Litvinenko (1996) reported, observed accelerated electrons are difficult to match with the classic current sheet model as the number of electrons is limited by the current.

In order to understand the flare progress and particle behaviour near the reconnection region in the corona, a lot of analytical studies and numerical simulations dealing with very complex configurations as that existing in the corona have been done. Until now, no self-consistent model could explain all the phenomenological features of particle acceleration in solar flares, as it is widely accepted that multi-mechanisms contribute for such phenomena. Two main numerical simulations could be used in our subject, the test particle, and Particle-In-Cell (PIC) simulations. Both methods have their advantages, disadvantages, and limitations. PIC simulations are beyond the scope of this thesis, but one of its advantages is the self-consistent treatment of particles and fields, whilst one of its disadvantages is the severe limitation concerning the particle mass and simulation region dimensions (some PIC work can be found in Birdsall (1991), Drake et al. (2005), Tsiklauri & Haruki (2007), and Siversky & Zharkova (2009)). On the other hand, the test particle method, (used method in this work and probably the major numerical approach used), has proved its applicability especially when considering large acceleration length and time scales. The test particle method means choosing electric and magnetic fields from a model (either a MHD simulation or analytical model) and calculating particle trajectories in these fields. The electric and magnetic fields generated by the test particle are ignored. The concept of a test particle often simplifies problems and can provide a good approximation for physical phenomena. In addition to its uses in the simplification of the dynamics of a system within particular limits, it is also used as a diagnostic in computer simulations of physical processes. In our context, plasma physics or electrodynamics, the most important characteristics of a test particle is its electric charge and its mass. When adding external electric and magnetic fields, the behaviour of a test particle is determined by effects of the Lorentz force. This method itself is divided into two approaches, the Full Trajectory, and Guiding Centre Approximation (GCA). The first calculates full particle motion by solving Lorentz equations of motion, whereas the second has its own theory as discussed in § 2.2 (the relativistic set of GCA equations being solved is presented in Appendix A.2). In our thesis we perform both approaches and compare results. MHD and test particle simulations are related as the second need to import the results of the first to perform. MHD simulations give us the values of the magnetic and electric fields and their derivatives and can image the progress of the reconnection region before and after reconnection. Test particle simulations use these calculated values of magnetic and electric fields and import them as snapshots to give information about particle trajectories and their corresponding energy spectra.

2.3.2 Analytical Models of Particle Acceleration

Although analytical solutions are limited to simple configurations of magnetic and electric fields and the numerical simulation approach is more efficient for complex cases, it is worth considering some of them to build up some basics. Speiser (1965) was among the first to develop an analytical model for a current sheet and solve particle trajectories within it. Sonnerup (1971) and Cowley (1978) also did similar work. Speiser was motivated by the discovery of a magnetically neutral sheets in the Earth's geomagnetic tail reported by Ness (1965). The author formulates two types of neutral sheets, those with and without a perpendicular magnetic field to the sheet plane. The fields are as follows

$$\vec{B} = b\big(\eta \hat{e_x} - \frac{x}{d}\hat{e_y}\big) \tag{2.20}$$

$$\vec{E} = -a\hat{e_z} \tag{2.21}$$

When $\eta = 0$, the model reduces to the simple case where no perpendicular magnetic field exists. For this simple model, particles are trapped inside the sheet and undergo damped oscillations about the sheet where their energy grows without bound. When adding a small component of perpendicular magnetic field, particles turn away from the accelerating electric field toward the same direction and are ejected off the sheet when they turn 90^o. The Author noticed that both protons and electrons are ejected with the same velocity but with electrons being ejected sooner as they are turned much faster (see Figure 2.10). Litvinenko & Somov (1993) pointed out that the case studied by Speiser (1965) has only a small probability of occurrence as the latter consider trajectories near a neutral plane where $B = 0$. In reality, a magnetic field should be always present with its transverse (perpendicular to the current sheet plane) and longitudinal (parallel to the electric current inside the sheet) components (Gorbachev et al., 1988). Such a current sheet is called non-neutral current sheet. Litvinenko & Somov (1993) showed that a transverse

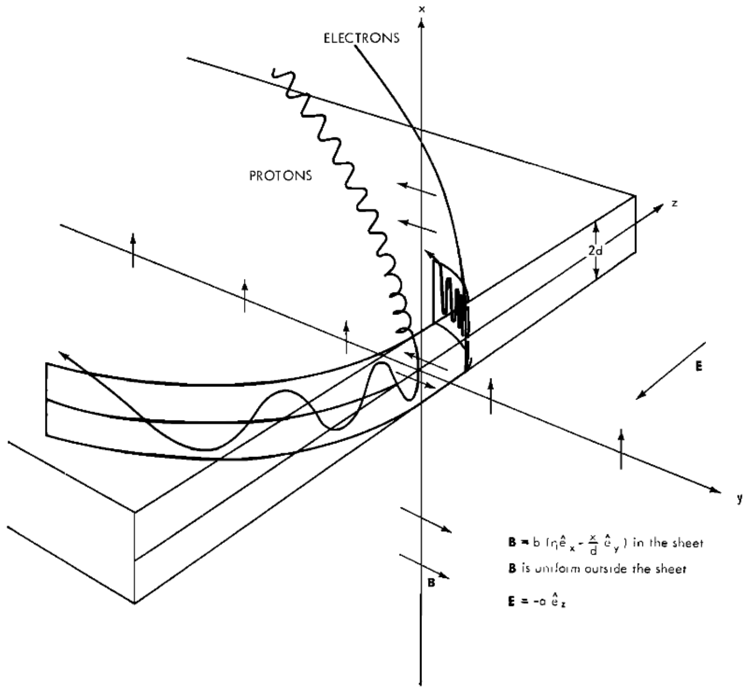

Figure 2.10: Particle trajectories when adding a small perpendicular component of magnetic field to the simple model. Oscillating protons and electrons are accelerated in opposite directions but turns away from the electric field toward the same direction due to the presence of the extra magnetic field. Figure not to scale (Speiser, 1965).

magnetic field turns the particle trajectory causing it to leave the current sheet, whilst in contrast, the longitudinal component tries to keep or to return the particle back to the sheet. Speiser (1965) consider the case of transverse magnetic field and showed that particles are ejected in a very small time thus not allowing them to have sufficient energy to explain the first stage of acceleration in flares, hence the longitudinal component should not be ignored. This longitudinal component has a effective role in accelerating particles and energy gain that could explain the first stage of electron acceleration in solar flares and the production of X-rays. Besides, it cannot be ignored after being observed in the geomagnetic tail (Fairfield, 1979) and X-ray observations of solar flares showing a strong longitudinal magnetic field at separators (Mandrini & Machado, 1992).

In a complementary paper to Litvinenko & Somov (1993), Litvinenko (1996) gave a nice explanation for the role of electric and magnetic fields (consider fields as shown in Figure 2.11). The paper, stated that the particle motion along the electric field causes efficient acceleration and the presence of a magnetic field can

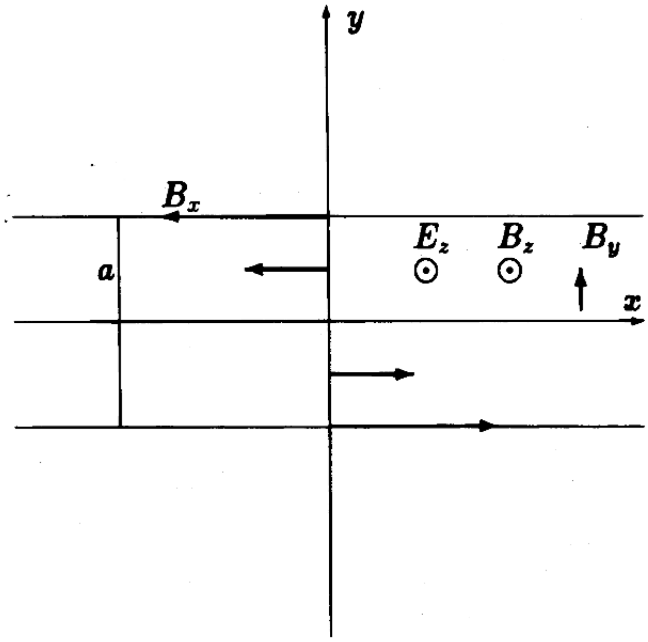

Figure 2.11: Different components of electric and magnetic fields inside a current sheet (Litvinenko, 1996).

change the particle trajectory allowing the displacement along $\vec{E}$ and the energy gain to be finite although it does not affect the particle kinetic energy. The parallel $\vec{B}$ component ($\vec{B}_x$ and $\vec{B}_y$ in Figure 2.11) magnetises charged particles forcing them to follow magnetic field lines and keep them inside the current sheet, to gain more energy from the electric field, whereas the perpendicular component also known by the guiding field ($\vec{B}_z$ in Figure 2.11) tries to eject them, reducing the gained energy. This guiding field when present has a great influence in the whole processes as it can disturb particle orbits and change their bounce frequency and can, when reaching some limiting values, cause trajectory asymmetry between electrons and ions (Zhu & Parks, 1993). Considering a nonzero guiding field as in Figure 2.12, particles accelerated at the reconnecting current sheet will lose the symmetry of their orbits in the phase space about the $z = 0$ plane, hence also change their bounce frequency. Importantly, its presence allows us to use the guiding centre approximation to calculate particles orbits (Wood & Neukirch, 2005). Zharkova & Gordovskyy (2004) showed that when $B_y/B_z > 10^{-2}$, then symmetry is completely destroyed and opposite charged particles are ejected into different legs or foot-points of the reconnecting loops. Assuming asymmetry between electron and proton beams occurs and knowing that electrons take about 1 sec and protons about 10 sec to cross the 10^7 m loops leg, then a temporal delay in the occurrence of HXR caused by this asymmetry would takes place. Trajectories are completely symmetric when $B_y/B_z < 10^{-6}$ as proposed by Zharkova & Gordovskyy (2004) and a neutralised beam is ejected. Between the 2 limits, a partially symmetric event occurs (see Figure 2.13).

It is worth noting that all authors who have studied particle acceleration in reconnecting current sheets from an analytical point of view derive extensively a lot of critical expressions. These include when a particle could leave the sheet and in what time, taking into account the existence or absence of transverse and longitudinal magnetic fields and the particle behaving adiabatically or not with other features. We do not present them here, as all expressions depend on the model considered. In addition to following the field lines, particle solved analytically show clearly the ordinary $E \times B$ drift known to be the dominant one among all other drifts (Schmidt, 1979). One interesting point discussed by Litvinenko (1996) is the theoretical value of the electric field in the reconnecting region, E_0. He stated that $E_0 = 10\ V\ cm^{-1}$. Forbes (1992) through numerical simulations showed that magnetic reconnection in erupted filaments in corona proceed at this value, and Foukal & Behr (1995) measured a field of $\sim 35\ V\ cm^{-1}$ in the flare surge.

2.3.3 Test Particle Model

Kliem (1994) using the full trajectory approach with a fragmentary electric field model showed that particles are accelerated during very small time $\sim 10^{-2}$ sec to relativistic energies. As we mentioned previously, Zharkova & Gordovskyy (2004) considered particle orbits in simple non-neutral current sheet and showed that the symmetry is completely destroyed when using strong longitudinal magnetic field and opposite charged particles are ejected into different legs or foot-points of the reconnecting loops. Gordovskyy et al. (2010a) get similar results as Zharkova & Gordovskyy (2004) and show that electrons and protons are accelerated to tens of

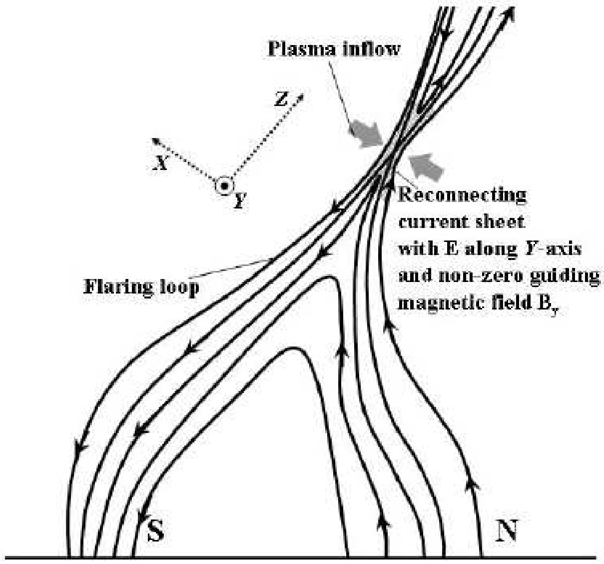

Figure 2.12: Field configuration model presenting a non-zero guiding field and electric field in the y-direction and the current sheet laying in the $x-z$ plane (Zharkova & Gordovskyy, 2004).

MeV in the forced reconnection model mainly near the X-point and less effectively around the magnetic islands. This was also seen by Oka et al. (2010) of 2 interacting islands. Dalla & Browning (2006) reveal the existence of two population of accelerated particles around 3D null points, one manages to escape near the spine (the reconnection site in 3 dimensions), and others are trapped near the null-point. Gordovskyy et al. (2010b) also denote two distinct populations of accelerated particles in fragmenting periodic current sheets. Particles accelerated in open magnetic fields have an energy spectrum which is a combination of a Maxwellian distribution and power law, and particles accelerated in closed magnetic field lines around O-points follow the guide field with a narrow energy range. Hannah & Fletcher (2006) also using the full trajectory approach with constant electric field and hyperbolic X-point showed that particles are accelerated during few gyro-periods in constant electric field. The authors pointed out that the number of accelerated particles increase when the guiding field exists. Similarly, Petkaki & MacKinnon (2007) using oscillating electric fields indicated that energy spectra are bi-modal with protons and electrons being accelerated to $\sim$10 MeV and $\sim$ 1 MeV respectively.

The values of some basic parameters of the field configuration influences a lot

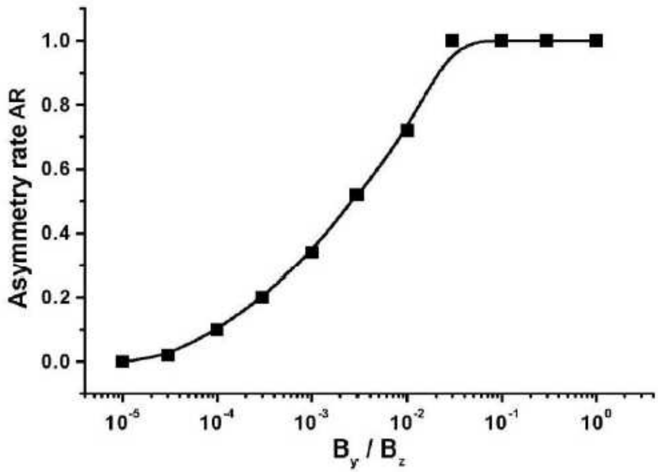

Figure 2.13: Asymmetry rate vs. the B_y/B_z ratio from work done by Zharkova & Gordovskyy (2004). The asymmetry rate is zero for values of $B_y/B_z < 10^{-6}$ where particles are ejected as a neutralised beam but this symmetry is completely destroyed when B_y/B_z exceeds 10^{-2} where particles travel all the way through different loop legs.

on the final shape of the energy spectra. The stronger the maximum electric field is the smoother the curve becomes and the greater the energy gain of the particles (Wood & Neukirch, 2005). Figure 2.14 shows 3 different curves when varying the maximum electric field, E_0, by 2 orders of magnitude from 10 to 1000 Vm^{-1}, where the spectral index γ is steeper for lower E_0. Hannah & Fletcher (2006) discussed the influence of the angle between separatrices ($\arctan\alpha$), where ($0 < \alpha \leq 1$), when using a simple flare model such as, $\vec{B} = B_0(\alpha^2 y, x, const.)$ and $\vec{E} = E_0\vec{z}$. Figure 2.15 shows the energy spectra results when varying α. "Three things are immediately clear: as α decreases, the heated component of the distribution moves to a slightly higher energy, more particles are accelerated out of the thermal distribution into the bump in the tail, and this bump occurs at lower energies" Hannah & Fletcher (2006). Obviously when the resistivity increases in the system more magnetic energy will be transferred to the particles. Figure 2.16 shows the final energy for 50 particles versus their initial positions when varying the resistivity by 2 orders of magnitude. We can see that particles at the same position gain more energy in case of higher resistivity (Heerikhuisen et al., 2002). Finally, concerning the spectral indices γ, we can note that its value is smaller in the case of protons than electrons, so protons have harder spectra than electrons. Typical values show indices of $\gamma \sim 2$ in case of

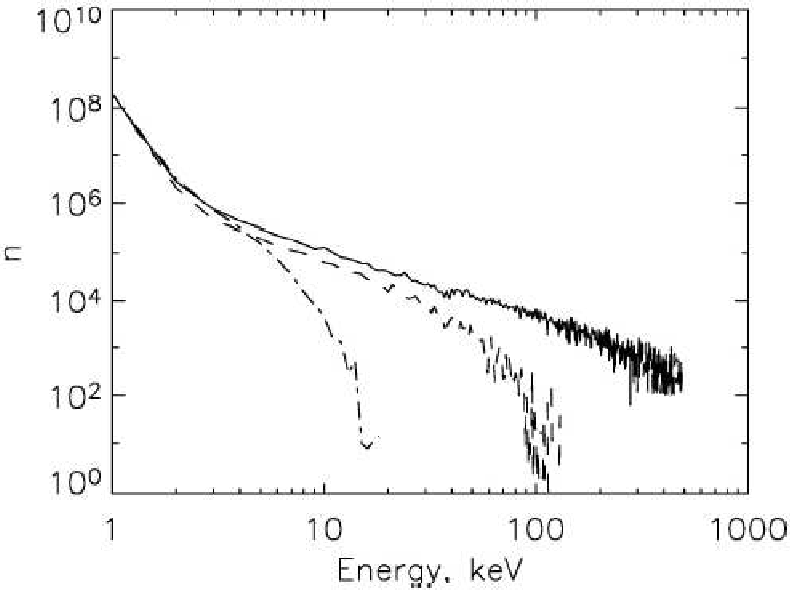

Figure 2.14: 3 energy spectra curves for a system varying its maximum electric field E_0 from 1000 Vm^{-1} (top curve) to 10 Vm^{-1} (bottom curve). The energy spectra curve become more steeper and its spectral indices grow up whenever the maximum electric field is decreased (Wood & Neukirch, 2005).

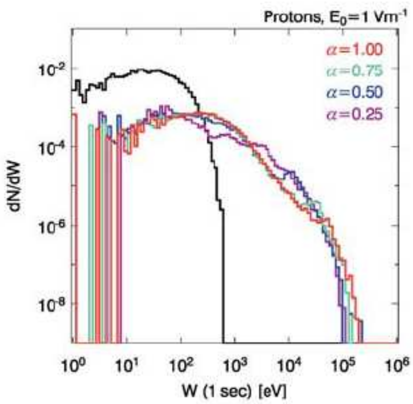

(a)

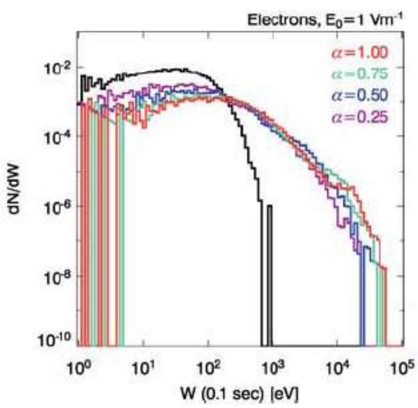

(b)

Figure 2.15: Energy spectra for a) protons and b) electrons with 4 different values of the angle between separatrices (α) (Hannah & Fletcher, 2006).

electrons between 10 KeV and 1MeV, while $\gamma \sim 1.0$-1.5 in case of protons with energy of $\sim$1MeV (Gordovskyy et al., 2010b). In addition, γ differs within reconnection stages (X or O-stages). Energy spectra seems to be harder in the X-point stage, that is X-point has lower γ value. At $E = 100$KeV, γ is between 1.0 and 1.5 in the X-stage while its between 1.5-3 at the same energy in the case of O-point reconnection stage (Gordovskyy et al., 2010a).

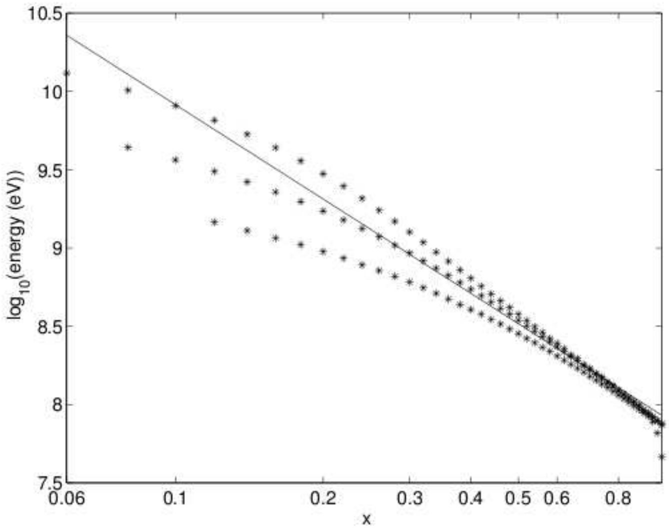

Figure 2.16: Final energy vs. initial position for 50 particles experiencing different resistivity from top to bottom, $\eta = 10^{-6}, \eta = 10^{-7}$, and $\eta = 10^{-8}$ respectively. We can deduce that when resistivity increases, more energy will be transformed to the particles as the tearing mode will be more efficient pushing field lines to reconnect (Heerikhuisen et al., 2002).

Particle Trajectories and Energy Spectra

All mentioned references in the previous section and a lot other authors simulate particle trajectories and energy spectra in the context of their acceleration in solar flares using the test particle approach. We cannot present them all here, but instead we will concentrate on Gordovskyy et al. recent work as it is used later within our own work for comparison as both use the same MHD data for forced reconnection events. Figure 2.17 shows single proton and electron trajectories for certain experiments in the forced reconnection model created using the GCA approach in Gordovskyy et al. (2010a) paper. It can be seen that both protons and electrons follow to a high extent the magnetic field lines. The $\mathbf{E} \times \mathbf{B}$ drift effects particle paths at some stages, where they cross the magnetic field lines, but it remains a secondary effect in the view of particles following field lines (Gordovskyy et al., 2010a). Gordovskyy et al. (2010b), after distinguishing between 2 magnetic regions, open (near the boundaries of the current sheet) and closed (at magnetic islands near the diffusion region), noted that particles experience different trajectories within these regions. They travel long distances with some oscillation in the first while being trapped with rotation motion in the sheet plane in the second and in both cases following the magnetic field lines. One further point to add is that when particles encounter a slow shock layer associated with reconnection, (mainly after being accelerated at the neutral line), they suffer large orbit modification leading to them no longer following field lines but rather a complicated motion. This is particularly important for protons. This sudden change is accompanied by a small gain of energy of several eV for electron and 10 KeV for protons (Sato et al., 1982). Figures 2.18 show the energy spectra for protons and electrons for a certain exper-

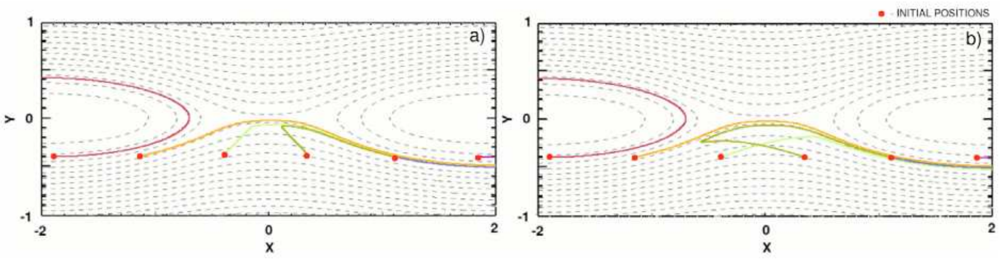

(a)

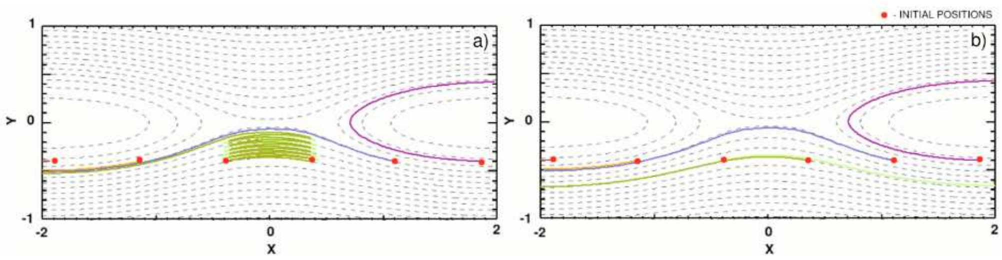

(b)

Figure 2.17: Particle trajectories for a) protons starting with initial thermal velocities $v_{int} = 0.1V_A$ where left panel correspond to large magnetic moment and right panel for small one and b) electrons with initial thermal velocities $v_{int} = 3.9V_A$ and same panel description as for protons (Gordovskyy et al., 2010a).

iment done by Gordovskyy et al. (2010b). Both species have a similar evolution of their energy spectra. Most of the electrons and protons are in the thermal region as their initial state with a Maxwellian distribution and a small fraction have higher energies making a tail that evolves as a broken power law (N $\sim$ E$^{-\gamma}$). This is true as just small number of particles can enter the diffusion region and be accelerated to higher energies. The authors show that particles acquire in the X-stage more energy than the O-stage and a higher percentage of simulated particles are accelerated. In addition, particles within closed regions gain more energy than that in the open one.

Unfortunately, in our thesis we study single particle motion rather than simulating a large number to deduce the energy spectra due to time matter. Extending this work to simulate a large number of particles could be a project for the future.

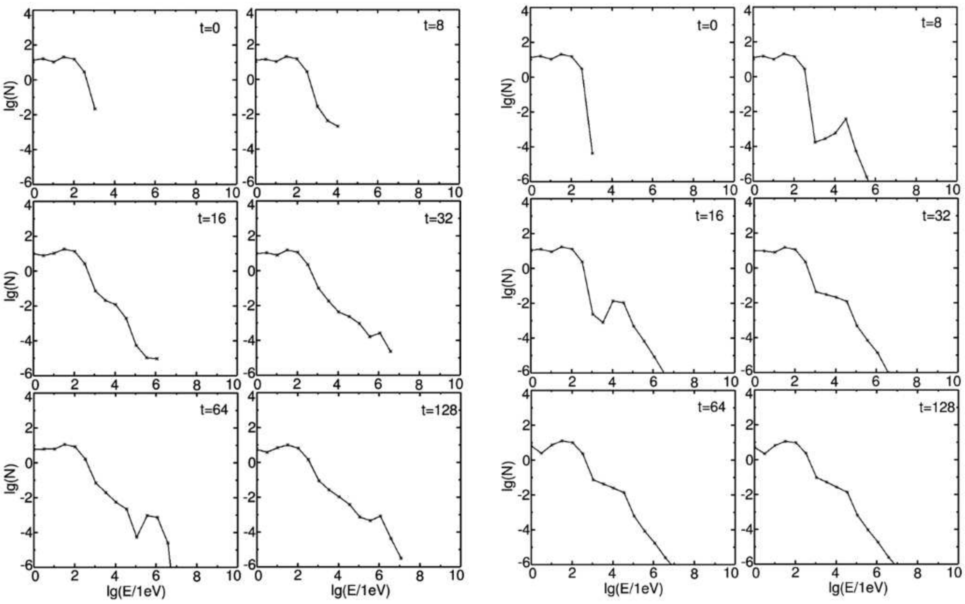

(a) (b)

Figure 2.18: Energy spectra for a) protons and b) electrons for the magnetic reconnection simulated in figure 2.20 (Gordovskyy et al., 2010b) for the whole process. It can be seen that most particles remain with their initial thermal velocities and just few of them are accelerated to high energies.

2.3.4 Forced Reconnection Using MHD Simulations

In order to perform the test particle approach, it first needs to be defined in a convenient model consistent with the solar corona. We have shown in detail previously that reconnection is the preferred process for such a model, thus we need to establish this model by simulating it to know how the magnetic field, electric current, plasma velocity, and their associated parameters evolve during reconnection. Several MHD codes exist for reconnection. The code we use, is widely used in our field, is the $LareXD$ code (Arber et al., 2001) with "X" standing for the number of dimensions (2 or 3). In our case we are dealing with 2D, so we use the $Lare2D$ code. In general $LareXD$ are Lagrangian remap codes for solving the nonlinear MHD equations in 2 or 3 dimensions with user controlled viscosity and resistivity (the standard set of resistive MHD equations being solved by the code are given in Appendix A.3). The code uses a staggered grid and is second order accurate in space and time. The staggered grid is used to build conservation laws into the finite difference scheme and time step splitting into Lagrangian step followed by remapping onto the original grid make it easy to add any additional physics. LareXD is compatible with IDL and $VisIt$ visualisation packages.

The current sheet is produced by external deformation of smooth magnetic fields. The preferred initial magnetic configuration is a stationary force-free Harris sheet (Harris current sheet is a stationary solution to the Maxwell-Vlasov system (Schindler, 2010)), which is magnetically dominant (low-β plasma). For simplicity, thermal conduction, radiation, and viscosity effects are ignored. This sheet is more relevant to the solar corona than a neutral Harris sheet as the latter is MHD stable whereas sheared force-free field might be tearing unstable, thus releasing more magnetic energy (Vekstein & Jain, 1998). The initial magnetic field configuration for the force-free Harris sheet is:

$$\vec{B}_{ini} = \Big[\ tanh\frac{y}{L_0}\ ;\ 0\ ;\ sech\frac{y}{L_0}\ \Big] \tag{2.22}$$

hence, as $\mathbf{j} \times \mathbf{B}$=0 (force-free) the current density is:

$$\vec{J}_{ini} = \Big[\ -\frac{1}{L_0}tanh\frac{y}{L_0}sech\frac{y}{L_0}\ ;\ 0\ ;\ -\frac{1}{L_0}sech^2\frac{y}{L_0}\ \Big] \tag{2.23}$$

where L_0 is the characteristic length scale and current sheet half-width. Figure 2.19 shows magnetic field and current density initially. The local current-dependent resistivity is defined as a step-like function such as:

$$\eta = 0, \quad (j < j_{cr})$$

$$\eta = \eta_1, \quad (j \geq j_{cr}) \tag{2.24}$$

Initially the resistivity is zero and the system is steady by setting the critical current

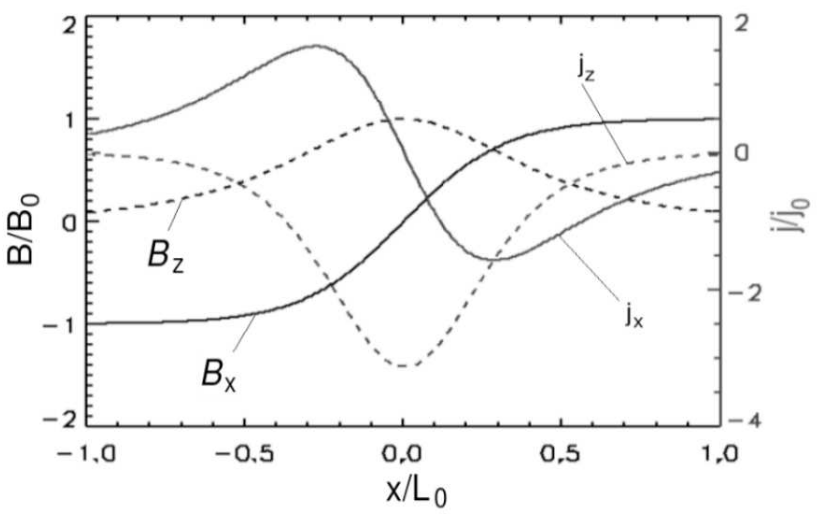

Figure 2.19: Initial magnetic field and current density as defined in equations 2.22 and 2.23 respectively (Gordovskyy et al., 2010a).

density greater than the maximum initial current density ($j_{cr} = 1.02 j_{max}(t = 0)$). At $t = 0$, the stable system experiences a transient spatially varying displacement at one of its boundary edges mainly by letting the plasma flow perpendicular to this boundary for a specific perturbation time t_p. From Gordovskyy et al. (2010b) and Gordovskyy et al. (2010a), the plasma flows in the y-direction such that:

$$V_x(y = \pm y_1) = 0$$

$$V_y(y = -y_1) = \frac{\Delta}{t_p} cos\Big(\frac{2\pi}{L_x}X\Big)\Big[1 - cos\Big(\frac{2\pi}{t_p}t\Big)\Big]$$

$$V_y(y = +y_1) = -\frac{\Delta}{t_p} cos\Big(\frac{2\pi}{L_x}X\Big)\Big[1 - cos\Big(\frac{2\pi}{t_p}t\Big)\Big]$$

$$V_z(y = \pm y_1) = 0 \qquad (2.25)$$

where $\pm y_1$ are top and bottom boundaries in y-direction, Δ is the displacement amplitude, and $L_x = l_x/L_0$ is the period of boundary deformation in the x-direction. As a result, magnetic field lines begin to deform and at the end of the impulse, ($t = t_p$), these lines are deformed near the top and bottom boundaries by $\delta Y = \Delta cos\Big(\frac{2\pi}{L_x}X\Big)$ and $\delta Y = -\Delta cos\Big(\frac{2\pi}{L_x}X\Big)$. Boundary conditions for such a system should be chosen carefully to insure no extra forces or electric currents oriented perpendicular to the perturbed boundary exist and to insure the rigidity of the boundary when perturbation ends ((Hahm & Kulsrud, 1985); (Vekstein & Jain, 1998); (Jain et al., 2005a)).

Simulating reconnection reveals a lot of details. Figure 2.20 shows how magnetic fields, current density, and plasma flow evolve with time in a forced reconnection event. First within the perturbation time, when magnetic fields are deformed, current density is observed to accumulate at the centre, allowing the threshold value for the switching resistivity to be reached. Thus resistivity becomes active and reconnection proceeds at the central region, as a result magnetic islands begin to form. At the first stages, as shown in Figure 2.20, plasma inflows in the y-direction and outflows in the x-direction and as time proceeds, the thickness of the sheet in the y-direction decreases and the plasma begin to outflow in 4 separatrix jets (Gordovskyy et al., 2010a). An expected and observed feature during this time is the decrease in magnetic energy and increase in thermal internal energy. Gordovskyy et al. (2010a) in agreement with analytical estimation for dissipation rate of magnetic energy in forced reconnection by Hahm & Kulsrud (1985) and Vekstein & Jain (1998), pointed out that $dE_m/dt = \eta_1^{-0.6}$ where E_m being the magnetic energy and η the magnetic diffusivity. When the process approaches the end, magnetic islands grow around O-points to relatively large sizes where magnetic field and electric current are concentrated. When the field reaches a new equilibrium, the reconnection rate diminishes and all parameters do not change.

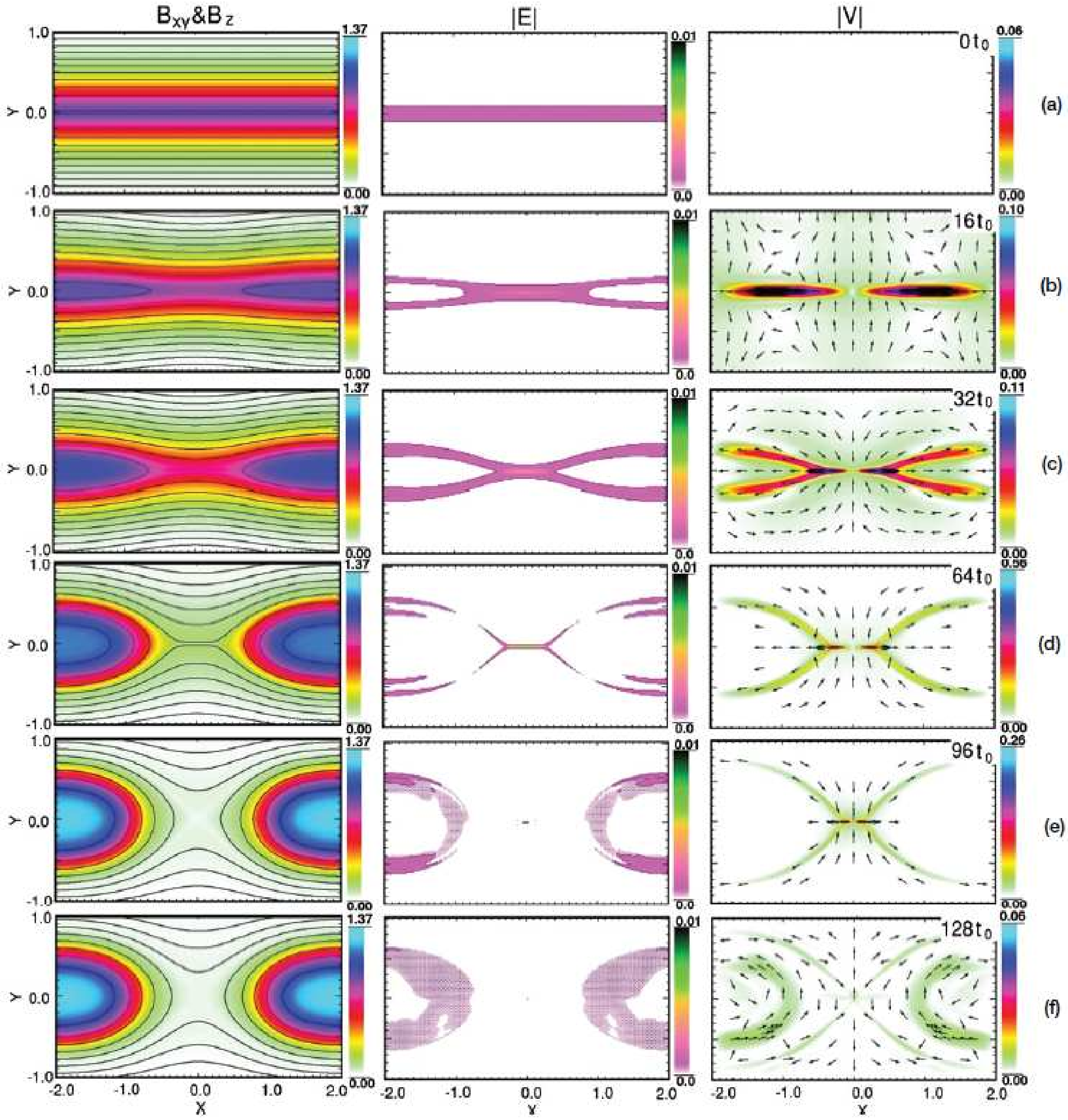

Figure 2.20: Evolution of magnetic field, current density, and plasma velocity in a current sheet due to forced reconnection (Gordovskyy et al., 2010b). Left panels show $x - y$ magnetic field lines in the current sheet with z-component plotted as a colour-scale. Middle panels correspond to the absolute value of the electric field. The right panels show how plasma flows in and out the current sheet marked by the black arrows, and a colour-scale for the absolute plasma velocity. The snapshots were taken at t=[0(a),16(b),32(c),64(d),96(e),128(f)]t_A.

Chapter 3

Methodology

Our aim in this project is to test particle trajectories and their acceleration mechanism by the direct DC acceleration process. Dealing with plasma is really a hard job due to its schizophrenic personality. Plasma sometimes behaves like fluid where the motion of individual particles could be dismissed. In this regime, the density is high and collisions dominate and simple equations of fluid dynamics operate. On the other hand, when densities are very low, plasma behave as a collection of individual particles each having its own trajectory. Plasma densities vary dramatically from one region to another. In the case of the Sun, it is well known that the corona is a low density region and things become more dense when we go down to the Sun's surface. As our interest is to investigate how particles are accelerated due to solar flares in the corona where densities are low, then single particle trajectories need to be considered. Two numerical approaches will be considered to solve particles trajectories: the full trajectory approach by solving the Lorentz equation of motion without any approximations, and the Guiding Centre Approximation (GCA) theory as discussed previously. We will compare both methods when working with field data on finite grid. What we expect is to see similar motions using the 2 codes when the conditions of GCA are fulfilled, together with all other parameters like velocities, drift, energy and so on. We already have a well organised and tested GCA code written by one member of our Solar physics group, Dr. Mykola Gordovskyy, thus our first task would be to write a well organised program that solves the Lorentz equation of motion with other functions that give us data on drifting, energy conservation, and some others.

3.1 The Full Trajectory Particle Code

Writing numerical codes especially for those solving differential equations, with other packages for different functions, may be tricky as any addition to a single loop can cause a lot of time and data-space consumption. In order to test the code we use some analytical solutions for the case of uniform and static electric and magnetic configurations as we shall discuss in the next section. We use two numerical methods, the first is Runge-Kutta of 4th order (RK4) and the second is Adams-Bashforth also of 4th order (A-B4), where the user can select the method; this will let us compare between the two methods. Besides, relativistic and non-relativistic calculations is an optional feature of this code, where the user should specify this in the input file. The code is written in C++ and divided into 4 modules for the 4 different combination of methods (RK4 or A-B4) and calculations (relativistic or non-relativistic).

The code can output many parameters, but for purpose of testing we will concentrate on the coincidence of particle trajectories calculated analytically and numerically to make sure that the numerical scheme is working properly. Hence, output data files will contain positions (x, y, and z), velocities (v_x, v_y, and v_z), magnetic fields (B_x, B_y, and B_z), electric fields (E_x, E_y, and E_z), and differences in positions and velocities at each step between numerical and analytical calculations. In order to reduce numerical errors within the code and to allow generality, all parameters are made to be dimensionless. We introduce three characteristic parameters which are L_0 (characteristic length), ρ_0 (characteristic density), and B_0 (characteristic magnetic field) which need to be consistent with corona values when using real MHD data. Defining these characteristic quantities allow us to define the dimensionless coordinates as $x^* = xL_0^{-1}$, $y^* = yL_0^{-1}$, $z^* = zL_0^{-1}$, and dimensionless time and velocity as $t^* = tt_A^{-1}$, $v^* = vv_A^{-1}$ where t_A and v_A are Alfven time and velocity respectively. The Alfven velocity is given by, $v_A = B_0/\sqrt{\mu_0\rho_0}$, and the

Alfven time by, $t_A = L_0/v_A$. The dimensionless magnetic field will be, $B^* = BB_0^{-1}$, and electric field, $E^* = EE_0^{-1}$, where the characteristic electric field is defined as, $E_0 = B_0 v_A$. We define the parameter α to be the dimensionless mass-to-charge ratio as follows, $\alpha = \frac{m/q}{(m/q)_0}$. Arranging the expression of Larmor radius, $r_L = \frac{mv_\perp}{|q|B}$, and using $t = r_L/v_\perp$, we find that, $(m/q)_0 = B_0 t_A$, therefore:

$$\alpha = \frac{m}{qB_0 t_A} = \frac{1}{\omega_c t_A} = \frac{r_L}{L_0} \tag{3.1}$$

where ω_c is the cyclotron frequency. α could measure and control the validity of GCA by varying it as we shall discuss later. It has a wide range from very light particles (e.g. $\alpha = 10^{-9}$) to very heavy one (e.g. $\alpha = 10^{-1}$). Ions for instance have values around 10^{-4} like protons having, $\alpha_{p^+} \simeq 1.47 \times 10^{-4}$. The dimensional Lorentz equation of motion is:

$$m\frac{d\mathbf{v}}{dt} = q(\mathbf{E} + \mathbf{v} \times \mathbf{B}). \tag{3.2}$$

Now, by using dimensionless variables, the dimensionless Lorentz equation become:

$$\frac{d\mathbf{v}^*}{dt^*} = \frac{1}{\alpha}(\mathbf{E}^* + \mathbf{v}^* \times \mathbf{B}^*) \tag{3.3}$$

Concerning the time step, the code contains a function that calculates it for the next iteration, thus the code can have an adaptive time step. This feature could be shut off and the user should assign the time step a constant value. Three limits are taken into account when calculating the adaptive time step which should be less by a certain factor indicated by the user than the *gyration period*, *velocity to acceleration magnitudes ratio*, and *grid separation to velocity ratio* derived from the following simple relations, $\delta t \ll T$, $\delta v \ll v$, and $\delta r \ll \Delta$, respectively where Δ is the minimum grid separation (our numerical box is a square, so $\Delta_x = \Delta_y$). When the code calculates the above three values, it takes the minimum one and multiplies it by a precision factor assigned by the user. If the user set the time step to be non-adaptive the code takes the time step to be constant and equal to the precision factor.

In order for the code to operate, the user must specify initial position, velocity, and the pitch angle. These initial value are the same as entered to the GCA code to guarantee that both codes are operating with same initial quantities. As the full trajectory code works with Cartesian components while GCA with parallel and perpendicular basis, where the entered initial information is for GCA code, then full code need to make a switching to operate with its own basis (see section 4.2 for more information). In the testing section there is no need to make switching as there is no comparison with GCA, hence initial position and velocity can be in the Cartesian form. After calculating position and velocity, many quantities can be calculated depending on what we are searching for. At each stage of our thesis we create different functions to compare aspects between full trajectory and GCA.

3.2 Testing the Code Using Uniform and Static Field Lines

In order to test the full trajectory code, we first compare thoroughly with analytical solutions for uniform static fields. Mainly in our context, 5 things should be tested which when giving acceptable results mean that we can continue to the next steps with non-uniform fields and real MHD data. These tests are the Interpolation scheme, Runge-Kutta 4th order method, Adams-Bashforth 4th order method, relativistic and non-relativistic calculations, and finally test if every thing holds true when using electrons as first we will use protons as they save time and are mainly easy to handle.

3.2.1 Analytical Configuration

We choose a specific configuration of electric and magnetic fields and solve it analytically by hand and then program it in our code. Our chosen configuration was not that sophisticated but also not trivial to solve. We let the magnetic field be in the $y-z$ plane having 2 components (B_y and B_z) and the electric field just be in the z-direction. As we mentioned previously, the fields do not vary in space (uniform) and time (static), that is why an analytical solution could be obtained for such a case. To solve for positions and velocities we should solve the Lorentz equation of motion:

$$\frac{dv}{dt} = \frac{q}{m}(\mathbf{E} + \mathbf{v} \times \mathbf{B}) \tag{3.4}$$

A full derivation is found in Appendix A.4. The 6 expressions for the phase-space variables are then programmed in the code in a separate function to be called when in need. We should note that this configuration was solved using the non-relativistic version of Lorentz equation of motion and so it only serves when using the non-relativistic module in the code. Concerning the relativistic case, the Lorentz equation become:

$$\frac{d\mathbf{p}}{dt} = q(\mathbf{E} + \frac{\mathbf{p}}{\gamma m} \times \mathbf{B}) \tag{3.5}$$

where

$$\mathbf{p} = \gamma m \mathbf{v} \tag{3.6}$$

In this case we will not use the same configuration as used for the non-relativistic one as the solution is more complicated and very hard to obtaine. Hence we used a simpler case with no electric field and just the z-component of the magnetic field. The general solution for the motion of a particle in a uniform and static magnetic field using the relativistic version of equation is found in Jackson (1998), which when solved for our case yields:

$$x = \frac{v_\perp}{\omega} sin(\omega t) + x_0 \tag{3.7}$$

$$y = \frac{v_\perp}{\omega} cos(\omega t) + y_0 - \frac{v_\perp}{\omega} \tag{3.8}$$

$$z = v_{z_0} t + z_0 \tag{3.9}$$

$$v_x = v_\perp cos(\omega t) \tag{3.10}$$

$$v_y = -v_\perp sin(\omega t) \tag{3.11}$$

$$v_z = v_{z_0} \tag{3.12}$$

where

$$\omega = \frac{qB}{\gamma m} \tag{3.13}$$

$\vec{v}_\perp$ is the perpendicular velocity around the direction of the magnetic field (in our case $\vec{v}_\perp = \vec{v}_x + \vec{v}_y$), and $\gamma = 1/\sqrt{1 - v^2/c^2}$ is the relativistic coefficient.

3.2.2 Testing the Interpolation Scheme

The MHD data given to us consists of magnetic and electric field values distributed on a discrete grid. The particle is free to move at any position inside the numerical box and at any time between the snapshots. This requires interpolation in two space dimensions and time, which causes some numerical error. Our code uses a 2-Dimensional linear interpolation method in order to calculate the magnetic and electric fields at any position inside the numerical box and at any time in between the snapshots known by bi-linear interpolation. Thus we interpolate first in position inside the numerical box for the 2 snapshots, the one exactly before the time step now under operation and the one exactly after. After position interpolation in the 2 snapshots, we interpolate in time, hence the problem could be viewed as a 3-dimensional interpolation separated into 2 steps. Figure 3.1 clarifies the idea of interpolating inside the numerical box. Consider any particle at a position (x_p, y_p) and at any certain time t_p, and take $f_{old}(x_p, y_p)$ and $f_{new}(x_p, y_p)$ to be any interpolated functions in the old and new snapshot respectively. Also let $F(x_p, y_p, t_p)$ to be the final interpolated function in space and time, then we have:

$$f_{old}(x_p, y_p) = (1-\delta_x)(1-\delta_y) f_{old_{i,j}} + \delta_x(1-\delta_y) f_{old_{i+1,j}} + (1-\delta_x)\delta_y f_{old_{i,j+1}} + \delta_x \delta_y f_{old_{i+1,j+1}} \tag{3.14}$$

$$f_{new}(x_p, y_p) = (1-\delta_x)(1-\delta_y) f_{new_{i,j}} + \delta_x(1-\delta_y) f_{new_{i+1,j}} + (1-\delta_x)\delta_y f_{new_{i,j+1}} + \delta_x \delta_y f_{new_{i+1,j+1}} \tag{3.15}$$

$$F(x_p, y_p, t_p) = (1 - \delta_t) f_{old}(x_p, y_p) + \delta_t f_{new}(x_p, y_p) \tag{3.16}$$

where

$$\delta_x = \frac{x_p - x_i}{x_{i+1} - x_i} \tag{3.17}$$

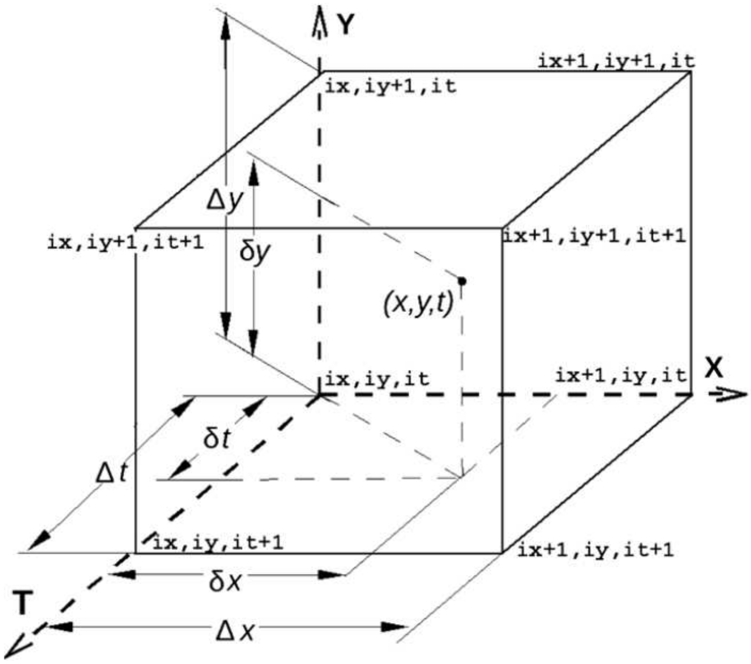

Figure 3.1: The numerical box having two dimensions in space (x and y) and one in time where the 6 field components are interpolated linearly to the particle position (figure taken from Gordovskyy et al. (2010b)).

$$\delta_y = \frac{y_p - y_j}{y_{j+1} - y_j} \tag{3.18}$$

$$\delta_t = \frac{t_p - t_k}{t_{k+1} - t_k}. \tag{3.19}$$

One way of checking that there is no major errors in the interpolation method is by varying Nx_{grid} and Ny_{grid} quantities, the number of grids in x and y respectively, which should not influence the difference between analytical and numerical results at any step as we are using uniform fields where values of electric and magnetic fields do not change from one point to another. Also if we output the values of electric and magnetic fields at each iteration we should notice that there is no change in their quantities as they are all the same. Of course this does not really test interpolation method fully but serves as a good test for fatal mistakes. In order to do that we perform 3 experiments (1, 2, and 3) all having the same initial conditions but with the only difference in the $Nx_{grid} = Ny_{grid}$ values where we took them to be 16, 128, and 256 respectively. The initial conditions and input parameters are shown in table 3.1. It is worth mentioning that the above values are chosen arbitrary, and some of the characteristic values like L_0 are not consistent with real values of the

$Calculation$	$Non-Relativistic$
$Method$	$RK4$
$Particle$	$Proton$
B_0	$0.01\ T$
L_0	$10\ m$
t_0	$10^{-6}\ sec$
E_0	$10^5\ V.m^{-1}$
V_0	$10^7\ m.s^{-1}$
$(\frac{q}{m})_0$	$10^8\ C.Kg^{-1}$
x_0	$20/L_0$
y_0	$30/L_0$
z_0	$10/L_0$
v_{x0}	$1.5 \times 10^5/V_A$
v_{y0}	$10^5/V_A$
v_{z0}	$1.5 \times 10^5/V_A$
t_{snap}	10
$t_{initial}$	$t_{snap} = 10$
t_{max}	40
$x_{min},\ y_{min}$	0
x_{max}	$80/L_0$
y_{max}	$60/L_0$
$\vec{B} = (\vec{B}_x, \vec{B}_y, \vec{B}_z)$	$(0, 1, 0.2)$
$\vec{E} = (\vec{E}_x, \vec{E}_y, \vec{E}_z)$	$(0, 0, 0.01)$
$Time\ Step$	$Non-Adaptive$
$Precision$	0.1

Table 3.1: Initial conditions and input parameters for the first 3 experiments (not chosen for any physical reason).

corona, since this is just for purpose of testing the code. The initial time is equal to zero ($t_{ini} = 0$) for the analytical solver and to the snapshot time ($t_{ini} = t_{snap}$) for the numerical solver where the particle begins to move from the first snapshot taken (it could be taken to be any time between any existing snapshots, but it could not be equal to zero or anything less than t_{snap} as this will cause problems). We pick 2 steps to test the interpolation, one in the middle and the second is the final step at $t = t_f$. After running the 3 experiments we notice that the errors between analytical and numerical solutions at the 2 steps for the 6 phase-space components are exactly the same. The gyro-period was constant all over the simulation as expected and the interpolation was also constant, that is the values of $B_x,\ B_y,\ B_z,\ E_x,\ E_y,\ and\ E_z$ did not change during the simulation as they are uniform. Figure 3.2 shows the result of plotting the exact and numerical solutions on the same graph where they coincide on top of each other. The solid black line refers to the exact one and dashed blue one refers to the numerical one. Table 3.2 shows the difference between analytical and numerical results at the final step along with the gyro-period in dimensionless unit.

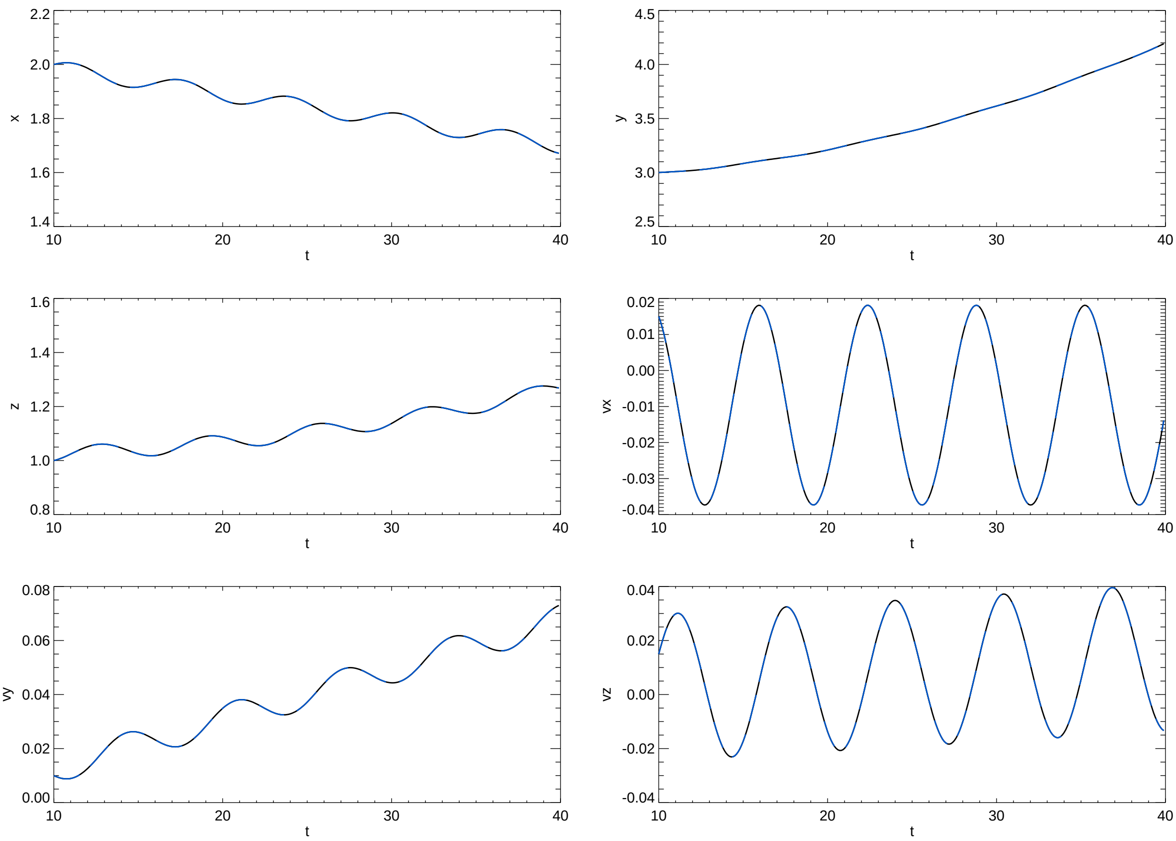

Figure 3.2: Analytical (solid black) and numerical (dashed blue) results of experiment 1. Panels from top to bottom are x, y, z, v_x, v_y, and v_z as labelled in each graph. we can notice drifting in the negative x direction due to the $\vec{E} \times \vec{B}$ drift together with gyration in x and z. Acceleration takes place in z and y directions. Same results are obtained for experiments 2 and 3 with exactly the same error results as expected.

3.2.3 Testing the Runge-Kutta 4th order Method

It is obvious from figure 3.2 that analytical and numerical solutions apparently coincide but this does not mean that the method is running properly. It is known that the error at each time step using a 4th order numerical methods deduced from

$diff_x$	$1.46.10^{-7}$
$diff_y$	$1.20.10^{-7}$
$diff_z$	$6.00.10^{-7}$
$diff_{vx}$	$5.98.10^{-7}$
$diff_{vy}$	$2.80.10^{-8}$
$diff_{vz}$	$1.40.10^{-7}$
$gyro - period$	6.43

Table 3.2: The error at the final step ($t = t_f = 40$) between analytical and numerical calculations for the first 3 experiments all having the same values as using uniform and static magnetic and electric field lines.

Taylor expansion is Δt^5 i.e.

$$error = |f_{exact} - f_{numerical}| \simeq C(\Delta t)^5 \tag{3.20}$$

where C is a constant and Δt is the time step. The accumulative error after n steps is reduced to Δt^4 as $n = t/\Delta t$, so global $error \propto \Delta t^4$. Taking the logarithm of both sides yields, when plotting Log(error) versus Log(Δt), a straight line of slope 4. To check if the method is running properly we perform 4 experiments having all the same initial conditions as experiment 1 but with different time steps as follows 0.1, 0.05, 0.025, and 0.0125 (we divide by a factor of 2 rather then 10 to avoid reaching the limit of *double precision*). The first one is actually experiment 1, so we need to perform experiments 4, 5, and 6 with the other 3 values of Δt. We also choose the final step to be our testing point. Figure 3.3 shows a logarithmic plot for the 6 phase-space components each represented by a coloured curve for experiments 1, 4, 5, and 6. We can notice that the 6 lines are approximately parallel, then we can say that they have the same slope. Taking any of the lines and calculating its slope, lets say the y-trajectory values, gives $slope$ = 4.00 exactly. We can conclude that our RK4 method is working properly (an explanation on how the RK4 method works is found in Appendix A.5).

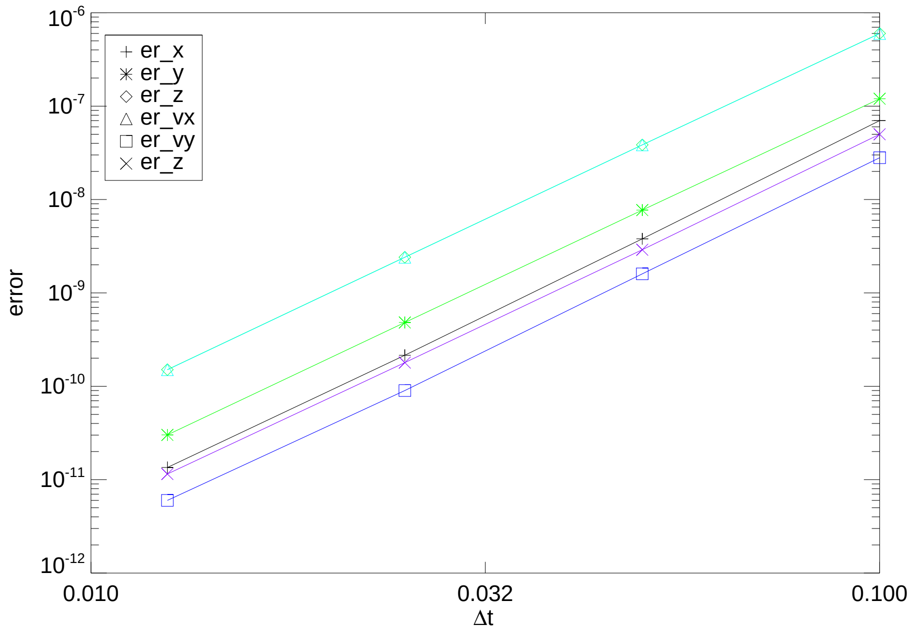

Figure 3.3: *Error* vs. Δt on a logarithmic scale for the 6 phase-space components for experiments 1, 4, 5, and 6. The 6 lines are approximately straight and parallel to each other with a $slope = 4$ indicating that RK4 method is working properly. The error in z and v_x are very close that is why the 2 lines seems to be on top of each other using a logarithmic plot.

3.2.4 Testing the Adams-Bashforth 4th Order Method

Using the same method to test RK4, we perform a set of 4 experiments (7, 8, 9, and 10) with same time steps as used before i.e. Δt=[0.1, 0.05, 0.025, 0.0125] and with the same initial conditions as used in experiment 1. Figure 3.4 shows the same thing as in figure 3.3 but this time for A-B4 method (an explanation on how the A-B4 method works is found in Appendix A.6). Also in this figure we can notice that the 4 lines are approximately parallel and when calculating the slope for any arbitrary line, say for instance v_x, we get $slope = 3.99$. One interesting thing we should note here when comparing the efficiency between the two numerical methods used, is that RK4 method is more accurate. It always gives less error at any certain time step than A-B4. Looking at the y-axis in figures 3.3 and 3.4 shows this. The error decreases in RK4 with decreasing time step from orders of magnitude of -8 when $\Delta t = 0.1$ till -11 at $\Delta t = 0.0125$, while in case of A-B4, error converges from -6 till -9 or -10, which infer that RK4 could reach to accuracy of 2 orders of magnitude better than A-B4.

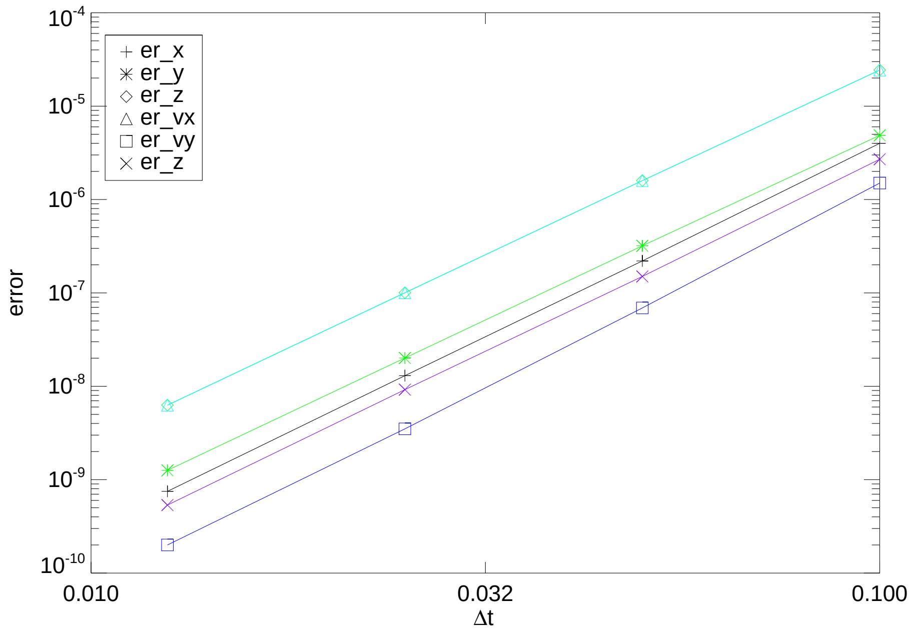

Figure 3.4: Same discussion as figure 3.3 but for Adams-Bashforth method using experiments 7-10. For some reason the error in z and v_x always show close results.

A good question here may be about which of the 2 methods perform faster. To answer this question, we put time-marks on the loops which solve the differential equations for the 2 methods. Using same initial conditions, we notice that there is no big difference. The program was very fast and the particle moves through the whole domain (crossing one the boundaries, where simulation stops) or consuming all the time (t_f=t_{max}, were simulations stops also) by a fraction of a second using the 2 methods. Hence RK4 seems to be more accurate, that is why we use it in the future.

3.2.5 Relativistic VS. Non-Relativistic Calculation

So far we checked that the interpolation and differential equation solvers are working properly, what remains to check is relativistic and non-relativistic modules and determine when relativistic calculation is required. Finally we will check if everything works for electrons as well as protons. To test relativistic and non-relativistic calculations we perform 4 experiments also with protons. Experiment 12 and 13 confirms that relativistic module agrees with the non-relativistic when particles have low speeds and experiments 14 and 15 aims to show that relativistic effects cannot be ignored when working with relativistic speeds as it is known. The configurations of magnetic and electric fields in this section are changed for the purpose of getting an analytical solution using the relativistic version of Lorentz equation of motion as discussed in § 3.2.1. In this new configuration where electric field is set up to zero and magnetic field is directed in the z-direction, the motion of any charged particle will be a simple helix where it gyrates in the $x-y$ plane and move with a constant velocity in the z-direction. As the electric field is zero then we expect the kinetic energy to be constant all the way, along with the perpendicular velocity (in our case $\vec{v}_{\perp} = \vec{v}_x + \vec{v}_y$). As we are using non-relativistic speeds in the first test (experiments 12 and 13) then we expect gamma (γ) to be close to unity through out the whole simulation. The initial velocities (before normalisation) were set as follows, $v_{x_0} = v_{z_0} = v_{\perp} = 0.5 \times 10^{-4}c,\ v_y = 0$, where c is the speed of light. We perform the simulation with the relativistic module in experiment 12 and with the non-relativistic module in experiment 13. Figure 3.5 shows the results for both experiments in the same graphs, where dashed blue lines correspond for relativistic values and solid black lines for non-relativistic one. It is easily noticeable that the 2 modules coincide in all phase-space components as expected. The value of γ was viewed in each iteration and it was always equal to 1. $v_{\perp}$ was also constant and equal to 0.015 as v_{x_0} (after dividing by the characteristic velocity V_A). The kinetic energy was constant as well. It is worth noting that analytical solutions for both experiments also coincide on top of the 2 curves in each plot (one can wonder that there should be a very small numerical error i.e. γ very close to 1 but not equal to 1, kinetic energy is constant but with a small percentage change and so on. We say that theoretically, $\gamma = 1.000000003$, for our chosen velocities and so the change occurs in the 9th decimal digit which could not appear in our output data files). Now we consider the case where speeds become relativistic and perform experiments 14 (with relativistic module) and 15 (with non-relativistic module). The initial velocities are as follows, $v_{x_0} = v_{z_0} = v_{\perp} = 0.5c,\ and\ v_y = 0$. As before, kinetic energy,

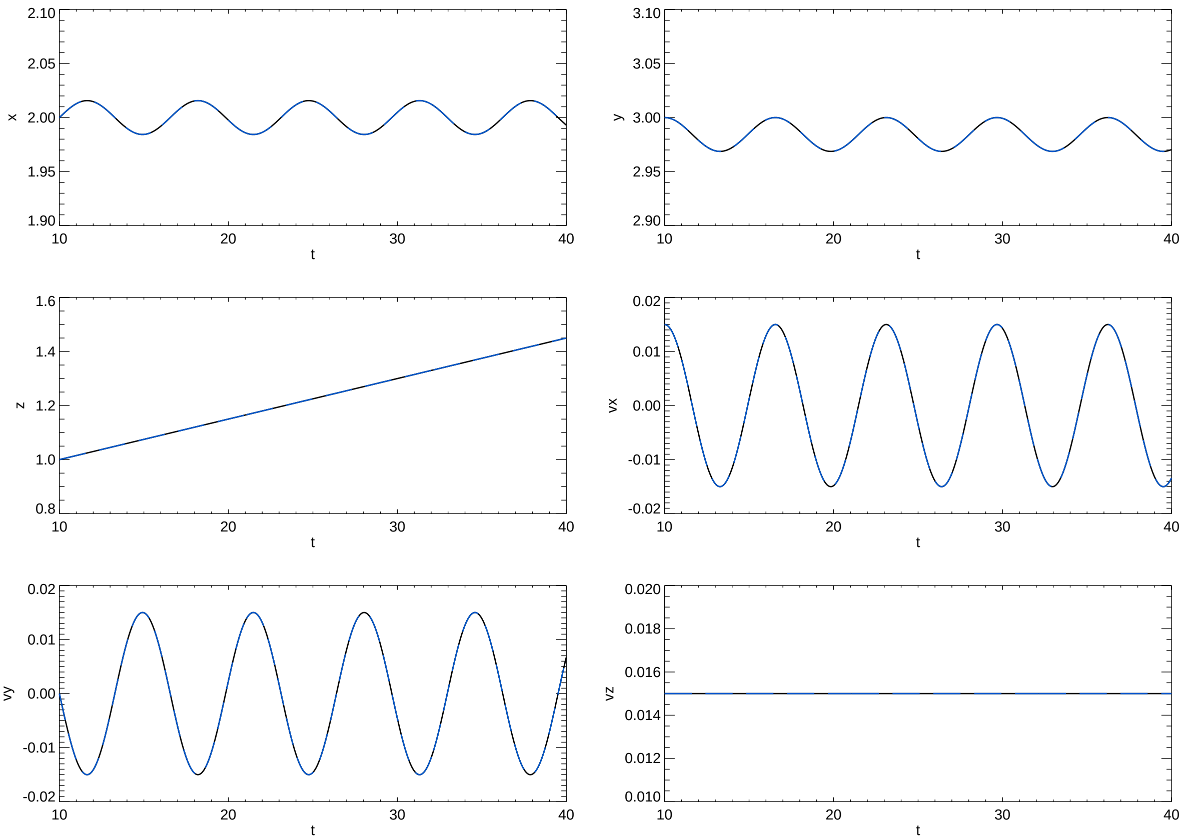

Figure 3.5: Relativistic (dashed blue) and non-relativistic (solid black) calculations for the 6 phase-space components using low speeds ($v_{x_0} = v_{z_0} = 0.5 \times 10^{-4} c/V_A = 0.015(dimensionless)$). Both calculations give similar results where $\gamma \cong 1$, hence relativistic effects are ignored. Analytical results for both calculations also coincide on top of the 2 curves.

γ, and $v_\perp$ should be constant as no electric field exist. There values are:

$$E_K = mc^2(\gamma - 1) = 389.2MeV, \tag{3.21}$$

where $\gamma = 1.41421$ and

$v_\perp = 15$ ($in\ dimensionless\ units$).

At each time step we viewed γ, $v_\perp$, and E_k and the results were exactly as we expected concerning values and the constancy of these parameters. The same thing was done in experiment 15 but with the non-relativistic module. Figure 3.6 shows the results of the 6 phase-space components for both experiments on the same graphs together with their corresponding analytical results. We can notice that curves in each plot except for z (constant all the way) and v_z (linear with time) do not match and this what we were expecting when using relativistic speeds. However, there is very good agreement between the numerical relativistic solution and its analytical one. If we discuss the issue from the energy side, the picture is more informative. Protons have a rest mass of 938.272 MeV/c^2 while that of electrons is 0.511 MeV/c^2. Simulations show that protons and electrons can gain energy of hundreds of MeV. As the rest mass of electrons is so small compared to that of protons then the latter need high speeds very close to the speed of light in order for the relativistic effects to significantly affect its trajectory. Even in our last experiment the disagreement is obvious, but the motion in general is the same and the kinetic energy is less then the rest mass. Hence we would say that relativistic effects are less important for the case of protons. As most of our coming experiments are for protons simulations, non-relativistic module will be mainly in use.

3.2.6 Electron Testing

Now after testing interpolation, methods, and relativistic and non-relativistic modules, what remains is to test the code using electrons rather than protons as the numerical error may be larger due to thier smaller gyro-period. We will not re-test all aspects of the modules as we did before, but we will set one experiment to see if we get the expected behaviour. To do so, we perform experiment 16 with mainly the same conditions as experiment 1 but with some differences listed in table 3.3. We expect electrons to have a similar behaviour as protons in experiment 1 with

y_0	$55/L_0$
v_{x_0}	$1.5 \times 10^6/V_A$
v_{y_0}	$1 \times 10^6/V_A$
v_{z_0}	$1.5 \times 10^6/V_A$
$Time\ Step$	$Adaptive$
$Precision$	0.01

Table 3.3: Changed initial conditions and input parameters for experiment 16.

gyrations in the x and z directions and moving in the negative y-direction rather than the positive one as in experiment 1. As $\vec{E} \times \vec{B}$ drift does not depend on the

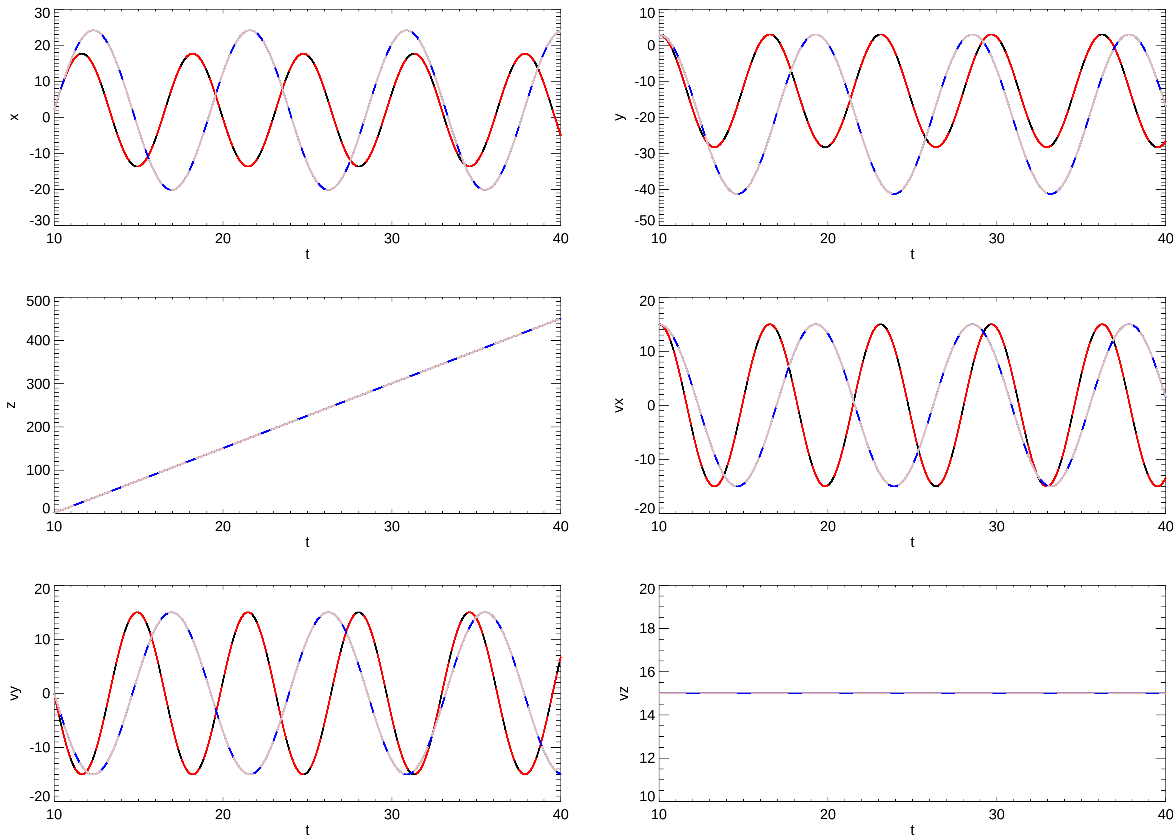

Figure 3.6: Relativistic-analytical (dashed gray), relativistic-numerical (solid blue), non-relativistic-analytical (dashed red), and non-relativistic-numerical(solid black) calculations for the 6 phase-space components using relativistic speeds. Relativistic effects are no more ignored and influence a lot on the path of the particle especially in the directions of gyrations. Analytical and numerical results always coincide within the same calculation.

charge of the particle so protons and electrons should drift in the same direction (in our case the negative x-direction). After running the experiment, it stops at $t = 12$ as the particle travel all the way down from $y = 5.5$ till $y = 0$ in this small duration of time. This small time does not mean a small number of iterations, in fact there was a lot of iterations as the time step is very small. Figure 3.7 shows the results of experiment 16 for the analytical and numerical solutions. We zoom in inside the curves in order to resolve gyrations in x and z directions that is why the time in the figure is just from $t = 10$ till $t = 10.15$ in most of the plots. The error at the final step was as expected very small, confirming that every thing is running properly (results shown in table 3.4).

$diff_x$	$3.99.10^{-8}$
$diff_y$	$7.40.10^{-10}$
$diff_z$	$3.43.10^{-9}$
$diff_{vx}$	$6.28.10^{-6}$
$diff_{vy}$	$1.40.10^{-5}$
$diff_{vz}$	$7.02.10^{-5}$
$gyro-period$	0.0035

Table 3.4: The error at the final step between analytical and numerical calculations for experiment 16 simulating an electron trajectory. The gyro-period is always much smaller for the case of electrons as they are more magnetised than protons due to their tiny mass.

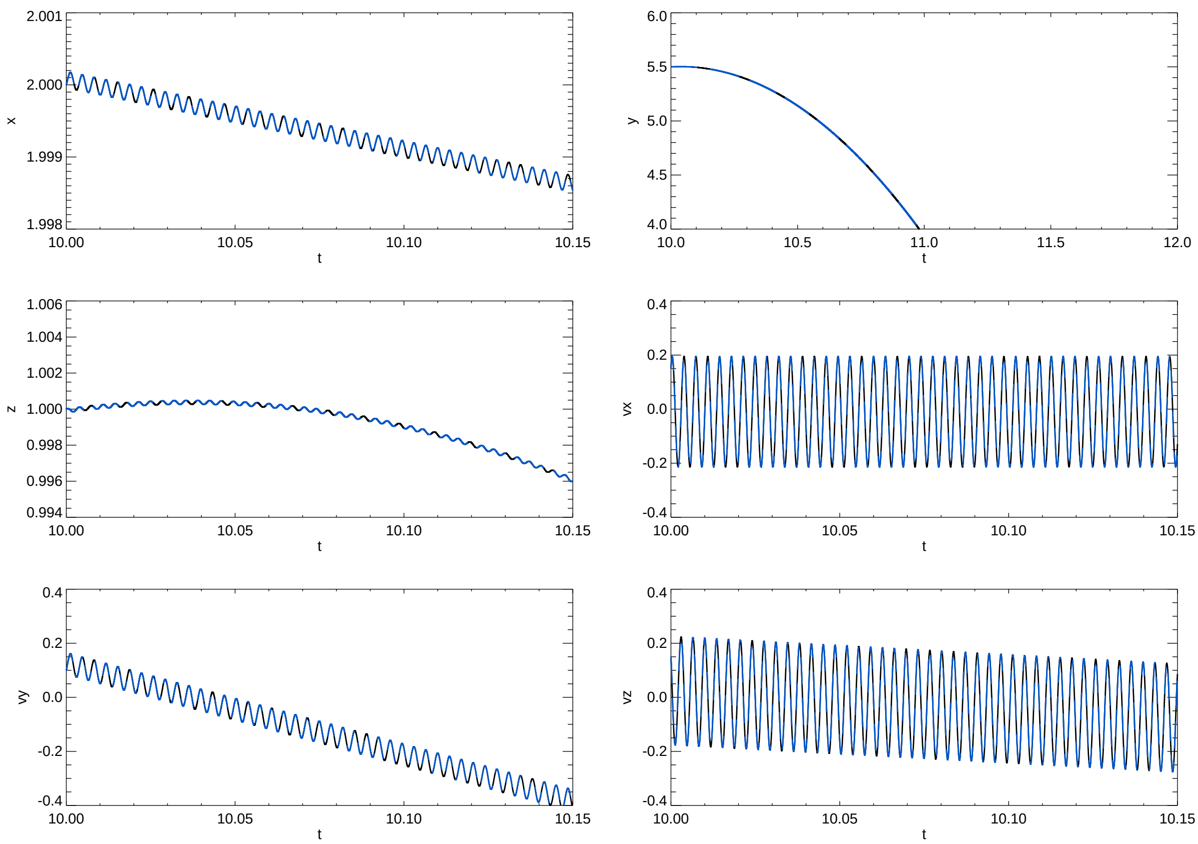

Figure 3.7: Results of experiment 16 simulating electron trajectory. Black solid curves correspond to analytical solutions and blue dashed one for numerical one. Coincidence is also insured by the small error values at the last iteration as stated in table 3.4.

3.3 Testing the Drift Theory

After testing the code using uniform and static fields indicating that it is working properly, now we can move on to the case of non-uniform field lines or more precisely the non-uniform magnetic fields. In this case no analytical solution exists, but an approximate solution can be find under appropriate conditions within the Guiding Centre Approximation (GCA) theory (see § 2.2). We compare our numerical solutions with GCA solutions for simple model fields in which the drift velocities can be calculated exactly. The purpose of this is to test the validity of GCA when varying specific parameters which could break down GCA conditions.

3.3.1 Field with ∇B Drift

We choose a field in which the only drift velocity is the ∇B drift. Thus we take the magnetic field lines to be directed in the positive z-direction and varying in the y-direction, thus $\nabla\vec{B}$ will be $\perp$ to $\vec{B}$. The mathematical formula for the field is:

$$\vec{B} = \alpha(y+\delta)\vec{k}, \tag{3.22}$$

where α is a constant used to vary the strength of the magnetic field, and δ is also a constant used to avoid getting $B = 0$ at $y = 0$ (particles become un-magnetised in this case). The electric field is set to zero. Following up from § 2.2 we get:

$$v_{gc} = \mp\frac{v_\perp r_l}{B}\frac{1}{2}\frac{\partial B}{\partial y}\vec{x} \tag{3.23}$$

The main condition for the guiding centre theory to be satisfied is that the Larmor radius should be much smaller than the length scale of the system, that is:

$$\frac{r_l}{L} \ll 1 \tag{3.24}$$

In our case, the length scale of the system is the distance where the magnetic field changes ($L_{\nabla B}$) given by the following formula:

$$L_{\nabla B} = \frac{|\vec{B}|}{|\partial\vec{B}|} = \frac{|\alpha(y+\delta)|}{\alpha} = y+\delta \tag{3.25}$$

and thus after substituting in $r_l/L_{\nabla B}$ and knowing that $r_l = \frac{mv_\perp}{qB}$ we get:

$$\frac{r_l}{L_{\nabla B}} = \frac{mv_\perp}{q\alpha(y+\delta)^2}. \tag{3.26}$$

Deriving the guiding centre velocity gives:

$$v_{gc} = \frac{mv_\perp^2}{2q\alpha(y+\delta)^2} \tag{3.27}$$

As $\vec{B}$ is in the z-direction and it is varying in the y-direction and we are using protons, then we expect the test particle to drift in the negative x-direction in a linear way where the Larmor radius does not change but the particle itself drifts slightly after each gyration.

3.3.2 Simulations and Results

Here we perform 7 experiments, aiming to calculate test particle trajectories in non-uniform magnetic fields given by equation 3.22. The main difference between these 7 experiments is the value of $r_l/L_{\nabla B}$ where we begin from small values satisfying the condition as stated in equation 3.24, where as we shall notice that the guiding centre approximation agrees with our exact trajectory calculations and then begins to increase the value of $r_l/L_{\nabla B}$ gradually until approaching 1, where we expect a large difference between the GCA theory and our simulations. The guiding centre drift velocity is calculated using 2 methods. First by using equation 3.27 giving us the value of v_{gc} from the GCA theory. v_{gc} is calculated also from our simulations by calculating the slope in the drifting direction. The particle with our chosen configuration of magnetic field should be drifting linearly downwards in the x-direction governed by the following equation:

$$x = v_{gc}t + x_0. \tag{3.28}$$

For each gyration we get the maximum and minimum values in the x-direction (the drifting direction) using a C++ script together with their associated time and

α	3
$B0$	1
c	10
x_0	$20/L_0$
y_0	$110/L_0$
z_0	$0/L_0$
vx_0	$1.5 \times 10^7/V_A$
vy_0	$1.5 \times 10^7/V_A$
vz_0	$0/V_A$
y_{min}	10
y_{max}	$60/L_0$
Time Step	*Adaptive*
Precision	0.01

Table 3.5: Initial conditions and input parameters for experiment 17 testing grad drift theory at applicable GCA regime.

calculate the midpoint which is the position of the guiding centre in the x-axis together with its approximated time. Knowing the position of the guiding centre at each time allows us to calculate the slope of motion which is the drift speed. The 7 experiments are labelled from experiment 17 till 23. The initial conditions and input parameters for experiment 17 are presented in table 3.5 (Calculation, Method, Particle, Characteristic values, t_{snap}, t_{max}, t_i, x_{min}, x_{max} are the same as experiment 1). Changes made for other experiments are stated later on. In this experiment the value of $r_l/L_{\nabla B} = 1.67 \times 10^{-3} \ll 1$, so the GCA theory would be valid. Calculating v_{gc} from the theory as in equation 3.27 gives us, $v_{gc} = -1.7751 \times 10^{-3}$, and calculating the slope of the drifting motion from our simulations as shown in figure 3.8 gives, $slope = -1.774 \times 10^{-3}$, and hence the error given in the following formula:

$$error = \frac{|v_{gc} - slope|}{|v_{gc}|} \tag{3.29}$$

would be 0.06%. In experiment 18 we just increase the velocities v_x and v_y to 10^8 and thus $r_l/L_{\nabla B} = 0.01$ which may also be considered as $\ll 1$. In this experiment, $v_{gc} = -0.078893$, and the slope of the drifting line in our simulation is -0.0801, and thus the error is 1.558%. So we notice that the error had increased when $r_l/L_{\nabla B}$ approaches 1. In experiments 19, 20, 21 and 22 we decreased α from 3 to 2, 1, 0.7, and 0.3 respectively in order to increase $r_l/L_{\nabla B}$ slightly as it is inversely proportional

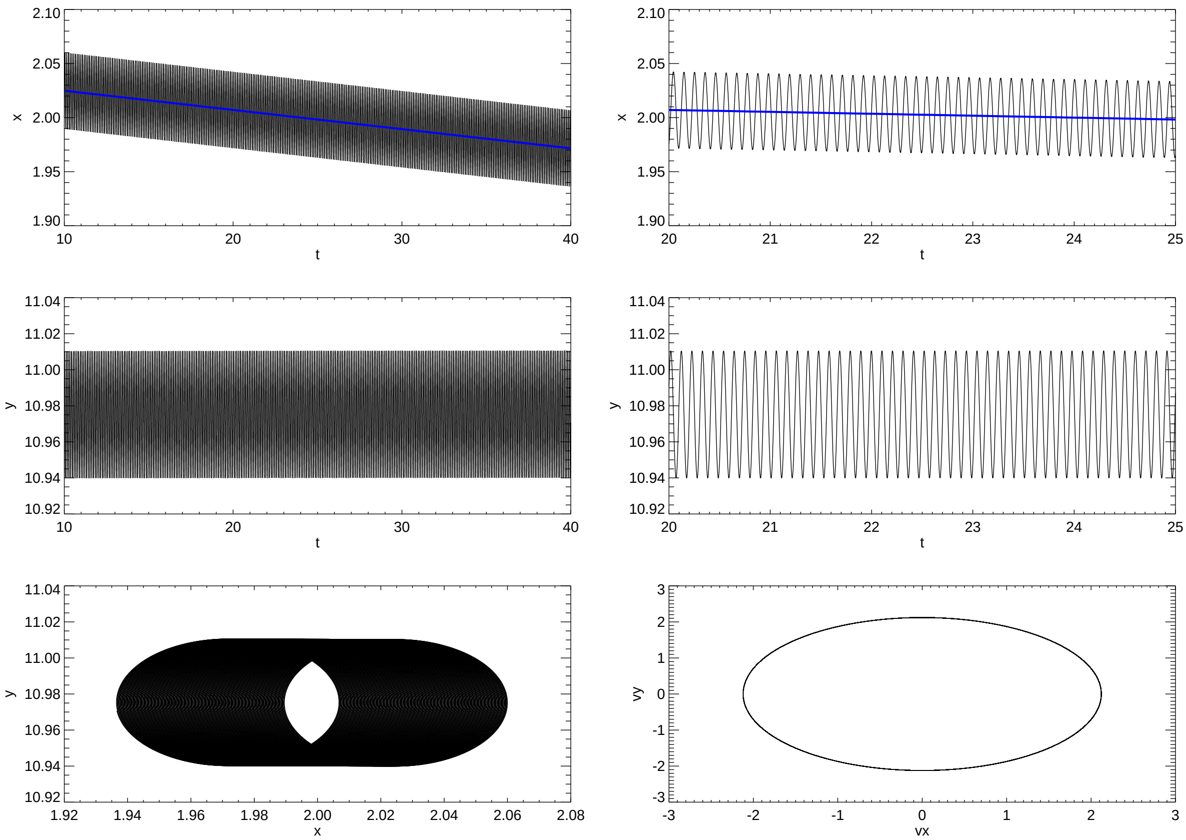

Figure 3.8: Results for experiment 17. The 1^{st} panel shows x vs. *time* where the test particle drifts in the negative x-direction due to the grad drift. The blue line represents the motion of the guiding centre in the x-direction drifting linearly downwards. The 2^{nd} panel (top right) is just zooming inside the first panel to reveal the plot structure. The 3^{rd} panel is y vs. *time* where the particle oscillates normally in this direction and a little bit of zooming in the 4^{th} one. The 5^{th} panel show a complete picture of dense oscillations in $x-y$ plane and drifting in the x-direction. The final panel shows v_y vs. v_x where all circles here accumulated above each other to indicate that the Larmor radius is not varying throughout time, it also gives an idea on the shape of gyrations in the $x-y$ plane.

to α getting values of 0.0167, 0.031, 0.0435, and 0.1 respectively. As a result the error increased to 2.37%, 4.5%, 6.2%, and 17.33% respectively. Figure 3.9 shows results for experiment 20 with same analysis as for figure 3.8 but with an increase in the error. We should note that the number of gyrations is decreasing as viewed in the figures due to the increase in the gyration period given by following formula:

$$T_c = \frac{2\pi m}{q\alpha(y+\delta)} \tag{3.30}$$

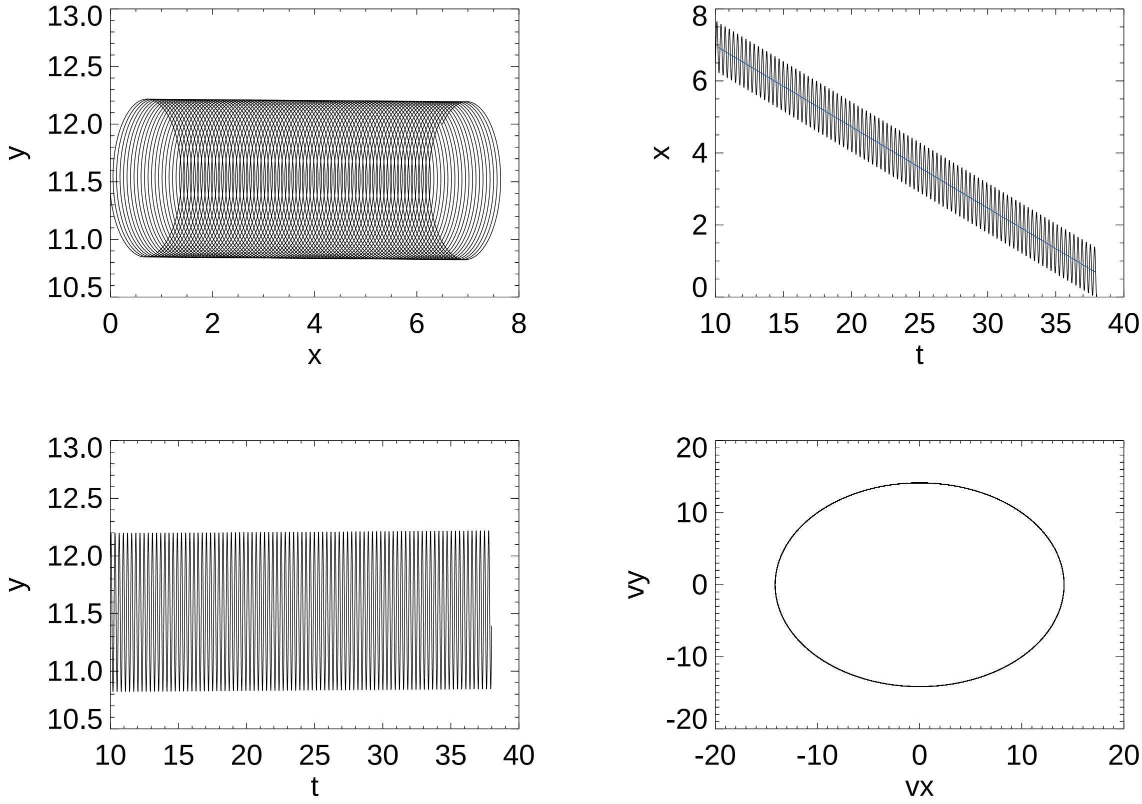

Figure 3.9: Results for experiment 20. Same discussion as in figure 3.8 but in this experiment the GCA become slightly less valid as $r_l/L_{\nabla B}$ is increased a little bit, also the number of gyrations is less as discussed above.

so as we decrease α, T_c increase and as $f_c = 1/T_c$ so the number of gyration decreases. Also it is worth mentioning that in some experiments as in 21 and 22 we were obliged to enlarge the boundaries of x and y as the Larmor radius given by the following formula:

$$r_l = \frac{mv_\perp}{q\alpha(y+\delta)}, \tag{3.31}$$

and is increasing with decreasing α that could in some cases be larger than the initial boundaries.

Finally we perform experiment 23, but before going through the details, we should note that we find a difficulty in choosing the numbers for this experiment as we have limited choices when we approach 1. The Larmor radius becomes very large to the extent that we cannot achieve even one gyration. We tried to find a high value for $r_l/L_{\nabla B}$ that would make some gyrations but show a huge difference between theory and simulations by keep decreasing y in equation 3.22 as much as we can till the value of y itself becomes a problem i.e. the particle crosses the boundaries in this direction and thus the simulation stops. we take α to be 0.0241 (a value that we calculated first to make $r_l/L_{\nabla B} = 0.5$ and choosing y=25, but it turns out that it does not work and the particle even did not complete one gyration, but any way we keep using it), also we enlarge the boundaries such that $y_{min} = 1$, $y_{max} = 50$, $x_{min} = 0$, and $x_{max} = 200$, hence here some useful values, $r_l/L_{\nabla B} = 0.2761$ (very close to 1), $r_l = 13$ (so large), $v_{gc} = -1.95$ (very fast drifting). The slope of drifting from our simulations is $= -4.77$ and so the error is 144% which indicates that the GCA is no more valid in such cases where $r_l/L_{\nabla B}$ is not much smaller than 1. However, the behaviour still qualitatively follows drift theory, just the value of the drift speed is quite inaccurate. Figure 3.10 shows results for experiment 23 where we can just see 3 gyrations from the simulations where time runs out before completing the fourth one due to the large gyration period. If we plot the influence of increasing $r_l/L_{\nabla B}$ on the accuracy of GCA using the preceding 7 experiments on a logarithmic plot as shown in figure 3.11, we could notice an approximately linear relation between Log(error) and Log($r_l/L_{\nabla B}$) of slope ~ 2 with some deviation. Thus we can say that, $error \propto (r_l/L_{\nabla B})^2$, which is true, as within the derivation of GCA, the second order of the parameter $r_l/L_{\nabla B}$ is always ignored because it is too small.

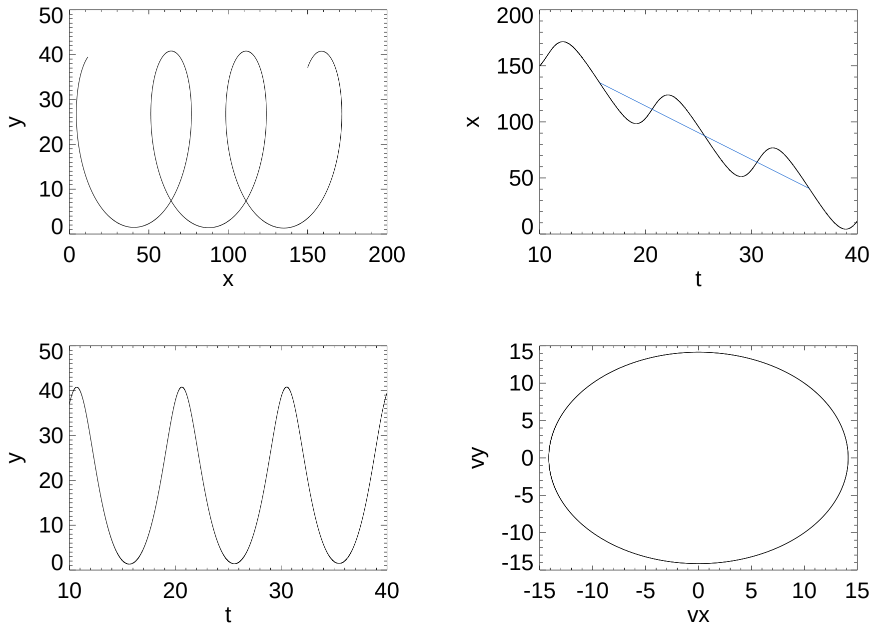

Figure 3.10: Results for experiment 23. The GCA is no more valid, but we can always notice the drifting in the negative x-direction. The guiding drift velocity no longer agrees with that calculated from the GCA. It is worth noting that in all cases, particles simulated in exact trajectories drift faster than what it is approximated.

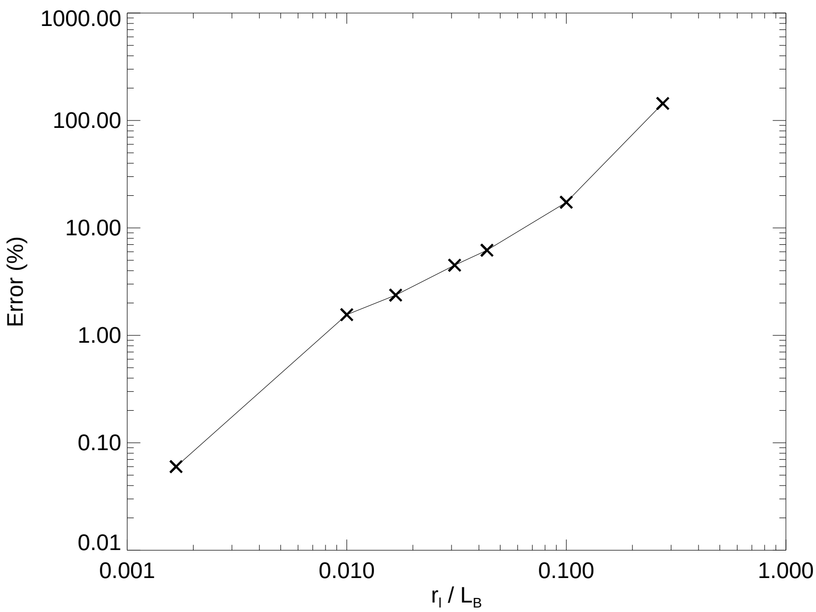

Figure 3.11: Logarithmic plot of $r_l/L_{\nabla B}$ vs. error(%) showing an approximate linear relation between Log(error) and Log($r_l/L_{\nabla B}$) of slope $\sim$ 2 with some deviation. This indicate a squaring relation between error and $r_l/L_{\nabla B}$ justified by the basic assumption made when deriving GCA in ignoring the term $(r_l/L_{\nabla B})^2$.

Chapter 4

Trajectory Calculations For Analytical Fields

All that we did in the previous chapter can be considered as a testing procedure to check if our code is working properly and it appears to be. Now we can go a step further and perform simulations using more realistic MHD data using the 2 approaches (approximation approach using an already written and tested Guiding Centre Approximation Code (GCA), and our full trajectory code) and we shall compare the results. However, before investigating numerical MHD data, it is interesting to compare full trajectory and GCA using analytical field models. This could be done using two approaches. Firstly, we calculate trajectories using both codes with analytical fields within the codes i.e. using exact values of fields with no interpolation from finite grid, and secondly we use the same analytical expressions but map these to a discrete grid. In this way we can figure out what are the effects of interpolation and using numerical data on grid points on the trajectory of a particle. Two variables should be taken into account, the first is the grid size, Nx_{grid} or Ny_{grid}, and second is the dimensionless mass-to-charge ratio, q/m, called α related to the dimensionless Larmor radius. When changing the grid size at a fixed mass-to-charge ratio, and calculating the error between analytical calculations using analytical fields and numerical calculations using analytical fields in grid points, we could specify the critical or the minimum grid size that should be used later on when

L_0	$10^4\ m$
ρ_0	$4 \times 10^{-11}\ kg.m^{-3}$
B_0	$10^{-2}\ T$
V_A	$1.4 \times 10^6\ m.s^{-1}$
t_A	$7.1 \times 10^{-3}\ sec$
E_0	$1.4 \times 10^4\ V.m^{-1}$

Table 4.1: Realistic coronal values assigned for the 3 main normalising coefficients; Length, Density, and Magnetic Strength and the other coefficients, Alfven Speed, Alfven Time, and Electric Strength are calculated from the assigned one following up from MHD theory.

using pure numerical data. Also we could see how things go when increasing the grid size. Of course we expect the error to decrease as grid size decreases, but in which way? Furthermore, comparing things at fixed grid size and variable α would give us an idea about the limitations of the guiding centre theory. Similarly, we know that GCA should break down at larger α, but for what range of values does it give meaningful results? These comparisons will be made in this chapter, for analytical fields, and afterwards, for numerical fields.

4.1 The Model and System Formalism

The system in our current work will differ from what we had done before as we are now dealing with more realistic fields. Therefore, now the normalisation coefficients will be given realistic coronal values. The domain is defined s.t. x and $y \in$ [-2.0 , 2.0]. To insure that $\Delta x = \Delta y$, Nx_{grid} is always taken to be equal to Ny_{grid}. The basic normalising coefficients are ($L_0,\ \rho_0,\ and\ B_0$). We assign realistic coronal values to these coefficients as shown in table 4.1, and also corresponding values for V_A (Alfven velocity), t_A (Alfven time), and E_0 (characteristic electric field).

Concerning analytical forms of electric and magnetic fields, we tried to formulate them such that they could be similar to that postulated and observed to the case of particle acceleration in solar flares. The simplest relevant form is an X-shape magnetic field in the $x - y$ plane with a transverse magnetic field and electric field in the z-direction with constant values. The expressions are as follows:

$$B_x = B_0 \frac{y}{a} \tag{4.1}$$

$$B_y = B_0 \frac{x}{b} \tag{4.2}$$

$$B_z = B_0 \tag{4.3}$$

$$E_x = 0 \tag{4.4}$$

$$E_y = 0 \tag{4.5}$$

$$E_z = E_0 \tag{4.6}$$

Same or similar field configurations where used by many authors like [Speiser (1965); Litvinenko & Somov (1993); Litvinenko (1996); Browning & Vekstein (2001) and references therein]. If $a = b$, then we are assuming a two-dimensional potential magnetic field configuration (**j**=0), while if $a \neq b$, then a current exists such that, **j**=$\frac{B_0}{\mu_0}(1/b - 1/a)\ \vec{k}$. The GCA code needs the values of $\nabla|\vec{B}|$, $(\vec{b}.\vec{\nabla})\vec{b}$, $\frac{\vec{E}\times\vec{B}}{B^2}$, and $\vec{E}.\vec{b}$ on the grid points as an input. These values should be evaluated for the specified field configuration chosen and then programmed into the GCA code (there analytical forms can be found in Appendix A.7). The data was created and saved into data files using a C++ program. The magnetic field lines can be plotted by two ways; either by calculating the equation of field lines; or by calculating the z-component of the magnetic potential associated with the magnetic field given by the formula, $\vec{B} = \nabla\times\vec{A}$, as the current sheet lies on the $x-y$ plane, and making a contour plot. A_z can be calculated analytically by integrating the previous equation. Also we could evaluate the value of the $\vec{E} \times \vec{B}$ velocity and plot it as it shows how plasma inflows and outflows from the sheet. The derivations for this is presented in Appendix A.8. Figure 4.1 shows a contour plot for A_z in the defined domain (solid blue) along with $V_{\vec{E}\times\vec{B}}$ (dashed black) with arrows indicating how plasma inflows and outflows from the sheet. This ensures that our chosen configuration represents reconnection as plasma inflow in vertical direction and outflow in horizontal direction. The contour

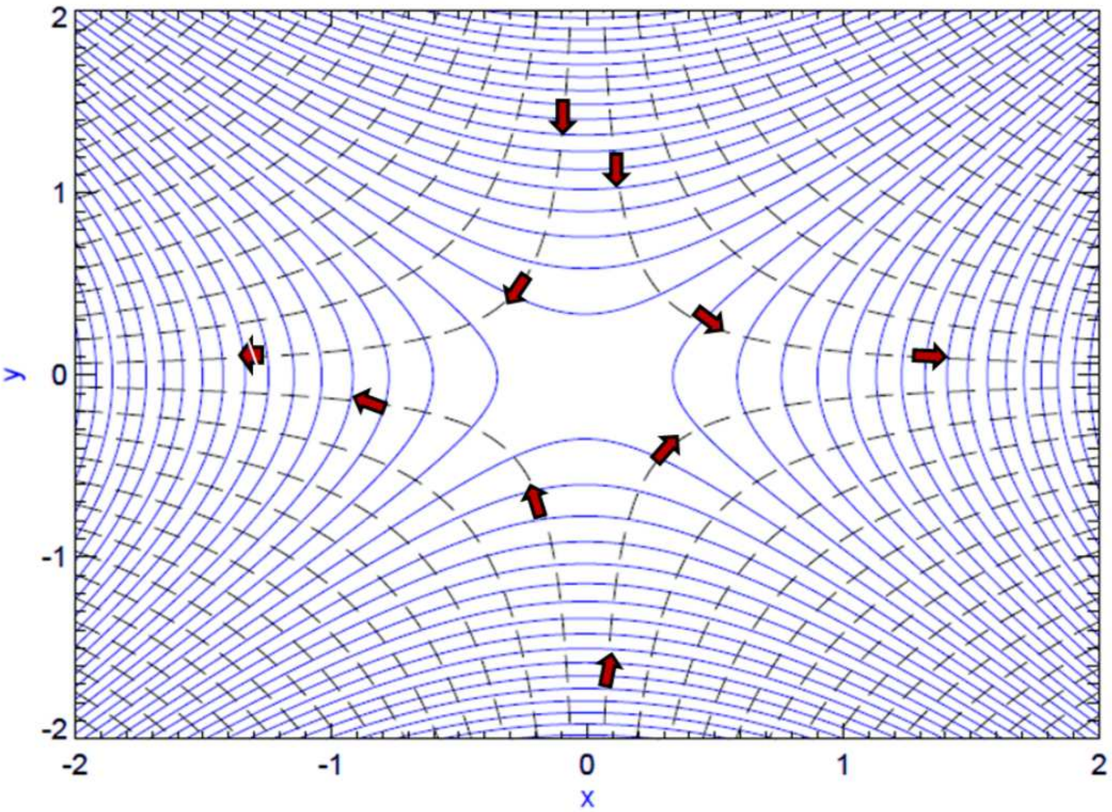

Figure 4.1: Magnetic field lines (solid blue) showing an X-shape configuration and $V_{\vec{E}\times\vec{B}}$ (dashed black) showing inflow of plasma in the x-direction and outflow in the y-direction indicted by the arrows in the $x-y$ plane (current-sheet plane). Reconnection is likely to occur with such configuration.

plot for A_z alone will be used as a background for our experiments to show how particles move within these magnetic field lines.

4.2 Switching

GCA codes use one parameter less than full trajectory codes. This parameter is the gyration-phase angle ϕ as GCA codes average over one gyration so there is no need to define this angle. Besides, in GCA versions, all velocity calculations are held in a basis perpendicular and parallel to the magnetic field ($V_\perp$ *and* $V_\parallel$). On the other hand, the full trajectory code performs simulations in the basis of a Cartesian Coordinate where (V_x, V_y, *and* V_z) are calculated in each step (see figure 4.2). Thus we need a switching procedure for which we can guarantee that we enter the same initial conditions in both codes. Initially the GCA code takes as an input, V_{ini}

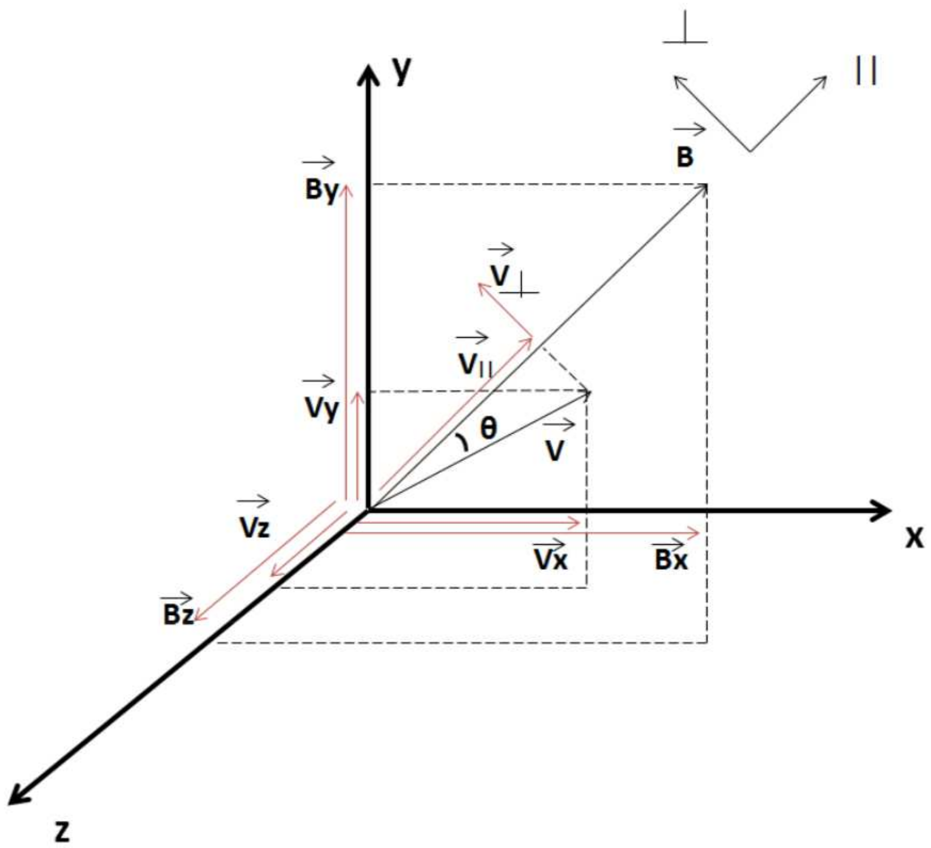

Figure 4.2: A schematic drawing showing the Cartesian components of the velocity together with the parallel and perpendicular one.

normalised to V_A, and $cos(\theta)\ \in$ [-1,1] s.t. $V_{\|} = cos(\theta)V_A$. In order to enter the same initial information to the full trajectory code, we define an arbitrary vector $\vec{e}$ and calculate initially the vector $\vec{b}$ which is the unit vector of the magnetic field. Then we create 2 new basis vectors ($\vec{a},\ and\ \vec{c}$) both $\perp\ \vec{b}$ s.t. $\vec{a} = \vec{e} \times \vec{b}\ and\ \vec{c} = \vec{a} \times \vec{b}$ and then we take $\vec{V_\perp} = |\vec{V_\perp}|(cos(\phi)\vec{a} + sin(\phi)\vec{c})$. After some extra algebra we end up by the following initial values for $V_x,\ V_y,\ and\ V_z$:

$$V_x = V_{\|}b_x\ +\ V_\perp cos(\phi)c_x\ +\ V_\perp sin(\phi)a_x$$

$$V_y = V_{\|}b_y\ +\ V_\perp cos(\phi)c_y\ +\ V_\perp sin(\phi)a_y$$

$$V_z = V_{\|}b_z\ +\ V_\perp cos(\phi)c_z\ +\ V_\perp sin(\phi)a_z \tag{4.7}$$

hence the full code can perform simulations with same initial values entered to the GCA code.

4.3 Experiments

Now everything is ready to begin performing simulations. What remains is to specify the values associated to the variables a, b, E_0, B_0, initial speed (V_{ini}), pitch angle (θ) (see table 4.2), Nx_{grid}, and α. One problem faced us with Nx_{grid} is that the maxi-

a	1
b	1
E_0	5
B_0	1
V_{ini}	0.1
$cos(\theta)$	0.8

Table 4.2: All values are normalised to their characteristic coefficients except $\cos(\theta)$.

mum value for a 2 dimensional array that could be used in our machine is 508 where beyond this number a segmentation error happens, and as Nx_{grid} would always be preferred to be a power of 2, then the maximum number would be 256. Later on we learnt how to overcome this problem by using heap arrays but already we had done our experiments with no time to remake them. Thus $Nx_{grid} \in [16, 32, 64, 128, 256]$. We choose α to represent very light particles increasing gradually to very heavy ones. $\alpha \in [10^{-9}, 10^{-7}, 10^{-5}, 10^{-3}, 10^{-1}]$. As analytical calculations have nothing to do with grid size then one simulation is done for every set of fixed α and variable Nx_{grid}, while for numerical ones, 5 simulations are done at a fixed α with changing Nx_{grid}. There is no need to perform simulations using the full trajectory code with small mass particles as we already know they will agree very well with the GCA one (see the full comparison in chapter 5), hence we dismiss $\alpha = 10^{-9},\ 10^{-7},\ and\ 10^{-5}$ from full simulations. Table 4.3 and 4.4 summarises the simulations performed for GCA and full trajectory respectively where "N" and "A" denotes numerical and analytical simulations respectively. All particle trajectory experiments presented in both tables have initial positions as follows: $x = z = 0$ and $y = -0.76$ (relatively far from origin). One extra experiment is performed near the origin with all previous parameters the same but fixing $\alpha = 10^{-9}$ and $Nx_{grid} = 256$, and with different initial position such that, $x = 0.1,\ y = -0.1,\ and\ z = 0$, using GCA and full

α \ Nx	16	32	64	128	256	
10^{-9}	N	N	N	N	N	A
10^{-7}	N	N	N	N	N	A
10^{-5}	N	N	N	N	N	A
10^{-3}	N	N	N	N	N	A
10^{-1}	N	N	N	N	N	A

Table 4.3: Performed simulations using the GCA code. Each set of constant α and variable Nx_{grid} correspond for 5 numerical simulations and 1 analytical one.

α \ Nx	16	32	64	128	256	
10^{-3}	N	N	N	N	N	A
10^{-1}	N	N	N	N	N	A

Table 4.4: Performed simulations using the full trajectory code. Low mass particles are dismissed as they give similar results to that simulated with GCA code.

trajectory both with analytical and numerical modules. This extra experiment aims to show how particles are sufficiently accelerated near the origin when they are less magnetised.

4.4 Results

All numerical experiments having any grid size and mass-to-charge ratio coincide with that simulated analytically for the same α value. Figure 4.3 shows one of these experiments with $Nx_{grid} = 256$ and $\alpha = 10^{-9}$. As the particle is so light then it is well-described by guiding centre theory and follows closely the field lines as shown in the first figure. The second one show the motion in the z-direction (out of the plane). For our chosen fields configuration, all drifts are out of plane except $\vec{E} \times \vec{B}$ drift, that is why we can notice a significant motion in this direction.

If we change the grid size, nothing will happen to the whole picture where the particle would also follow nicely the field lines, but entirely the error will change

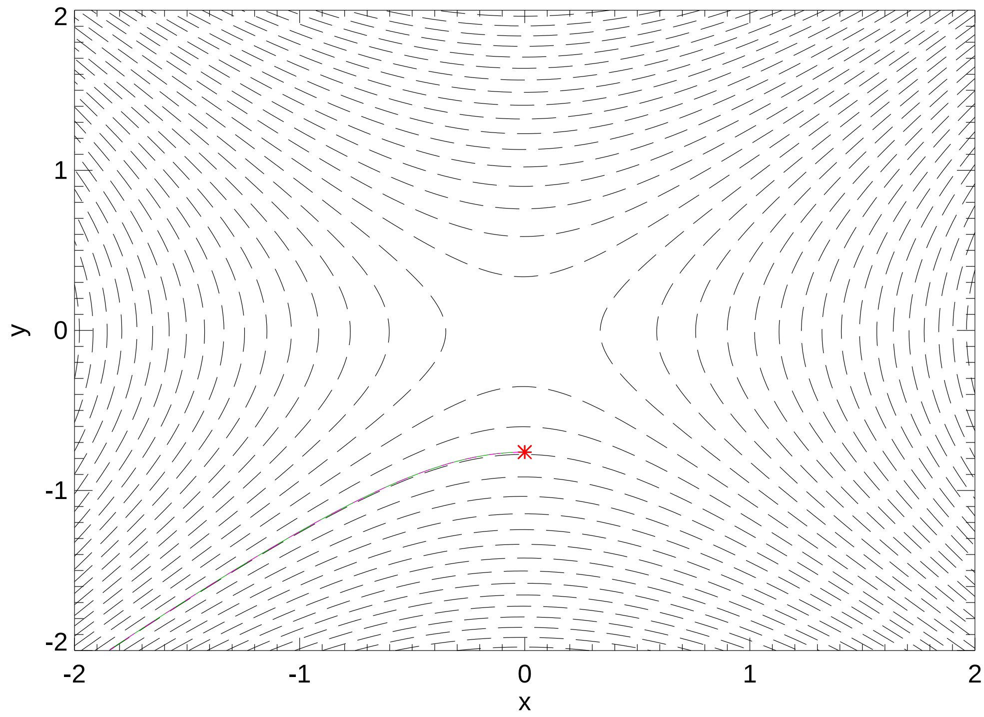

(a) Analytical (solid green) and numerical (dashed pink) particle motion in the sheet plane ($x-y$ plane). The particle follows closely the field lines as it is very light. The asterisk correspond for the initial position.

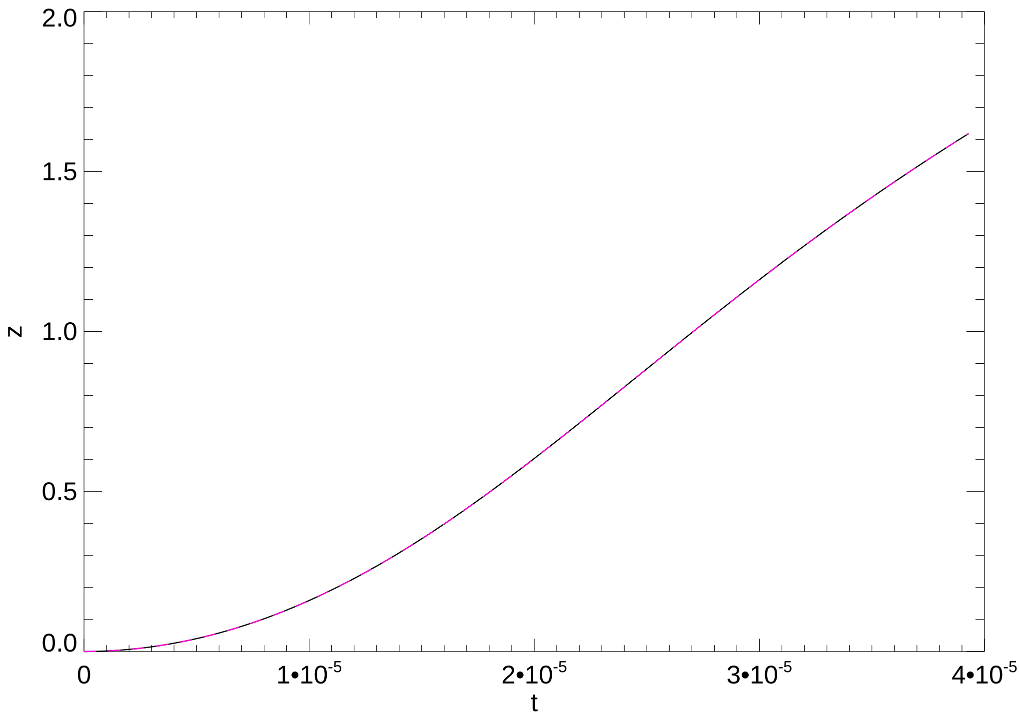

(b) The motion in the z-direction due to the presence of all drifts except $\vec{E} \times \vec{B}$ in this direction.

Figure 4.3: Results for a particle trajectory having $\alpha = 10^{-9}$ on a fine grid of $Nx_{grid} = 256$.

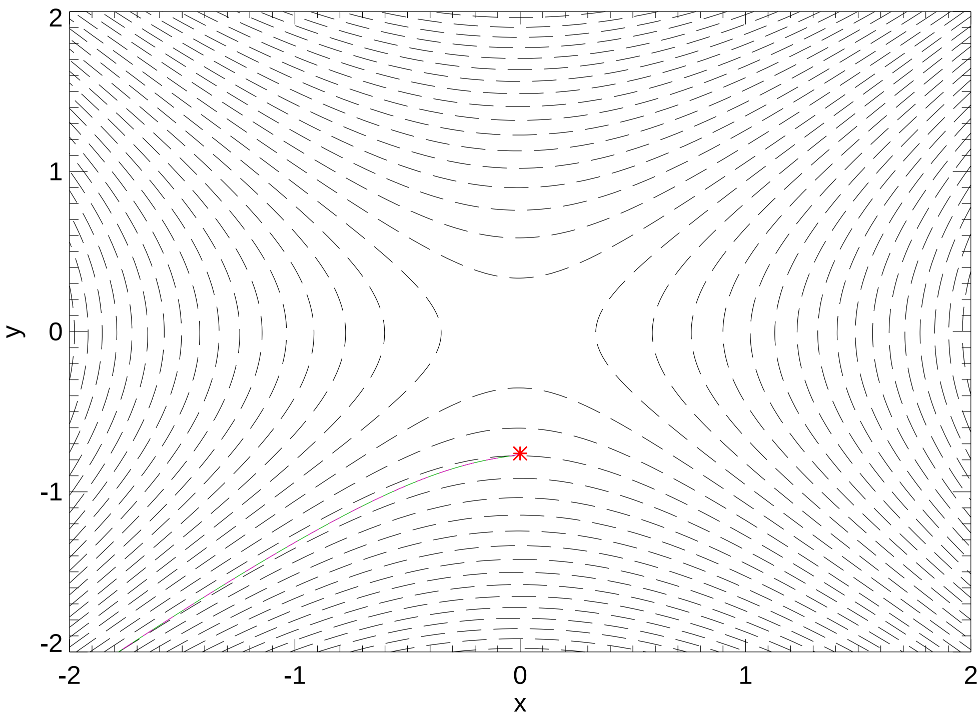

Figure 4.4: Same as figure 4.3 but for a heavier particle with $\alpha = 10^{-3}$. The particle does not perfectly follow the field lines.

as we shall discuss later. The same also if $\alpha = 10^{-7}$ *or* 10^{-5} where those particles remain in the GCA regime. When performing simulations with $\alpha = 10^{-3}$ *and* 10^{-1} the situation differ as now GCA is no more valid (see chapter 5 for more details on non-applicable GCA regime). Figure 4.4 and 4.5 shows particle trajectory using the GCA code for the preceding values of α respectively.

The results of the extra experiment for a light particle, $\alpha = 10^{-9}$, on a fine grid, $Nx_{grid} = 256$ having initial position near the origin ($x = 0.1,\ y = -0.1, and\ z = 0$) are presented in figure 4.6. The upper panel (a and b) show numerical results, while the lower one (c and d) show analytical results for both GCA and full trajectory. Figures (b) and (d) indicate a noticeable acceleration in the z-direction after the particle drifts toward the centre as shown in figures (a) and (c). After passing a long distance in the z-direction, the particle is being ejected from the lower left separatrix.

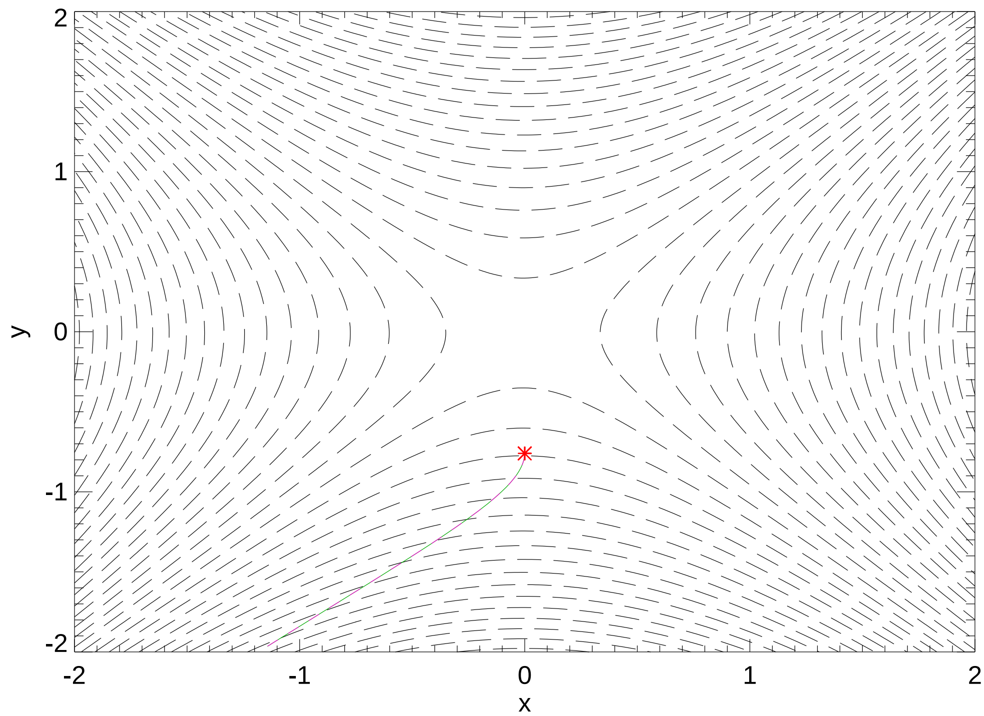

Figure 4.5: Same as before but for a much heavier particle with $\alpha = 10^{-1}$. The particle no more follow the field lines and GCA is broken down (more details in chapter 5).

4.5 Error Discussion

What we mainly care about here is the error analysis and the dependence of the error on the different parameters, in our case Nx_{grid} and α. The error is calculated as the difference between the analytical value and the numerical one, for given Nx_{grid} and α. The final error is given by the following formula:

$$error = \frac{1}{N}\sqrt{\sum_{i=0}^{N}(x_a - x_n)^2 + (y_a - y_n)^2 + (z_a - z_n)^2} \tag{4.8}$$

where subscript "a'' stands for analytical, "n'' for numerical and "i'' for summing over all calculated positions. A similar error can be calculated using velocities rather than positions. Table 4.5 shows the results using the GCA code. Figure 4.7 shows a logarithmic plots for error when fixing α and varying Nx_{grid}. As we expect, error decrease as the grid becomes finer. The plots show a linear relation between $Log(error)$ and $Log(Nx_{grid})$, thus we could conclude that $error \propto Nx_{grid}^{-n}$

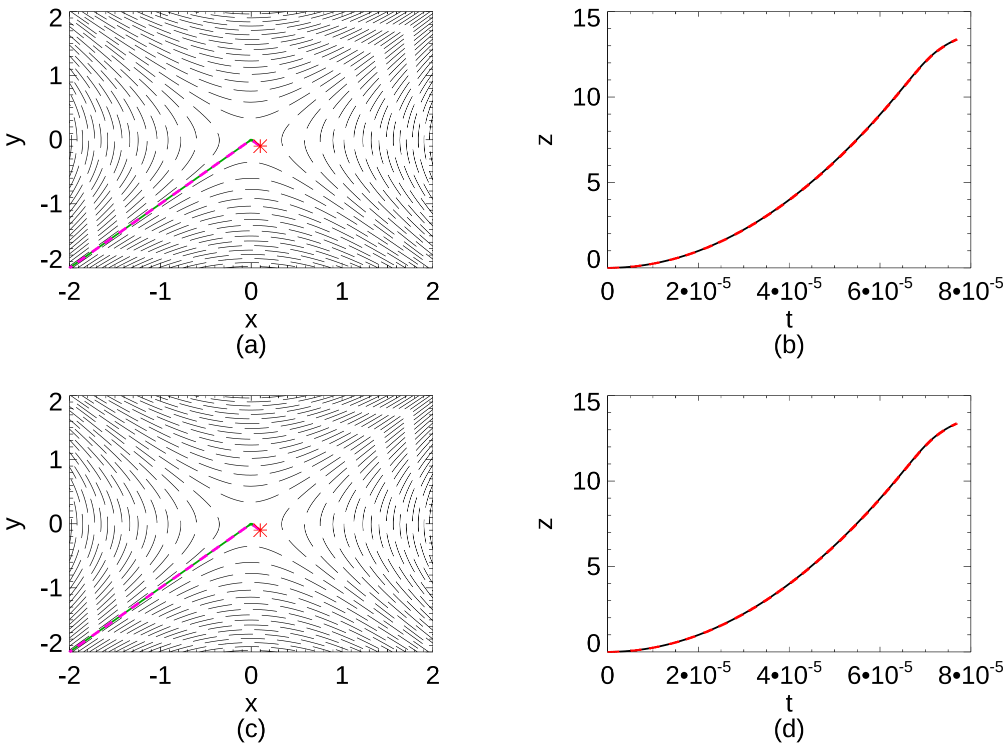

Figure 4.6: a) Numerical GCA (solid green) and numerical full trajectory (dashed pink) trajectory in $x-y$-plane for a light particle having initial position near the origin. b) Trajectory in the z-direction using GCA (solid black) and full trajectory (dashed red). (c) and (d) same as (a) and (b) respectively but for analytical calculation without interpolation from the discrete grid. The particle is sufficiently accelerated in the z-direction in a small time before being ejected from one of the separatrices.

α \ Nx	16	32	64	128	256
10^{-9}	$1.094925.10^{-4}$	$2.992065.10^{-5}$	$7.822563.10^{-6}$	$2.009044.10^{-6}$	$5.304022.10^{-7}$
10^{-7}	$3.448845.10^{-5}$	$9.424147.10^{-6}$	$2.463145.10^{-6}$	$6.325505.10^{-7}$	$1.669911.10^{-7}$
10^{-5}	$1.838233.10^{-5}$	$5.110984.10^{-6}$	$1.277694.10^{-6}$	$3.319355.10^{-7}$	$9.364546.10^{-8}$
10^{-3}	$2.269898.10^{-5}$	$6.723262.10^{-6}$	$1.875811.10^{-6}$	$5.024031.10^{-7}$	$1.449038.10^{-7}$
10^{-1}	$1.274749.10^{-3}$	$3.824872.10^{-4}$	$1.029695.10^{-4}$	$2.646001.10^{-5}$	$6.676308.10^{-6}$

Table 4.5: Error calculation using equation 4.8 for each experiment. Other forms of error expression could be used but all of them would give in general similar results.

where n is the slope of the parallel lines. A simple calculation for the slope yields that $n = 1.92$. This value is fully justified by our used linear interpolation method; following from Taylor expansion for linear interpolation, the error should be of second order, $O(Nx_{grid}^2)$, which our results indicate. If we were to choose a critical or minimum value for Nx_{grid} in a basis that the minimum error using any mass-to-charge ratio would be acceptable (e.g. 10^{-4} *or* 10^{-5} and smaller) then we would say

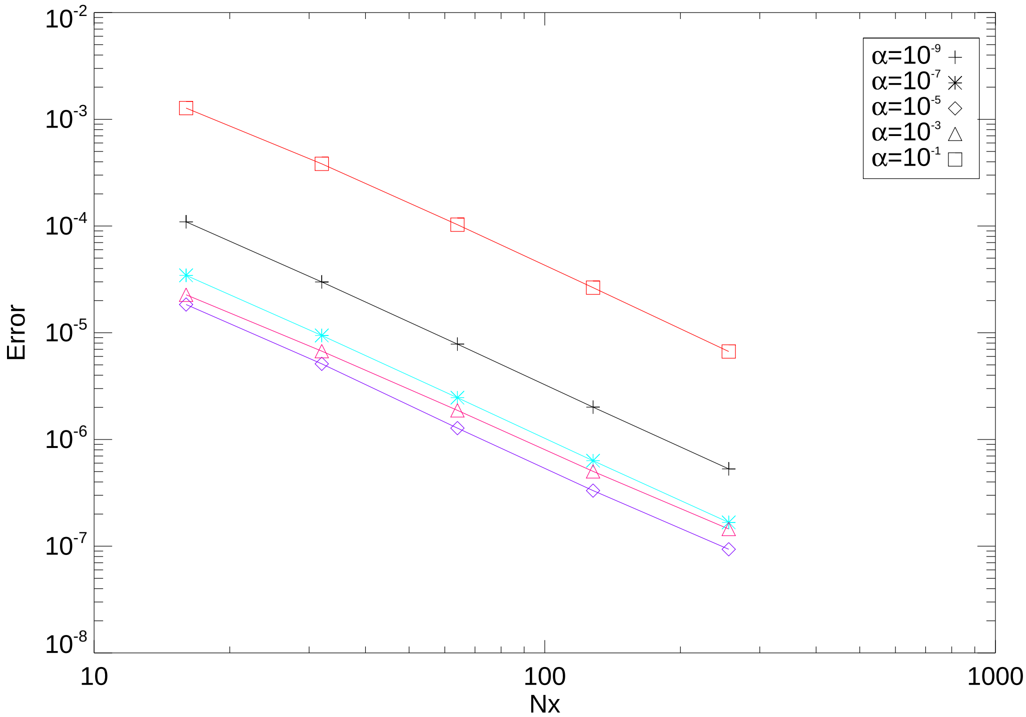

Figure 4.7: A logarithmic plot for $error$ vs. Nx_{grid} for the 5 α values. $Log(erorr)$ decreases lineally in the plots with a slope of ~ 2 indicating that $error \propto Nx_{grid}^{-2}$.

that $Nx_{grid} = 128$ is a good choice.

Now we consider the effect of fixing Nx_{grid} and varying α, which is an interesting case as we do not have any predictions for it. Figure 4.8 shows these plots. All five curves show similar orientation, so a general conclusion can be drawn. The error decreases as α decreases till the mass-to-charge ratio reaches 10^{-5} where it then turns up and begin increasing. What we know about this point is that it is a turning point between applicable and non-applicable GCA regime, so we can say that when GCA is applicable, the error decreases slowly with decreasing α, whereas when GCA is not applicable the error increases rapidly with increasing α.

On the other hand, the full trajectory data will not hold any surprising results. As we said before, small particles will obey the rules of the guiding centre theory that is why we perform simulations using the full trajectory code with heavy particles. The first thing to do is comparing the 2 results just by plotting both trajectories on the same graph. Figures 4.9 and 4.10 shows these plots for $\alpha = 10^{-3}$ and 10^{-1} respectively. It is obvious that the 2 trajectories do not coincide and the case

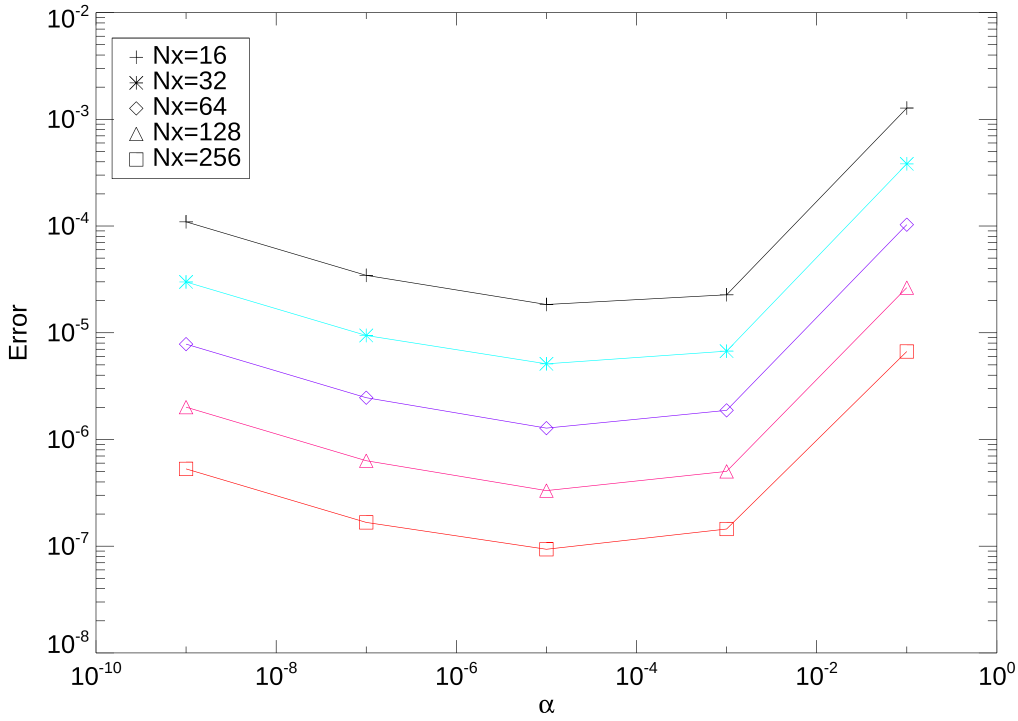

Figure 4.8: $Error$ vs. α for the 5 Nx_{grid} values. It is the inverse plot for the previous one. All lines show same feature for $Log(error)$ decreasing slowly with increasing α till reaching the non-applicable GCA regime where the $error$ orientation reverses and increase rapidly. Basically the GCA should not be used at this stage as its non-applicable so even the error discussion would not be informative.

become worse when α become larger. We also calculate the error in the numerically-calculated kinetic energy at the final step. This is relevant because main use of trajectory calculations in solar flare modellings is to evaluate energy gain of particles. We are interested in comparing full trajectory with GCA so we will not compare analytical data with numerical one within the full trajectory calculations. We would rather compare analytical with analytical and numerical with numerical between full trajectory and GCA. The non-relativistic equation of kinetic energy is:

$$E_K = \frac{1}{2}mv^2 \tag{4.9}$$

dropping the first 2 terms as they are constants then v^2 is taken into account. Table 4.6 illustrate the values of v^2 for different parameters for both full trajectory and GCA at the final step. In table 4.7 we calculate the error at certain Nx_{grid} and α, analytical with analytical and numerical with numerical between full trajectory and

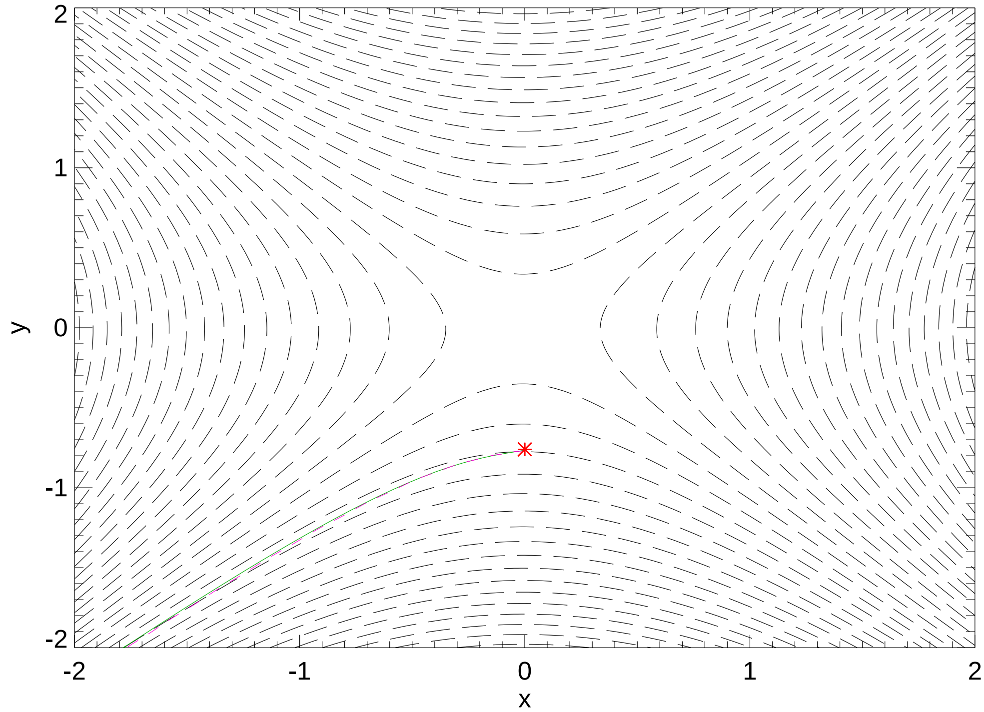

Figure 4.9: GCA (solid green) and full trajectory (dashed pink) trajectories for a particle with $\alpha = 10^{-3}$. The 2 lines do not coincide exactly as the particle can be considered as a heavy one and does not obey guiding centre validity conditions.

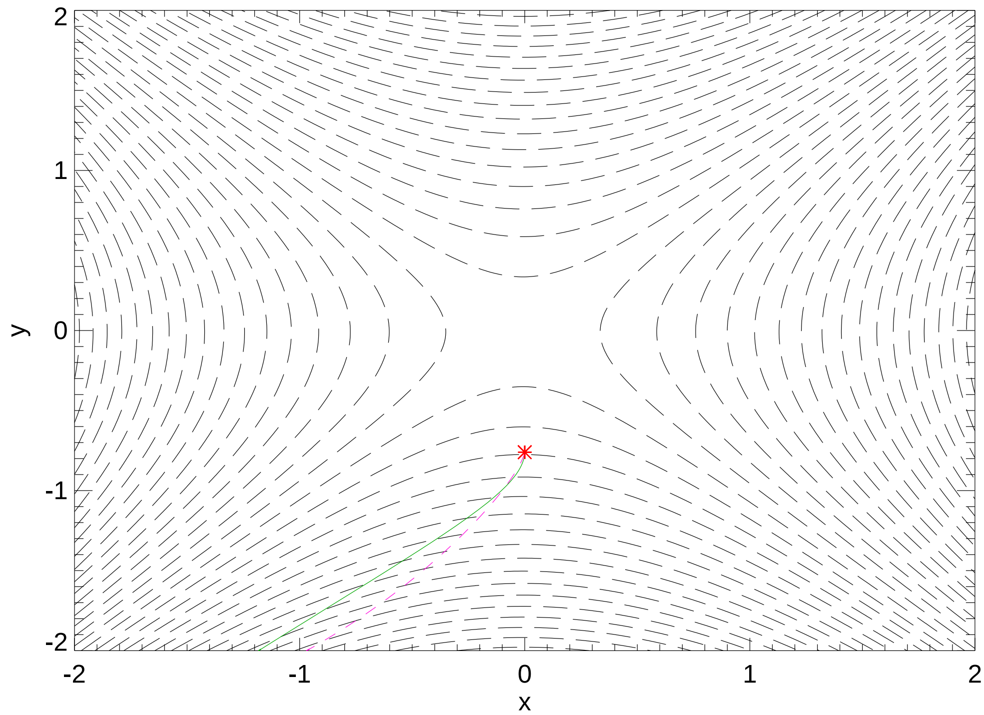

Figure 4.10: Same as figure 4.9 but for a heavier particle ($\alpha = 10^{-1}$). The 2 trajectories show different paths.

GCA.

	α \ Nx_{grid}	10^{-3}	10^{-1}
Full	16	$1.582015.10^4$	$1.414568.10^2$
	32	$1.582866.10^4$	$1.415142.10^2$
	64	$1.583060.10^4$	$1.415358.10^2$
	128	$1.583135.10^4$	$1.415429.10^2$
	256	$1.583119.10^4$	$1.415435.10^2$
	Analytical	$1.583130.10^4$	$1.415459.10^2$
GCA	16	$1.587208.10^4$	$1.342827.10^2$
	32	$1.588349.10^4$	$1.343811.10^2$
	64	$1.588591.10^4$	$1.343905.10^2$
	128	$1.588662.10^4$	$1.343963.10^2$
	256	$1.588653.10^4$	$1.343955.10^2$
	Analytical	$1.588660.10^4$	$1.343980.10^2$

Table 4.6: The value of the kinetic energy at the final step for the simulated particle using full trajectory and GCA with all grid sizes and just for heavy particles in order to calculate the error.

α \ Nx_{grid}	16	32	64	128	256	Analytical
10^{-3}	0.328	0.346	0.349	0.349	0.349	0.348
10^{-1}	5.07	5.04	5.05	5.05	5.05	5.05

Table 4.7: The calculated error in final energy between full trajectory and GCA (analytical with analytical and numerical with numerical) at each grid size for particles with $\alpha = 10^{-3},\ 10^{-1}$.

As the value of the error hardly varies with using coarse or fine grid, then we could say that the choice of grid size will not influence the error between full trajectory and GCA at this certain grid size. Of course, using a finer grid reduces the error when comparing analytical and numerical solutions.

Chapter 5

Trajectory Calculations For Numerical Fields

In this chapter we are going to make further comparisons between full trajectory and GCA. Now simulations will be held using real data from MHD simulations. We expect that full trajectory will give similar results when the Larmor radius is much smaller than the length scale of the system, but we need to determine how small the Larmor radius needs actually to be. Also, we will perform simulations at different positions within the current sheet (near and far from the origin and at magnetic islands). Besides, we will consider conditions that violate the requirements of the guiding centre theory, and see how the particle behaves non-adiabatically.

5.1 System Formalism

The formalism will not change in this chapter and all characteristic values used before will remain unchanged. The only difference is the domain of definition of the y-axis where $y \in$ [-1.0 , 1.0] because the MHD data delivered to us is defined over this domain where $Nx_{grid} = 256$ and $Ny_{grid} = 128$. This data correspond to one snapshot of the forced reconnection described in section 2.3.4 for the phase in which a current sheet and X-point are formed. This stage is the most important stage through the reconnection procedure, as the current is concentrated at the

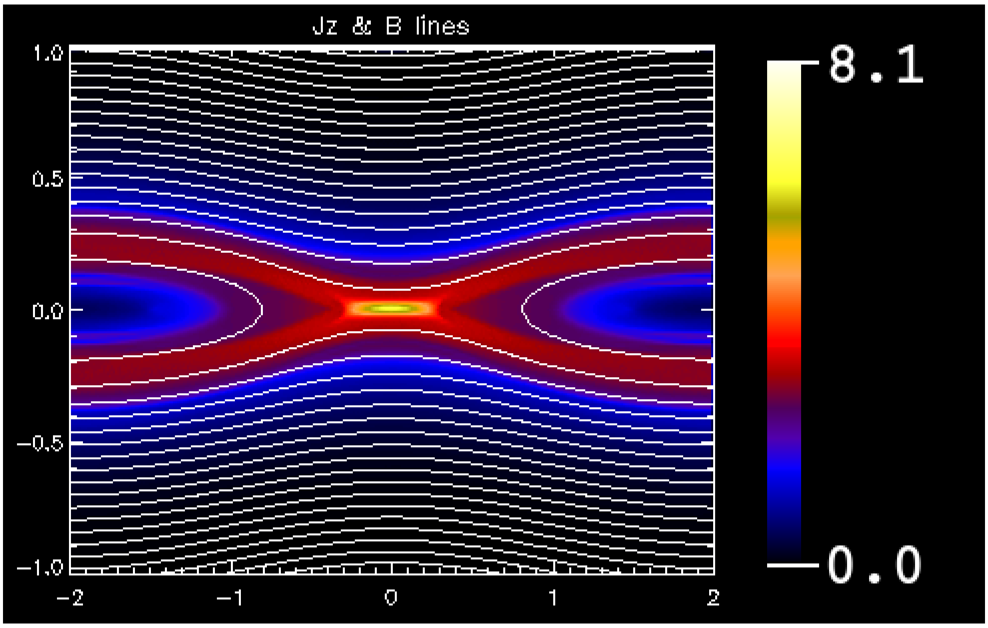

Figure 5.1: Magnetic field lines in the current sheet plane ($x - y$ plane) with a colour scale for the current density. Data taken from Gordovskyy et al. (2010b). The current sheet is symmetric vertically and horizontally but in opposite polarity for field lines. In the bottom section the field lines are directed from the right to the left where in the top section it is reversed. The current density $\vec{j}$ is concentrated at the centre of the sheet and decreases gradually as going away.

centre and along 2 separatrices making an X-shape where particles are sufficiently accelerated. Figure 5.1 shows a plot for the field lines with a colour scale for the current density.

5.2 MHD Data Analysis

Before going through the experiments for particle trajectory, we shall first analyse some parameters for the MHD data given, in order to understand what type of particle motions we expect at different positions in the domain. Figures 5.2, 5.3, and 5.4 are contour coloured plots of the 3 components of the magnetic field, $B_x,\ B_y,\ and\ B_z$ respectively. B_x and B_y are both zero near the X-point. They increase in magnitude as we go away from the reconnection site (B_x has a *tanh* shape if we fix x and plot y as it is defined initially shown in Figure 5.5 similar to that shown in Figure 2.19). The guiding field B_z has a high value near and at the X-point. We could notice also that its highest value is at the 2 magnetic islands and

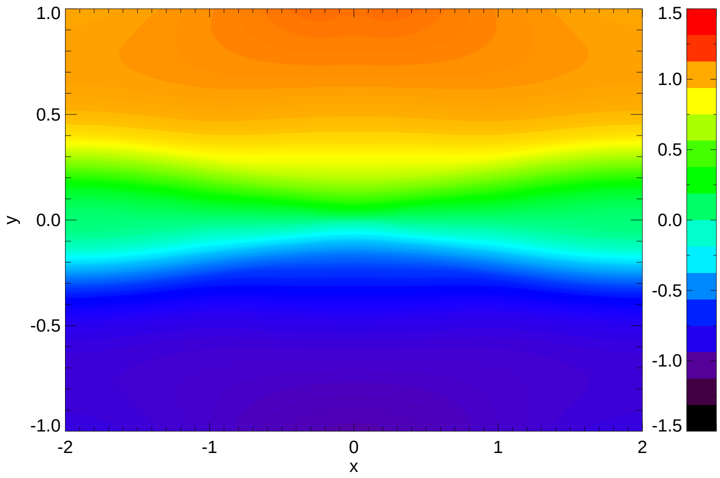

Figure 5.2: Coloured contour plot for $\vec{B}_x$ over the defined domain.

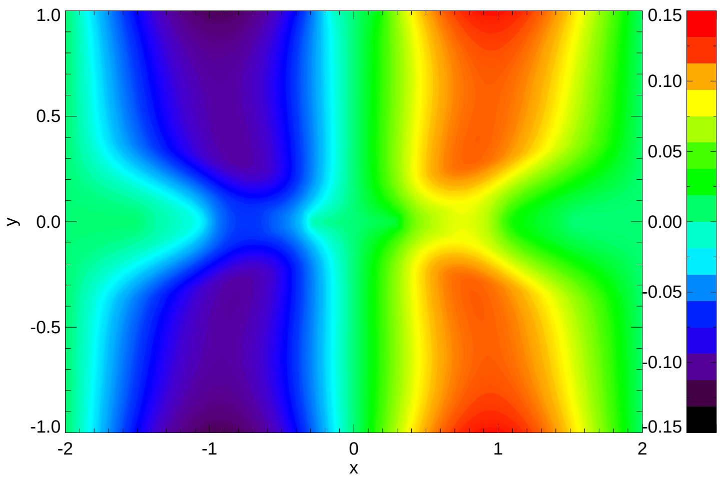

Figure 5.3: Coloured contour plot for $\vec{B}_y$ over the defined domain.

that its magnitude decrease as we go further from the centre. Figure 5.6 shows the absolute value of the magnetic field in the grid i.e. $|\vec{B}| = \sqrt{B_x^2 + B_y^2 + B_z^2}$. As we expect, $|\vec{B}|$ has its lowest values near the centre of the domain where reconnection occur as particles become un-magnetised there and ready to be accelerated by the electric field.

The z-component of the magnetic potential associated with the magnetic field is evaluated by numerically integrating over B_x and B_y using a specific code and used as a background. Figure 5.7 shows a contour plot for A_z corresponding to the magnetic field lines in the $x - y$ plane (a surface plot is provided in Figure 5.8). Figure 5.9 shows a contour coloured plot for the absolute value of $\vec{E}$ i.e. $|\vec{E}| = \sqrt{E_x^2 + E_y^2 + E_z^2}$.

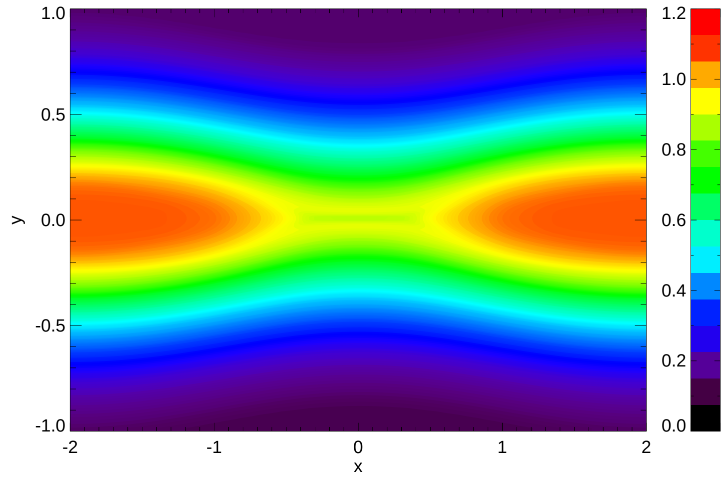

Figure 5.4: Coloured contour plot for $\vec{B}_z$ over the defined domain.

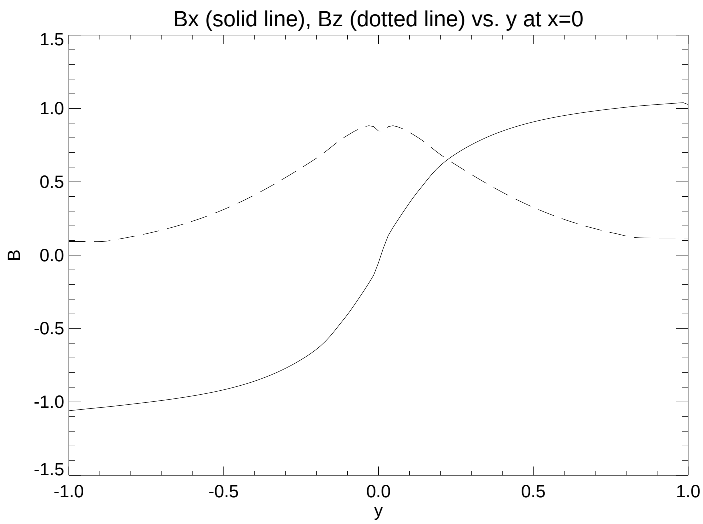

Figure 5.5: B_x (solid line) and B_z (dashed line) vs. y at the vertical centre of the sheet ($x = 0$). These are quite similar to initial profiles as shown in figure 2.19 after long time of evolution.

As we expect also, E is zero far from the centre where no current exist and particles are strongly magnetised. This value increases dramatically near the reconnection site making 2 peaks around the centre and its nearly zero at $x = y = 0$. The final plot in figure 5.10 represent the dot product between $\vec{E}$ *and* $\vec{B}$ divided by $|\vec{B}|$ ($\vec{E}.\vec{B}/|\vec{B}|$) which represent the parallel component of the electric field responsible for the direct acceleration along longitudinal field lines. This component is mainly significant near and at the X-point, and along the X-shaped separatrices due to the anomalous resistivity which operate at these regions. We expect that this component

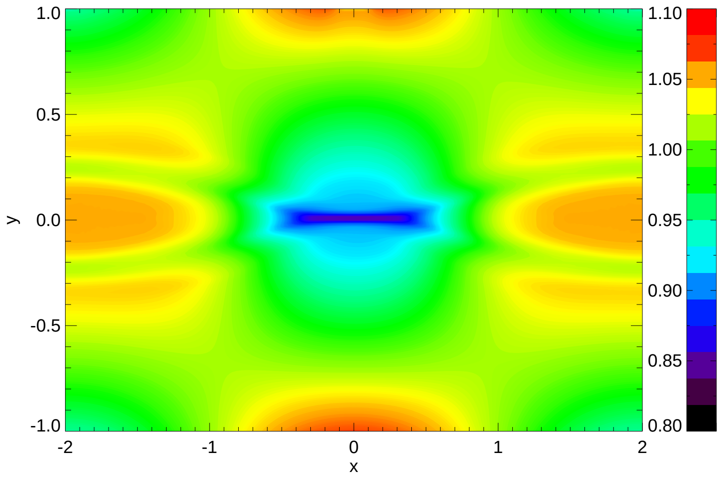

Figure 5.6: The absolute value of the magnetic field ($|\vec{B}|$) over the defined domain.

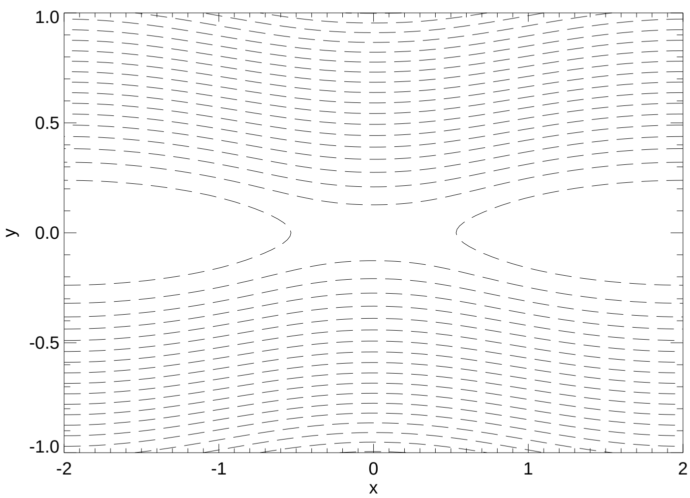

Figure 5.7: A contour plot for the z-component of the magnetic potential A_z representing the field lines in the simulated current sheet in the $x - y$ plane reproduced after integrating the magnetic potential equation. Same as Figure 5.1 but without the current density.

will influence on the energy gain of the particle at these locations as we shall see when we plot each component of motion from the GCA separately in coming plots.

5.3 Particle Trajectory Experiments

In all what follows, unless otherwise stated, the value of mass-to-charge ratio is, $\alpha = 4.4 \times 10^{-4}$, which is an Helium-3 ion (^3He), not chosen for any physical reason.

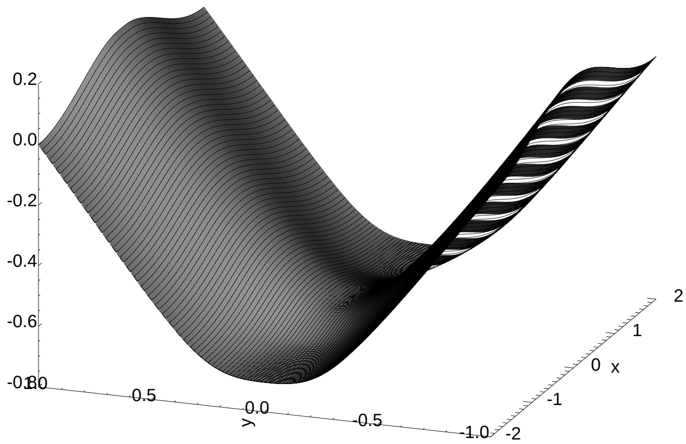

Figure 5.8: Surface plot of the current sheet.

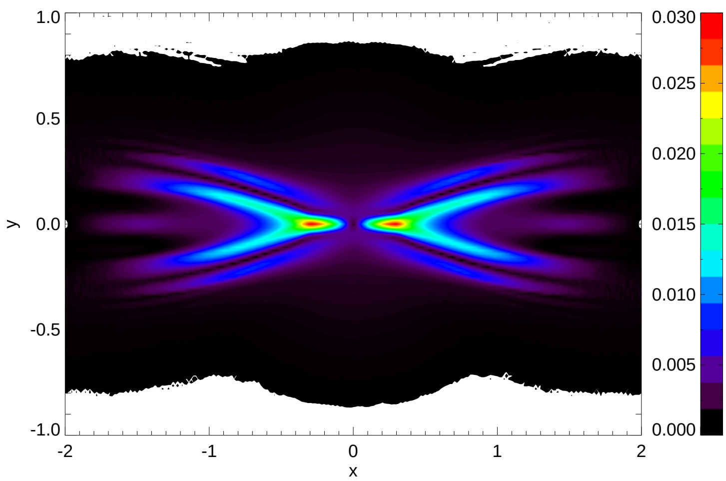

Figure 5.9: Absolute value of the electric field ($|\vec{E}|$) over the defined domain.

5.3.1 Matching Experiments

In this first section of experiments, we will present the work when the guiding centre can be applied where both GCA and full trajectory codes give similar results. The guiding centre theory is expected to be applicable since $r_l/L_{\nabla B}$ shows a value around 10^{-5} throughout all the following experiments (the value of $L_{\nabla B} = |\vec{B}|/|\nabla\vec{B}|$ was calculated by interpolating x, y, and z components of $\nabla\vec{B}$ within the interpolation function as the MHD data contain this information). We performed numerous simulations, and present some typical examples here. We divide the experiments into 2 sets, low magnetic moment, μ, where $V_\parallel$ dominates over $V_\perp$ initially by choosing

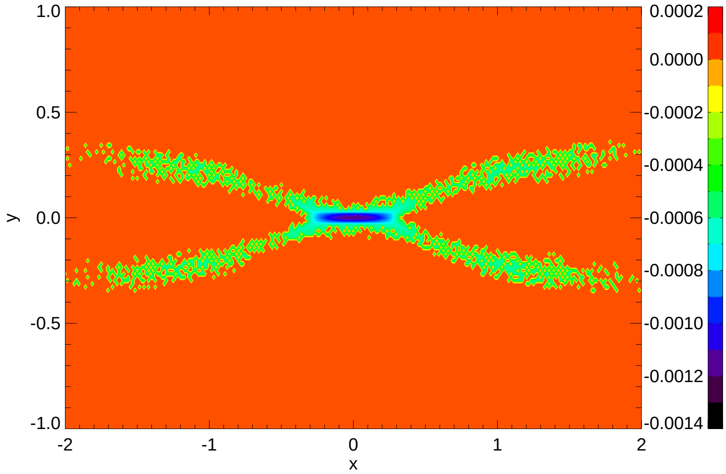

Figure 5.10: Parallel electric field, zero everywhere except at the separatrices.

$cos(\theta)$ near to one (in our case we take it to be 0.8), and the opposite case, high μ, with $cos(\theta) = 0.1$. Mainly the noticeable difference between high-μ particles and low-μ one is that the former undergo some mirroring. We begin first with the low μ case and show results for 9 particles simulated both by GCA and full trajectory with $V_{ini} = 0.1V_A \; and \; cos(\theta) = 0.8$ with different initial positions as shown in figures 5.11 and 5.12. The same initial phase-space components are entered to both codes in each experiment. We can see that both codes in this set give similar results and particles follow nicely the field lines. Magnetic field and due to reconnection is divided into two regions, open and closed field lines near upper and lower boundaries and at magnetic islands in the outflow region respectively. This gives rise to particles being distributed into two distinct categories; particles moving in an open magnetic field travel long distances in the x-direction and oscillate in the y-direction (all experiments in figure 5.11 and 3 experiments in figure 5.12), while those moving in a closed field lines are trapped in the magnetic islands (one experiment in figure 5.12). All these experiments have initial positions relatively far from the origin. Figure 5.13 shows one extra experiment in this set for a particle initially at the origin, $(x = y = z = 0)$, being accelerated in the negative z-direction. After being sufficiently accelerated out of the plane, the particle is ejected from the lower right separatrix.

Figure 5.14 show results for 3 experiments for the other set of simulations (high

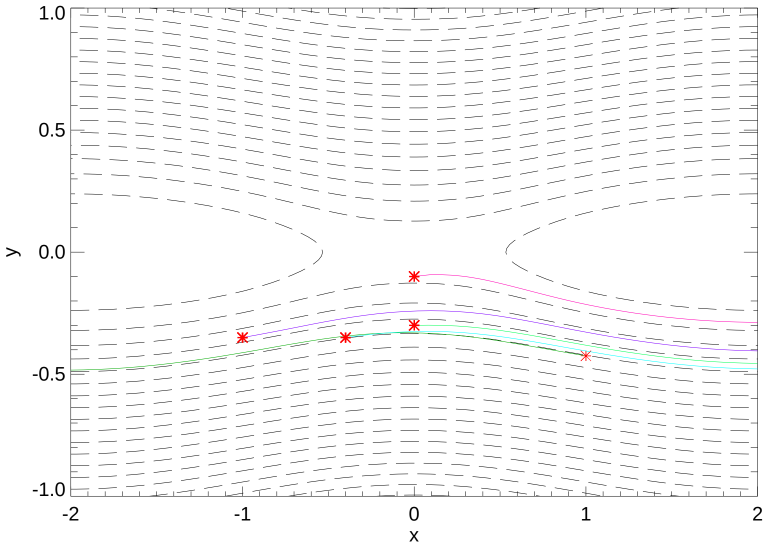

(a) 5 experiments in the set of low μ done using the GCA code. The asterisk marks the initial position.

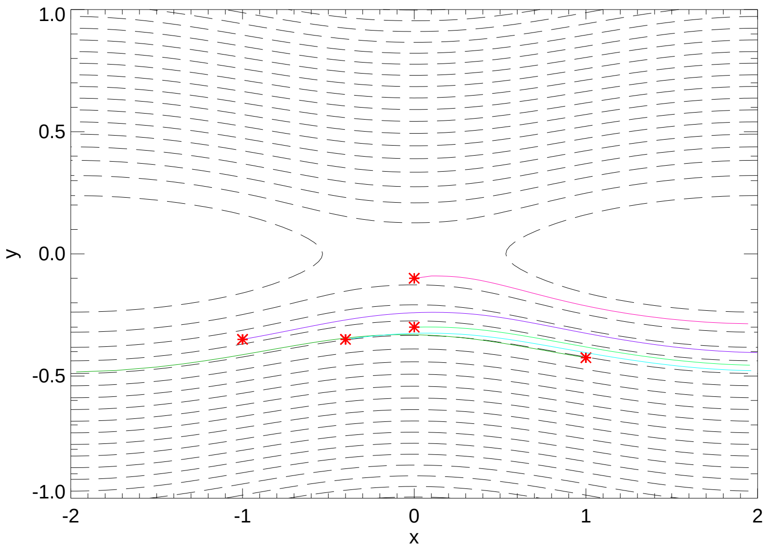

(b) The same 5 experiments simulated using the full trajectory code.

Figure 5.11

μ) with $V_{ini} = 0.1V_A\ and\ cos(\theta) = 0.1$ using GCA and full trajectory. It is probably the same or slightly different with high μ as particles will remain following the field lines but we can notice some slightly crossing over the lines.

5.3.2 Non-Matching Experiments

While performing some experiments, we notice that some of them do not match (GCA and full trajectory). The high μ case makes very weird motions completely

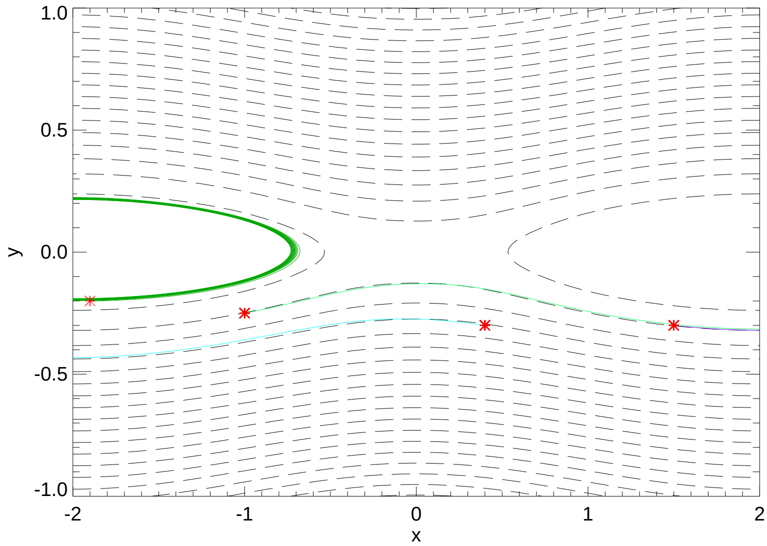

(a) 4 extra experiments in the set of low μ done using GCA code.

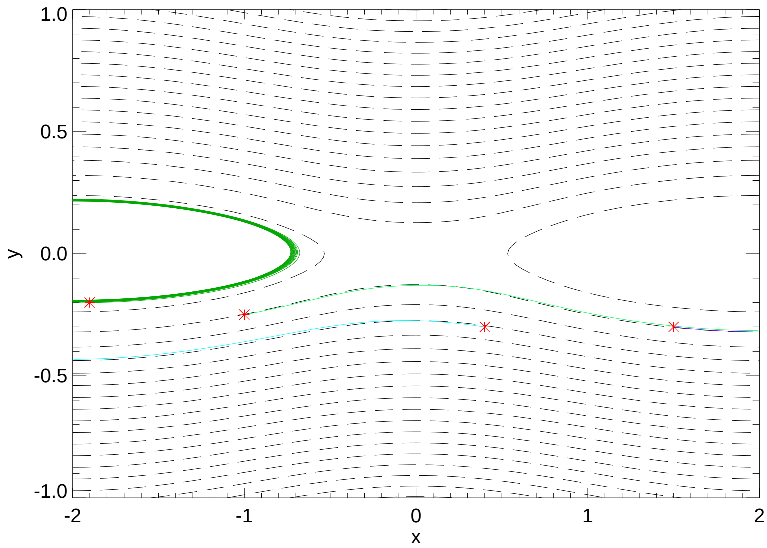

(b) The same experiments using the full trajectory code.

Figure 5.12: At magnetic islands, the condition of particle passing the defined domain stops the simulation is dismissed, that is why the particle keep bouncing in the left current island.

different from that of GCA and what we expect. Figure 5.15 shows one of these faulty experiments for the low μ case. Here the problem is that the full trajectory particle experiences one extra bouncing motion than the GCA, but the motion in general is the same. The problem seems to be in the full trajectory code and not in the GCA code as there is no reason for such a bounce at the specific location where the bounce occur. As we discussed earlier in § 2.2.2 about magnetic mirroring that this happens when a particle is drifting from a weaker to a stronger magnetic region,

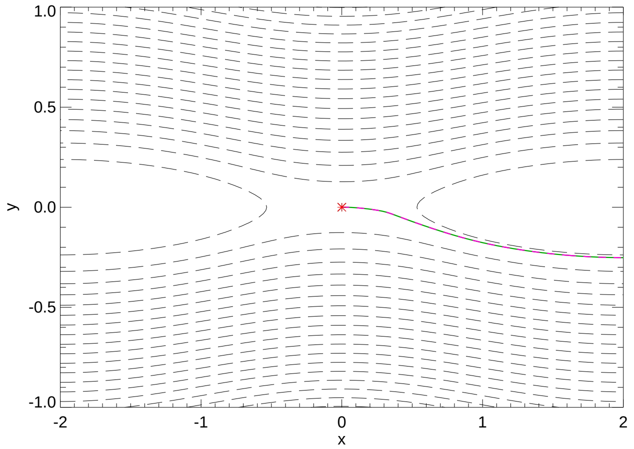

(a) Full trajectory (solid green) and GCA (dashed pink) particle trajectory in the current sheet.

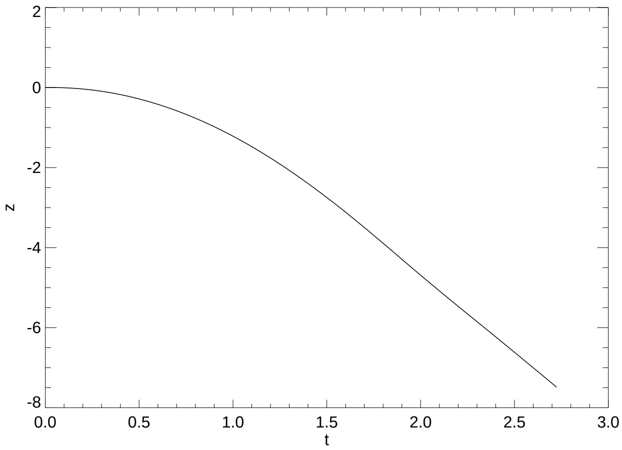

(b) Trajectory along the z-direction from the Full simulation.

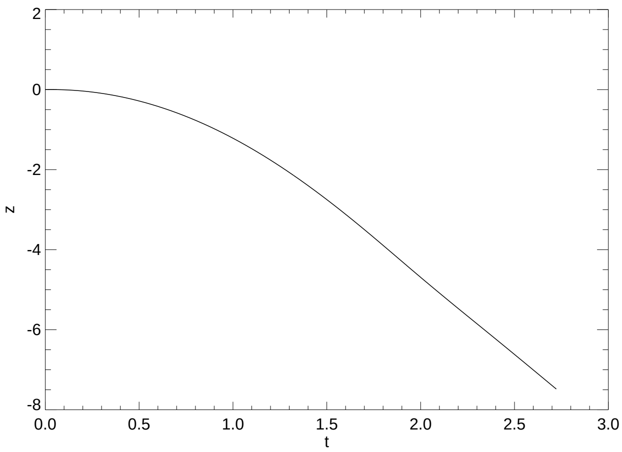

(c) Trajectory along the z-direction from the GCA simulation.

Figure 5.13: Particle being accelerated in the negative z-direction as being placed initially at the origin of the current sheet where it is less magnetised. After acceleration, the particle is ejected from one of the separatrices. We could not plot the z-component of motion from GCA and full trajectory on the same graph as for time step differences but it is noticeable that both curves coincide.

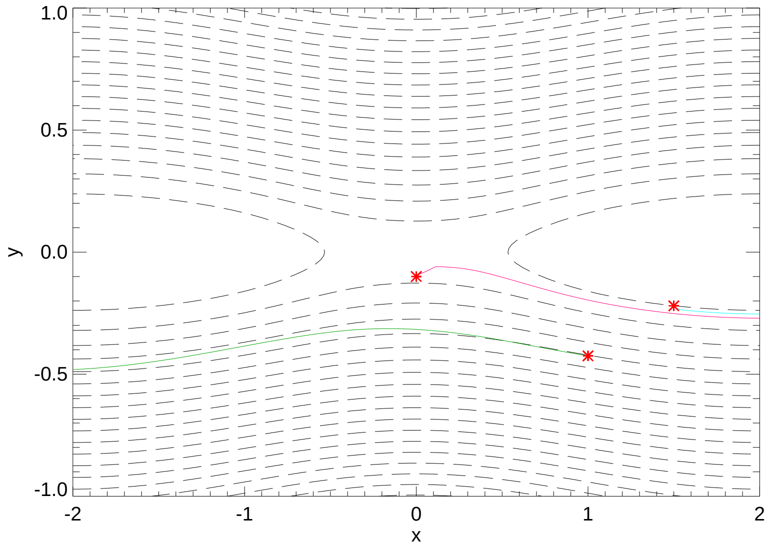

(a) 3 experiments in the set of high μ done using the GCA code.

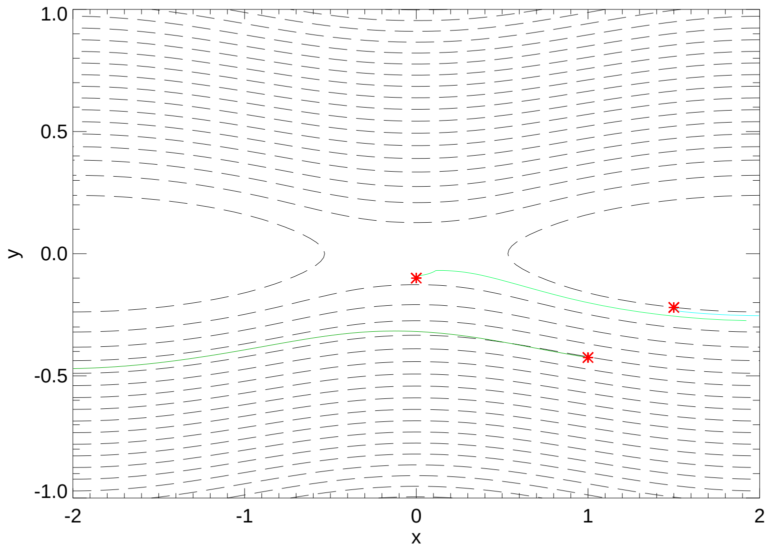

(b) The same experiments simulated using the full trajectory code.

Figure 5.14

which is not the case at the specific location of the extra bounce in figure 5.15b. Figure 5.16 shows the same problem but for the high μ case; things become worse, as the particle motion is completely different and messy. Again it is obvious that the full code show the wrong trajectory as it is unlikely for an adiabatic particle to behave as the particle in figure 5.16b do. Every thing seems to be fine within the code as we review it several times especially that it passes the testing procedure without any fatal mistakes, so what is going on!!??

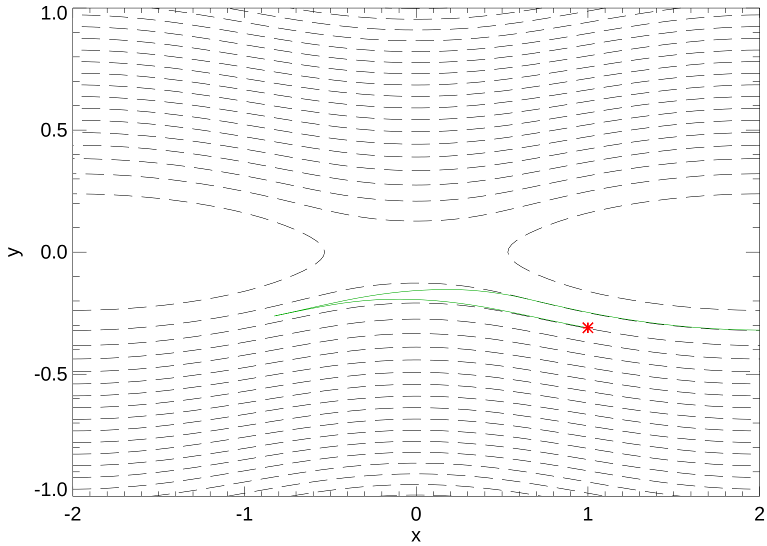

(a) The particle simulated using the GCA code. The trajectory shown is the normal one.

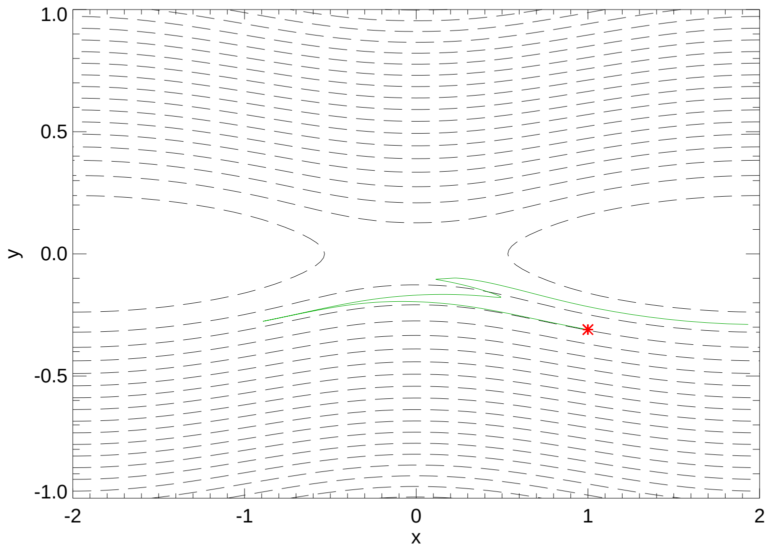

(b) The same experiment using the full code. The trajectory show extra bouncing which was not understood.

Figure 5.15: One of the fault experiments with low μ value.

5.3.3 Numerical Issue, Problem Solved

When we were trying to understand the reasons behind the anomalous experiments, we discovered something interesting and surprising in the code. First, we guessed that such unusual motions like extra bouncing could happen when the parallel electric field is so high but we could not find any explanation for it. In fact any term could cause such an effect but the parallel electric field is mainly zero everywhere

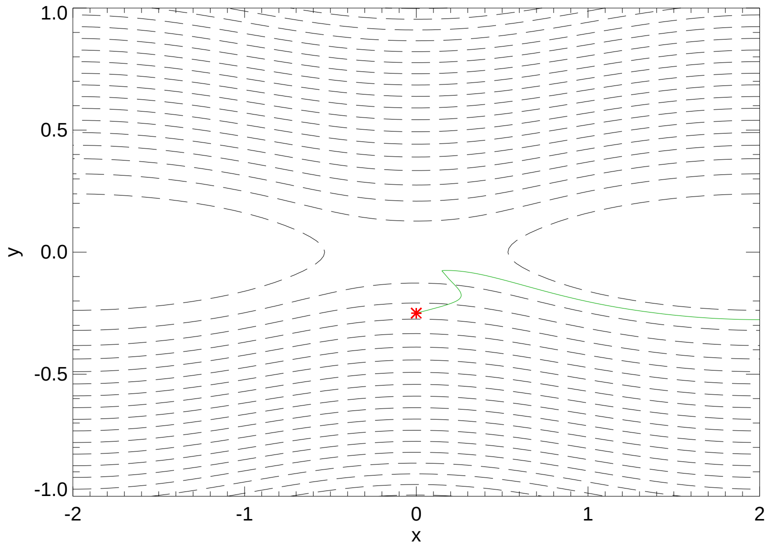

(a) The normal trajectory using GCA.

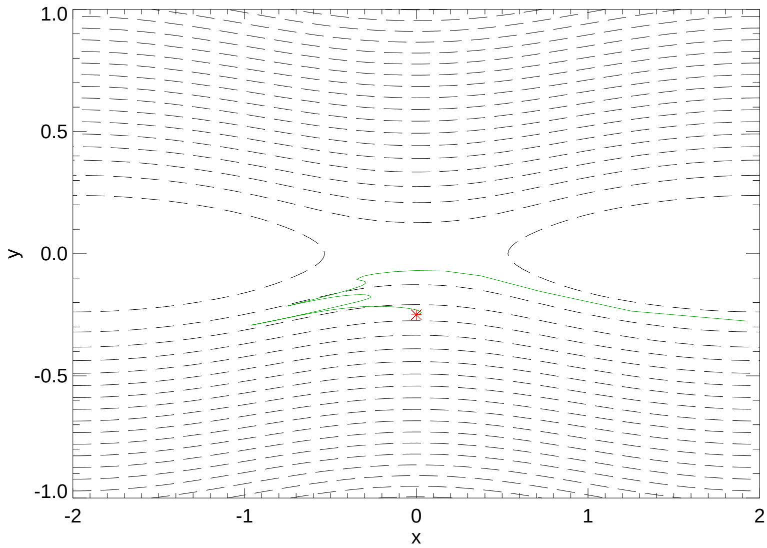

(b) Same experiment using the full code. The trajectory looks very messy raising a fundamental problem.

Figure 5.16: Another fault experiment but with high μ value.

except near the diffusion region where it has small values, whereas $E_\perp$ always has relatively higher values, thus any small numerical error in calculating $E_\parallel$ may cause artificial effects; that is why we suspect it to cause the problem. In attempt to solve the problem we get the minimum and maximum values for the parallel electric field defined on the initial mesh given from the MHD data. We find that, $min(\vec{E_\parallel}) = -0.0012489010$ and $max(\vec{E_\parallel}) = 7.3752310 \times 10^{-8}$ in dimensionless units. We analyse in detail the results of the experiment shown in figure 5.15, and tried to understand what happens when the particle bounces backward and forward where it should (according to GCA) continue its path without any bouncing. When we output the value of the parallel electric field near the first bounce it was above 10^{-6} which itself is greater by 100 times than the maximum value of the parallel electric field defined on the grid without interpolating, thus an error may have happened during interpolation. We choose an arbitrary point to check what is happening within the interpolation, and we make the calculations by hand using 2 approaches. First after getting the 6 fields at the 4 grid points around the particle position, we calculate the parallel component of the electric field at the 4 corners all having values around 10^{-9} and then when interpolating these 4 values to get the interpolated parallel electric field, we get an acceptable value in the same range of the 4 values (figure 5.17a). The second approach, which our code uses, is calculating the interpolated values of the 6 fields at the particle position and then calculates the value of the parallel electric field (figure 5.17b) which will not necessarily be the same value as before but should be very close. Surprisingly the value was 1000 times greater in the range of 10^{-6} in consistent with the values we noticed at the bounce. So in fact this gives rise to a numerical error that should be solved to get accurate values at all positions. In fact we could explain what happened as a leakage from the perpendicular component of the electric field to the parallel one at places where the electric field is approximately perpendicular to the magnetic field where parallel electric field is ~ 0. Such an error could cause a severe change in the angle between electric and magnetic fields causing a sudden change on the particle motion showing a bounce feature. In attempt to solve this problem we create a corrector electric field having the following formula:

$$\vec{E}_{corr} = \vec{E} - (\vec{E}.\vec{b}).\vec{b} + |\vec{E}_{\parallel}|.\vec{b} \tag{5.1}$$

where $\vec{E}$ are the three interpolated values of the electric field at the 4 corners (giving these fault results) and $\vec{b}$ is the magnetic unit vector after interpolating the 4 values for each of the 3 components of the magnetic field, and $|\vec{E}_{\parallel}|$ is the scalar of the interpolation of the parallel electric field at the 4 corners (giving the acceptable results). In this way we guarantee that the parallel electric field is correct and dismiss its fault values from the interpolated $\vec{E}$ field. Now after applying changes to the interpolation function within our code we re-perform all our previous experiments. All matching experiments re-match and the non-matching one now show similar results. Figures 5.18 and 5.19 show the new results for the non-matching experiments shown previously in figures 5.15 and 5.16.

5.3.4 GCA Data Analysis

In order to get a better understanding for the results especially that done using GCA code we plot each component of motion separately. The GCA code solves equations in Appendix A.2 where we can plot each term accounting to the motion separately like the $\vec{E} \times \vec{B}$, curvature drift, grad drift, mirroring, acceleration due to parallel electric and some others. In full trajectory, the code solves equations 3.3 where all aspects of motion are hidden entirely and add up to form the particle trajectory. We should note that the GCA version delivered to us is a "light" one i.e. the higher terms of GCA expressions (last 4 terms of equation A.12) were turned off as they do not have any noticeable difference. These terms would be important if $U_{\vec{E}\times\vec{B}}$ has a comparable value with the local Alfven velocity, but this is not always the case as at maximum $U_{\vec{E}\times\vec{B}} \sim 10^{-2}V_A$. The $\vec{E} \times \vec{B}$ and the $\vec{E}.\vec{b}$ terms represent the bulk plasma (in our case, "particle") motion ($\vec{E}.\vec{b}$ term tends to zero far from the centre of the sheet as shown in figure 5.10 and as we shell show now). Other terms become important at specific locations, for instance curvature drift becomes important when field lines are curved enough as discussed in § 2.2.2.

We will take some experiments and analyse them in more depth. In each figure we will present 8 plots; the 1st (upper-left panel) shows how the particle moves in the domain (same as shown in previous plots), the 2nd (upper-centre panel) shows $U_{\vec{E}\times\vec{B}}$, the velocity due to $\vec{E} \times \vec{B}$ drift versus x, the 3rd (upper-right) shows $U_{\vec{E}\times\vec{B}}$ versus y (not that informative as particles are mainly moving in the x-direction) , the 4th (middle-left panel) shows the curvature drift component vs. x, the 5th

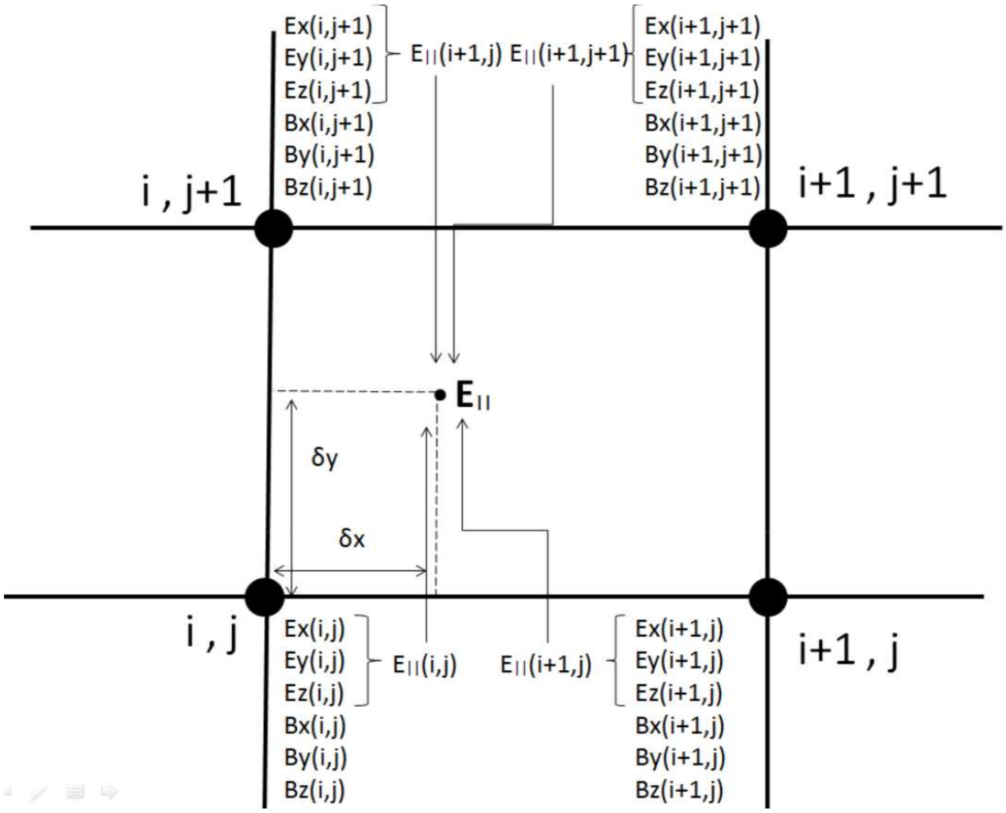

(a) Method 1, calculating $E_{\|}$ at the grid points and then interpolating them giving acceptable results.

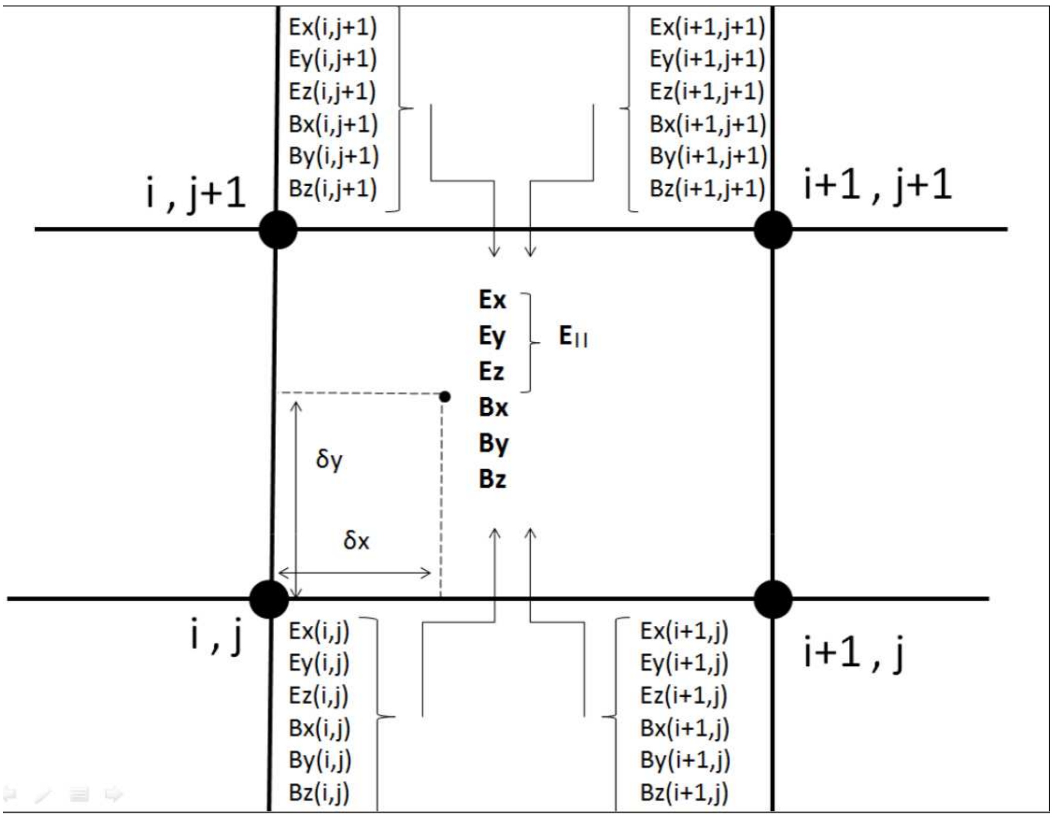

(b) Method 2, interpolating different fields at grid points and then calculating $E_{\|}$ at the particle position causing numerical error.

Figure 5.17

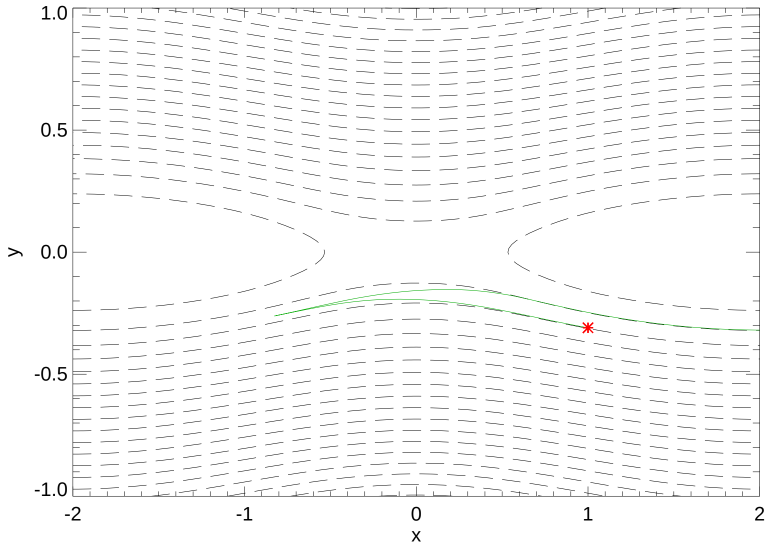

(a) The same as figure 5.15a using GCA.

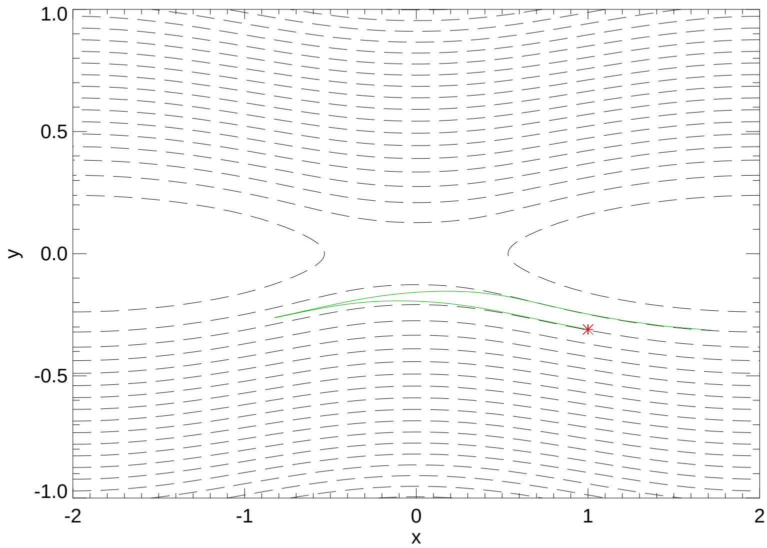

(b) The new trajectory simulated using the full code showing a similar path to that simulated using GCA one.

Figure 5.18: Problem resolved for the case of low μ after introducing the notion of corrected electric field.

(middle-centre panel) shows the $\nabla\ \vec{B}$ component, the 6th (middle-right) shows the $\frac{q}{m}(\vec{E}.\vec{b})$ component (direct acceleration) versus x, the 7th (lower-left) represent the mirroring term, and the final one (lower-centre) corresponds for something related to the variation of electric field along the magnetic field (just a GCA term). Figure 5.20, 5.21, and 5.22 correspond to 3 experiments from the low μ set. What we can say is that $U_{\vec{E}\times\vec{B}}$ value increases whenever we become closer to the reconnection site. This can be deduced first when looking at each $U_{\vec{E}\times\vec{B}}$ plot, as it reaches its maximum

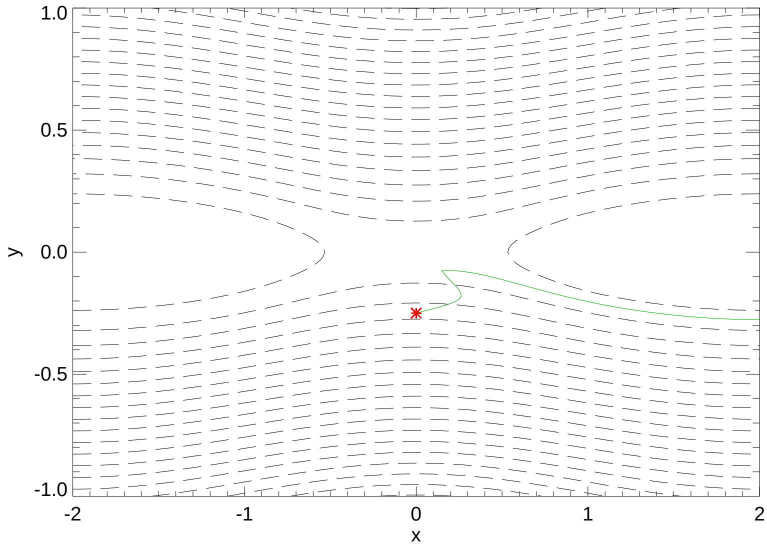

(a) GCA

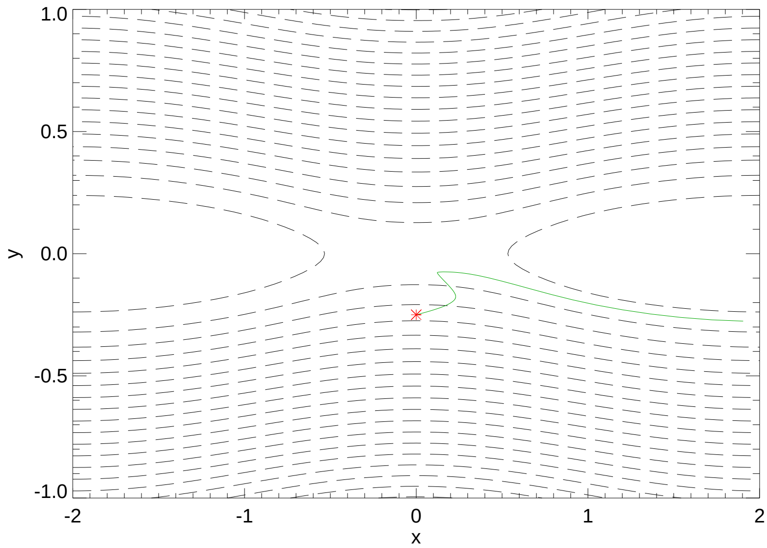

(b) Full trajectory

Figure 5.19: Same but for the high μ case.

when its y is closer to 0, and secondly when comparing $U_{\vec{E}\times\vec{B}}$ plots between figures, for instance in figure 5.20 its maximum value is around 0.0011 corresponding to a maximum y around -0.3 whereas in figure 5.22, it has a maximum value of about 0.008 corresponding to its maximum y around -0.15. The $\frac{q}{m}(\vec{E}.\vec{b})$ term is ~ 0 in any position away from the region around the X-point (this term can be understood when looking at the contour plot of $\vec{E}.\vec{B}/|\vec{B}|$) shown in figure 5.10). We can note the 2 maxima in $U_{\vec{E}\times\vec{B}}$ term when plotted versus x in figure 5.21, these are due to the maximum value of $|\vec{E}|$ as shown in figure 5.9 resembling to be as 2 summits.

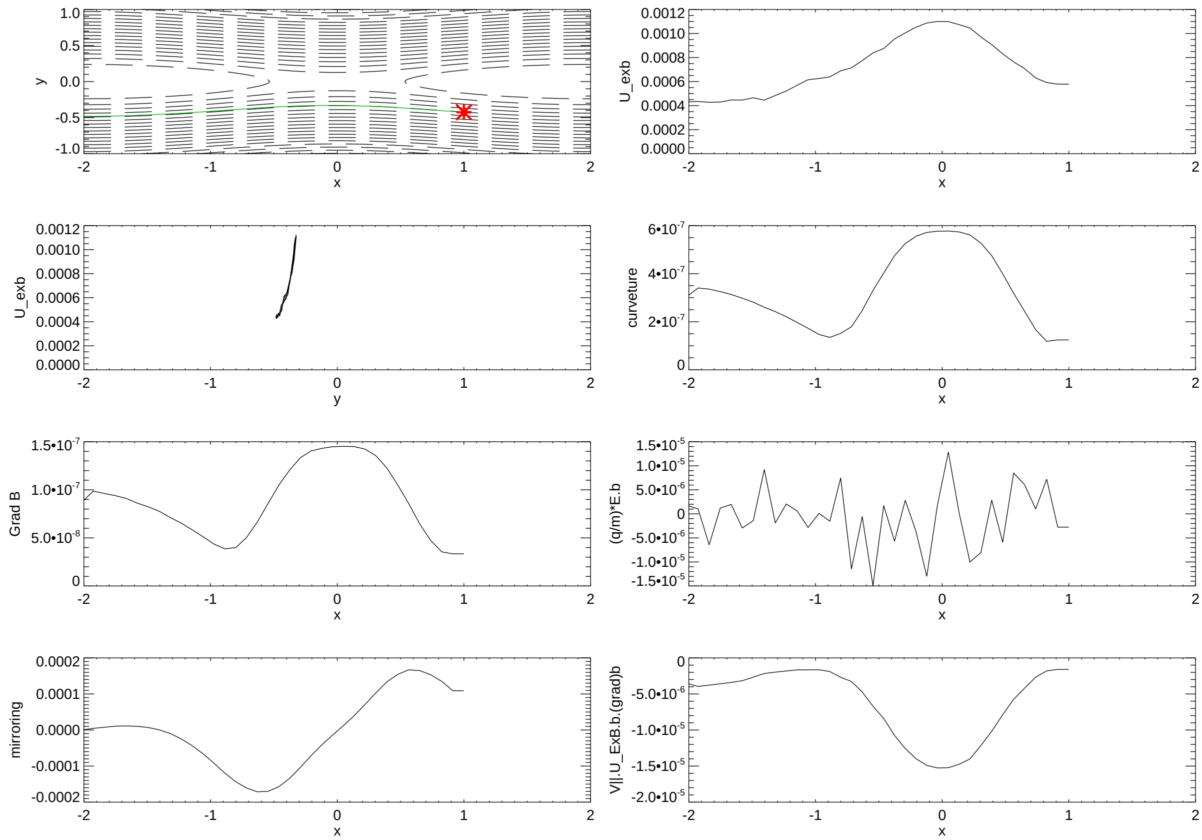

Figure 5.20: Analysing different types of motion accounting for the particle trajectory using the GCA code. The main term accounting for the particle path in this experiment is $\vec{E} \times \vec{B}$. Direct acceleration along field lines can be neglected as the particle is a little bit away from the centre as shown in the 6th panel where the value is fluctuating around zero. All other terms are also very small so the particle does not experience any sudden change.

5.3.5 V$_{gyro}$ and The Magnetic Moment μ

Magnetic moment μ is one of the most important parameters in the context of particle acceleration. The basic equation for the magnetic moment is as follows:

$$\mu = \frac{1}{2} m \frac{v_{gyro}^2}{B}. \tag{5.2}$$

As the mass term is just a constant, it is necessary just to plot is $v_{gyro}^2/2B$. It gives an idea if the particle simulated is adiabatic or not in such a way that if its constant through out the simulation than this means that we are in the adiabatic regime. In the Guiding Centre Approximation Theory μ is assumed constant, where $\frac{d\mu}{dt} = 0$ is one of the equations used within the code. The particle in the full trajectory

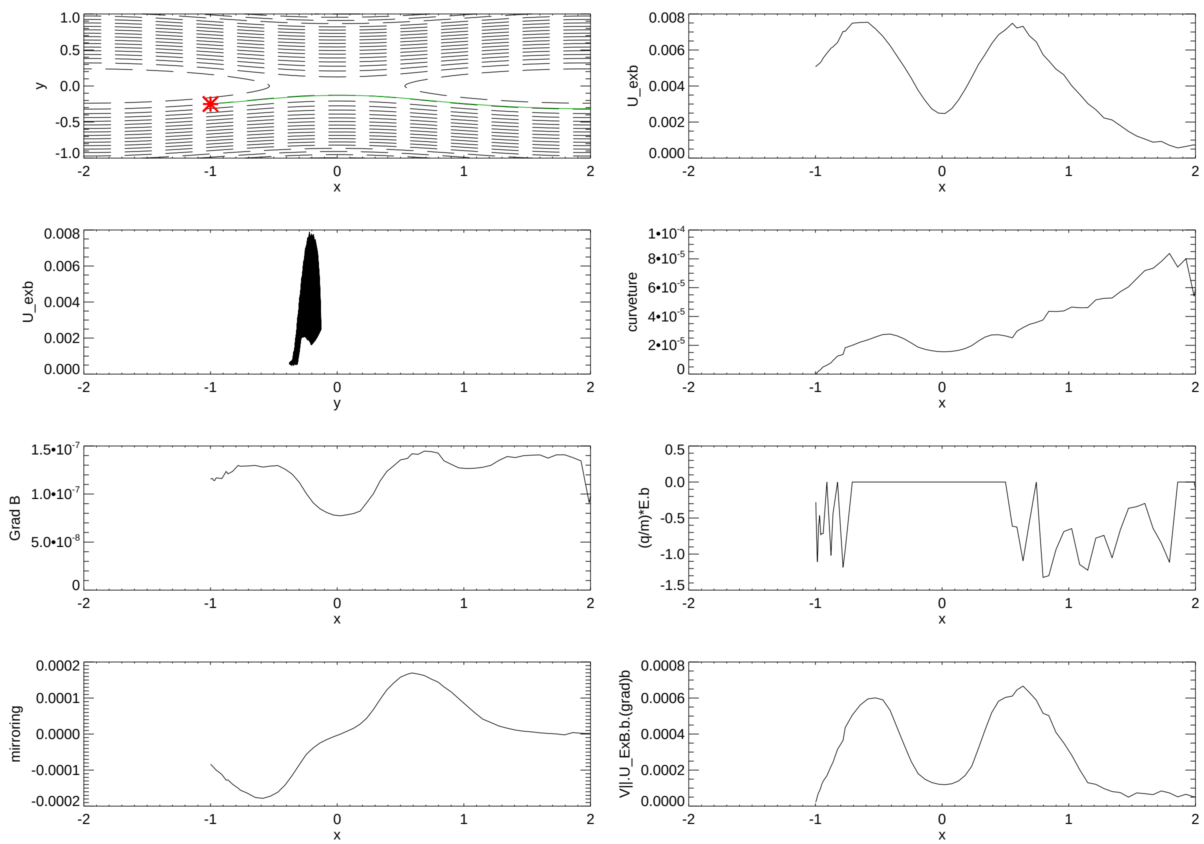

Figure 5.21: Same discussion as before but we could notice that the $\vec{E}.\vec{b}$ term is very high at some places as the particle passes near the centre at the separatrices where electric current is concentrated. The 2 peaks in $U_{\vec{E}\times\vec{B}}$ term are a results for the high value of $|\vec{E}|$ at these specific locations (see figure 5.9).

can move and gyrate in any direction and the trajectory consists of many kinds of motions such as drifting, gyrating, and moving along the field lines. In order to calculate μ we are interested in the gyration term. The particle velocity terms can be written as follows:

$$\vec{V} = \vec{V}_{\parallel} + \vec{V}_{\perp} \tag{5.3}$$

and

$$\vec{V}_{\perp} = \vec{V}_{gyro} + \vec{V}_{drift}. \tag{5.4}$$

The full trajectory code operates in the Cartesian Coordinate, but as $\vec{V}_{gyro}$ can just be extracted from $\vec{V}_{\perp}$ then we need to supply an extra bit of code to do this. The three Cartesian components of the perpendicular velocity ($\vec{V}_{\perp_x}$, $\vec{V}_{\perp_y}$, and $\vec{V}_{\perp_z}$) can be easily calculated by first calculating the three Cartesian terms of $\vec{V}_{\parallel} = \vec{V}.\vec{B}/|\vec{B}|$

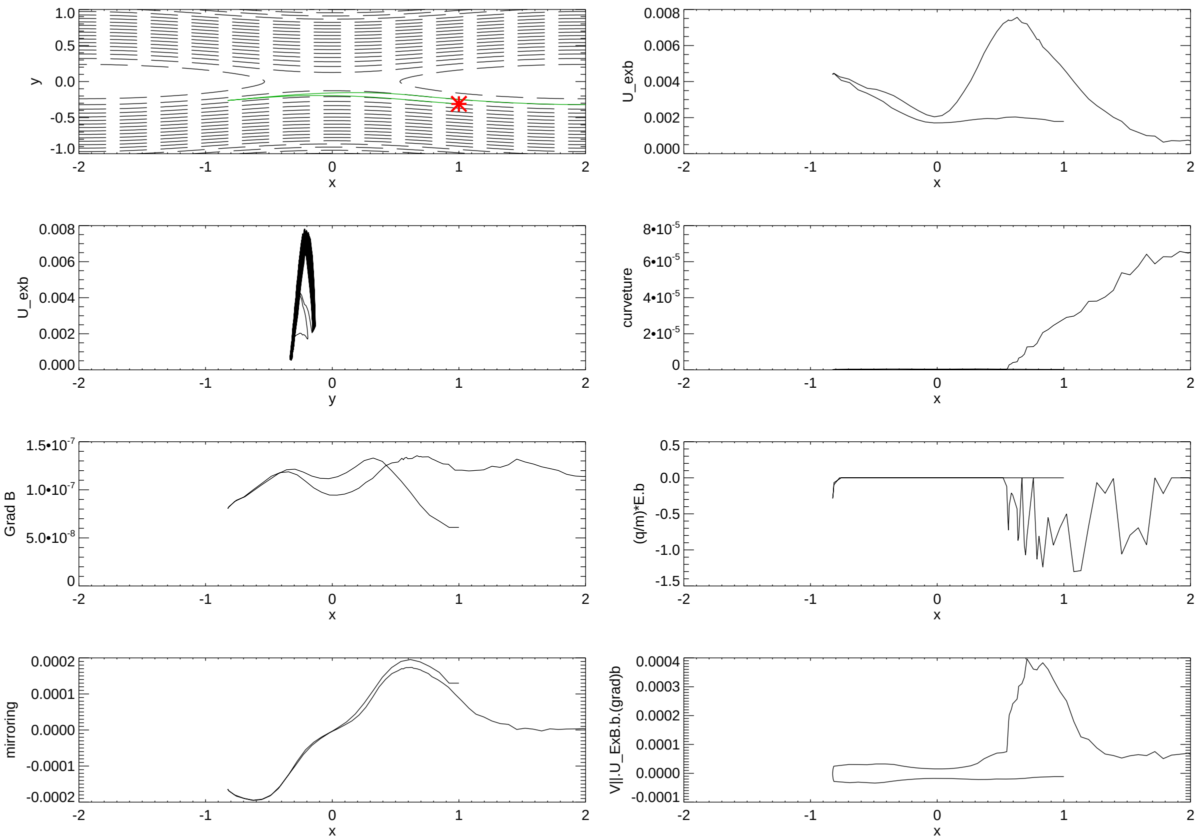

Figure 5.22: A bouncing feature with a sudden change in particle direction could be viewed as a mirroring effect where magnetic field become stronger (see § 2.2.2).

in each iteration and then subtract them from the total velocity. Now we should find a way to separate the 2 different components of $\vec{V}_\perp$, ($\vec{V}_{drift}$ *and* $\vec{V}_{gyro}$). One approach is to use the known drift components for an adiabatic particle; mainly the $\vec{E} \times \vec{B}$ drift, $\nabla\vec{B}$ drift, and the curvature drift (the last 2 terms are mainly very small as shown in figures 5.20, 5.21, and 5.22 so they can be usually neglected). We can calculate these values analytically as we know their expressions from the GCA theory and then subtract them from $\vec{V}_\perp$ and what remains would be $\vec{V}_{gyro}$. This method works if we assume that we are in the GCA regime, but this is not known in advance and later on we will consider cases where GCA is not valid and the particle becomes non-adiabatic; thus, we must think of another method. Figure 5.23 shows the absolute value of $\vec{V}_\perp$ for one of the experiments shown in figure 5.12 over the whole simulation (upper panel) and zoomed in between time 18.4 and 19.6 in dimensionless units (lower panel). What we can notice from this figure (mainly from the lower panel) is that $\vec{V}_\perp$ can be approximated by 2 functions. The

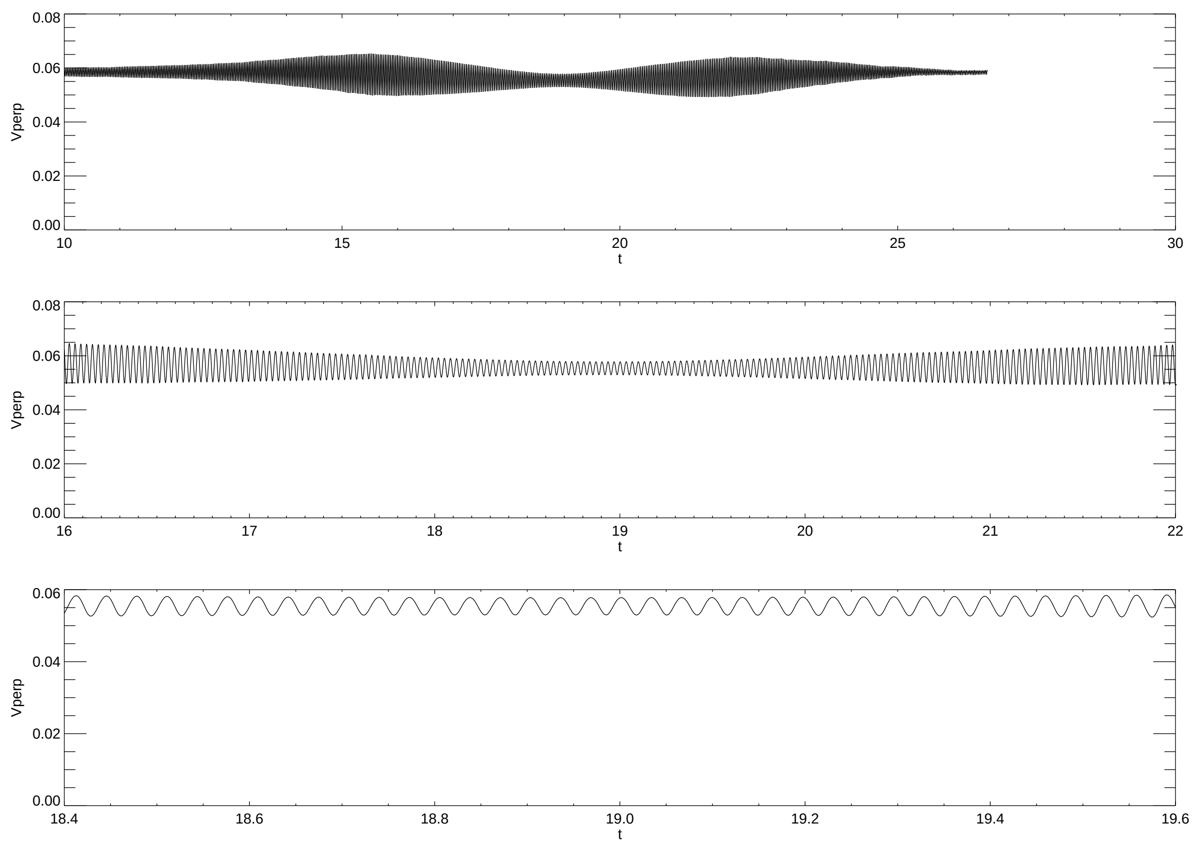

Figure 5.23: $V_\perp$ over the whole time for one of the experiments (upper panel). The middle panel show a little bit of zooming to reveal the plot structure and the lower panel zooms in more to resolve gyrations with constant amplitude. $V_\perp$ can be decomposed into 2 functions as viewed in the last panel. First, is the periodic one corresponding for gyrations and the second is a lifting one corresponding for drifting. A specific function was made to separate both types of motion from each other to evaluate Larmor radius and calculate the magnetic moment μ.

first is a periodic function that we believe corresponds to $\vec{V}_{gyro}$ and the second is a lifting function holding $\vec{V}_\perp$ above the axis which represents $\vec{V}_{drift}$. Thus we now consider the drifting velocity to be a constant function over a small period of time where we average a specific number of gyrations and then subtract this average from the original function ($\vec{V}_\perp$) and what remains should be gyrations centred at the axis. This method should be performed at each direction separately (x, y, and z) by calculating $\vec{V}_{drift_x},\ \vec{V}_{drift_y},\ and\ \vec{V}_{drift_z}$ and then subtract them from there corresponding $\vec{V}_\perp$ to get $\vec{V}_{gyro_x},\ \vec{V}_{gyro_y},\ and\ \vec{V}_{gyro_z}$, and then evaluate the absolute value of $\vec{V}_{gyro}$ which will be used to calculate extra 3 parameters, $\mu,\ r_L,\ and\ \epsilon$. r_L is the Larmor radius, and ϵ gives us an idea on how much the guiding centre theory is applicable having the following formula, $\epsilon = r_L/L_{\nabla B}$, where $L_{\nabla B} = |\vec{B}|/|\nabla\vec{B}$ which represents the length scale of the system. As argued previously, if $\epsilon \ll 1$ then GCA is applicable, otherwise it is not. In order to perform what we have just discussed, we add a small function to our code that averages over gyrations within a specific number of steps specified by the user. This function calculates the magnetic moment μ, r_L, and ϵ and saves them into data files. Then we can use the two approaches (calculating analytically the drifts, and averaging over gyrations) and compare the results. Figure 5.24 shows one of these experiments using the 2 approaches. As we can notice, the 3 components of gyrations are centred at the x-axis and they coincide using the 2 approaches ($|\vec{V}_{gyro}|$ and r_L also coincide), $V_{\vec{E}\times\vec{B}}$ completely coincide with $\vec{V}_{drift}$, μ is $\sim$ constant and coincides with the 2 methods, and $\epsilon \ll 1$.

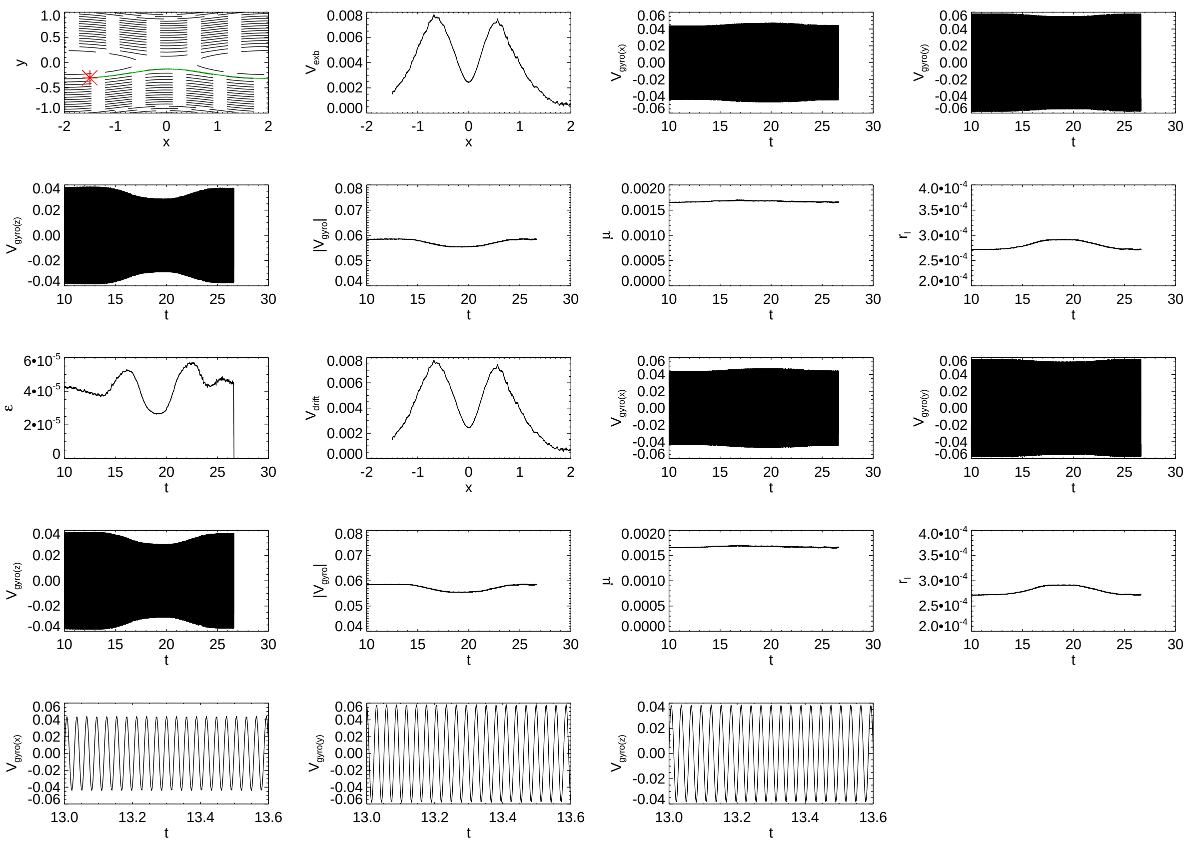

Figure 5.24: 19 plots aims to compare between 2 approaches (analytical calculation of drifts and averaging method). 1^{st} panel is the particle trajectory. The next 7 (moving horizontally) are for analytical calculation of drift term (mainly $V_{\vec{E}\times\vec{B}}$) and its corresponding $\vec{V}_{gyro}$, μ, and r_L. The next 8 plots are for the same parameters but using the averaging method (1^{st} of these 8 is ϵ vs. time). The 2 methods seems to give similar results as GCA is applicable within this experiment and μ is approximately constant (adiabatic particle). The last 3 panels are zooming in inside V_{gyro_x}, V_{gyro_y}, and V_{gyro_z} to reveal there structure precisely.

5.3.6 Non-applicable GCA Regime

All that we reported so far with full trajectory code was in the region where GCA is applicable and the two codes give similar results. Now we go a step further and break the conditions that govern this relation between the guiding centre theory and full trajectory. The main issue is to make the Larmor radius not much smaller than the length scale of the system. This can be achieved by several methods but an easy one is to perform simulations using heavier particles than protons which have larger Larmor radius (another way of doing it for instance is by decreasing the strength of the magnetic field). To do this we just multiply mass-to-charge ratio ($\alpha = m/q$) by a factor κ greater than one. To achieve noticeable result, this number κ should be high enough to show gyrations in the simulated region. First we take it to be 1000 (large enough that no particle exists that has such a mass, but our simulated region is small that is why we need high κ to see differences). Figure 5.25 shows a simulation done both using full trajectory and GCA for the low μ case. Now gyrations from the full trajectory can be easily seen; still the particle mainly follows the field lines, but a small difference of path can be noticed. Actually this difference could arise from the fact that both particles begin moving from the same initial position which is not the guiding centre position, so the GCA particle is not following the guiding centre of full trajectory particle. Hence, this small difference could not be a direct evidence of the non-applicability of GCA. Figure 5.26 shows some plots from the full trajectory to the particle simulated in figure 5.25. We can now see that $V_{\vec{E}\times\vec{B}}$ is different from $\vec{V}_{drift}$, also the parameter ϵ is not so small and closer to 1, and μ now varies significantly. These parameters ensure that this simulated particle is no longer behaving adiabatically and GCA is non-applicable as μ show noticeable inconstancy.

5.3.7 Kinetic Energy calculations

One of the things that can be plotted and compared between the two regimes (applicable and non-applicable GCA) is the kinetic energy of the simulated particle before

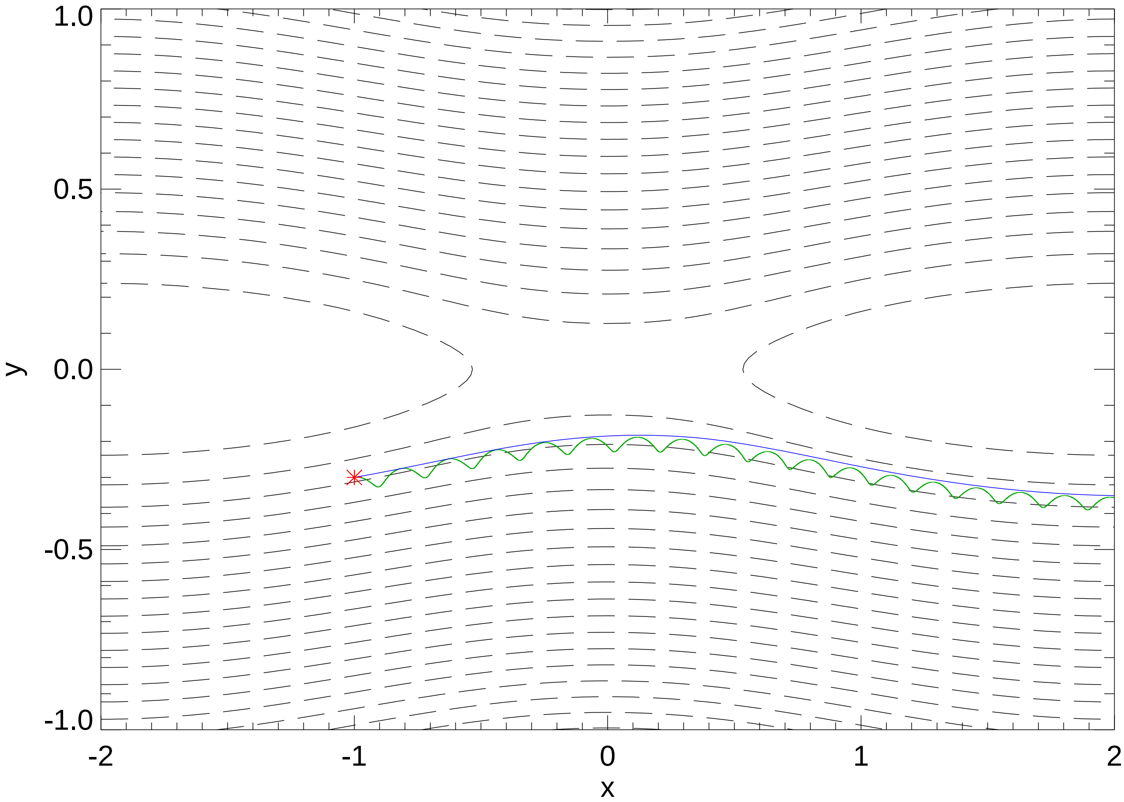

Figure 5.25: 1000 times heavier particle trajectory simulated using both codes (blue for GCA and green for full trajectory). Gyrations now appear without zooming as the Larmor radius is much bigger than before. The difference in path may arise from the fact that the initial position is not the guiding centre one. Energy discussion in the next section will insure the difference.

leaving the domain. Kinetic energy is relevant in our context (particle acceleration in solar flares) as now we can detect radiations from flares and evaluate particles energy gain and kinetics and compare them with simulations. When the guiding centre theory is applicable, we expect that when simulating the same particle using both codes to have almost equal energies at any time and at the end, with a very small error. As most of our simulated particles do not begin or end up with relativistic speeds then the kinetic energy for any particle at any step is:

$$E_K = \frac{1}{2}mv^2 \tag{5.5}$$

The first 2 terms are just constants so we can drop them from plots and comparison, thus we will just consider v^2. Figure 5.27 shows plots for kinetic energy profiles for

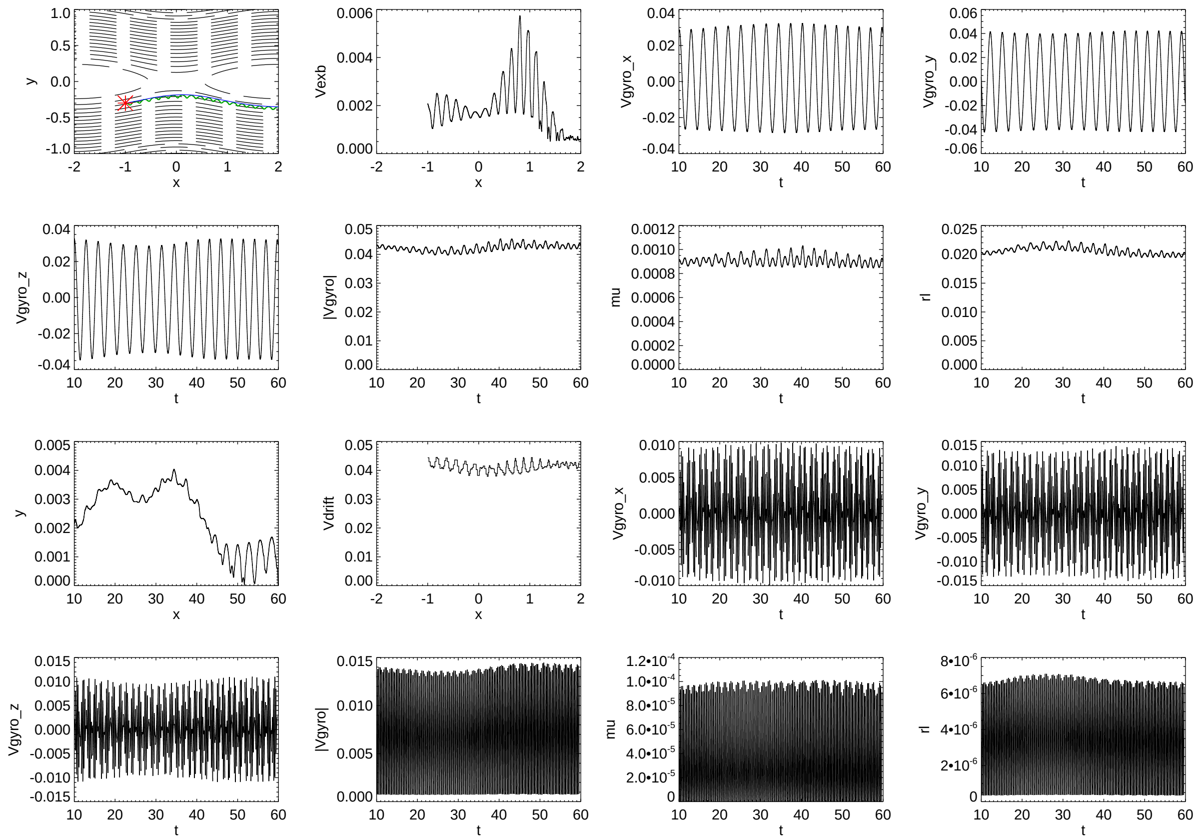

Figure 5.26: Same as figure 5.24 but for the particle simulated using full code in figure 5.25. It can be easily noticed that agreement is not as good as before and μ show a lot of fluctuation.

the experiment shown in the first panel in the regime where GCA is applicable and the particle is relatively far from the origin. We can notice that the 2 curves matches with some few difference (the full trajectory energy curve seems to be more smooth as in GCA not all steps are plotted. We skip saving some data to avoid big data files). We could not plot the 2 curves on top of each other in the same graph as the calculated adaptive time step for sure is different in each code as well as the number of iterations. The error given as follows:

$$error = \frac{|E_{K_{full}} - E_{K_{GCA}}|}{E_{K_{full}}} \tag{5.6}$$

at the final step is, $error = 0.041\%$. If we consider the same particle but now being initially at the origin (the particle simulated in figure 5.13), things may differ slightly. Figure 5.28 shows kinetic energy profile for this particle using both approaches.

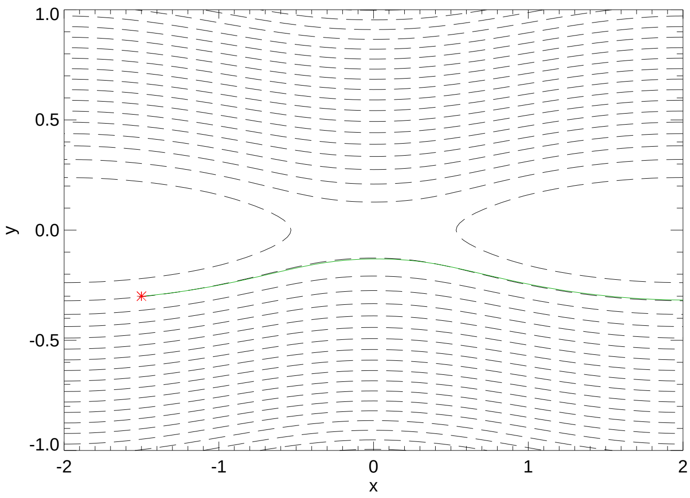

(a) Particle trajectory for one of the experiments.

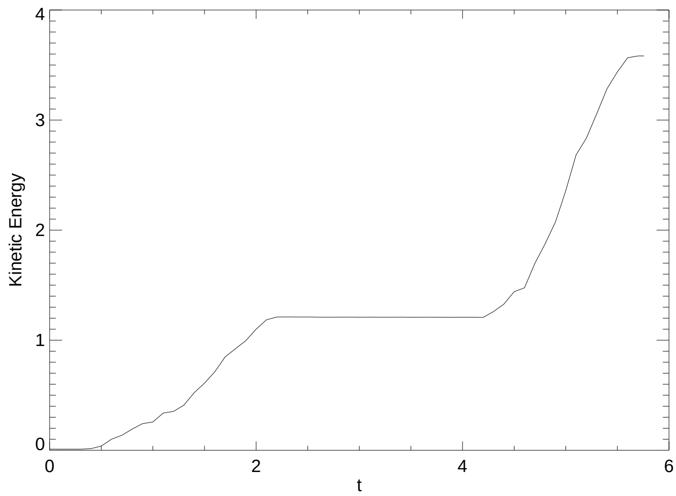

(b) Energy profile through out the whole time for the simulated particle using the full code.

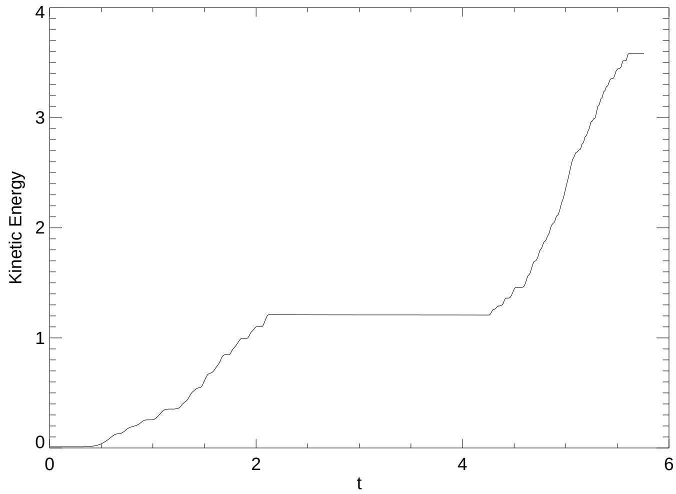

(c) Energy profile using the GCA code.

Figure 5.27: Energy profile comparison between full and GCA codes for one of the experiments in the applicable GCA regime. Both codes give similar profile shape. The full profile is smoother as GCA skip saving some data for data-storage purposes. The energies before ejection were very close with a small error.

The error at the final step is 0.08%, double the previous experiment, which means that acceleration near the origin where particles are less magnetised increase the difference between full trajectory and GCA. The same particle, but now trapped in

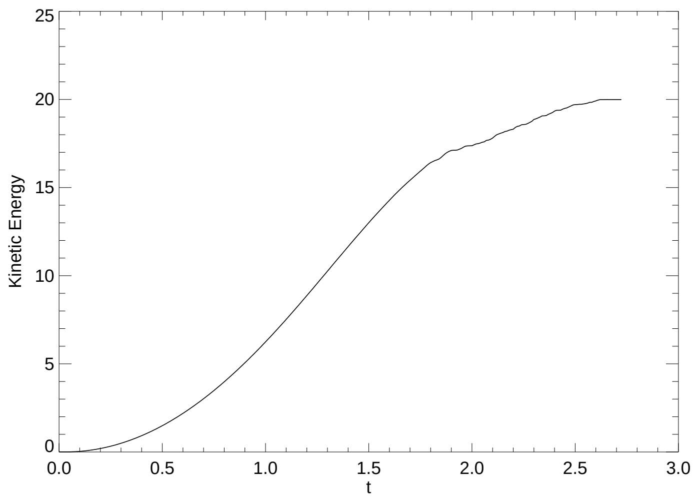

(a) Energy profile using the full code.

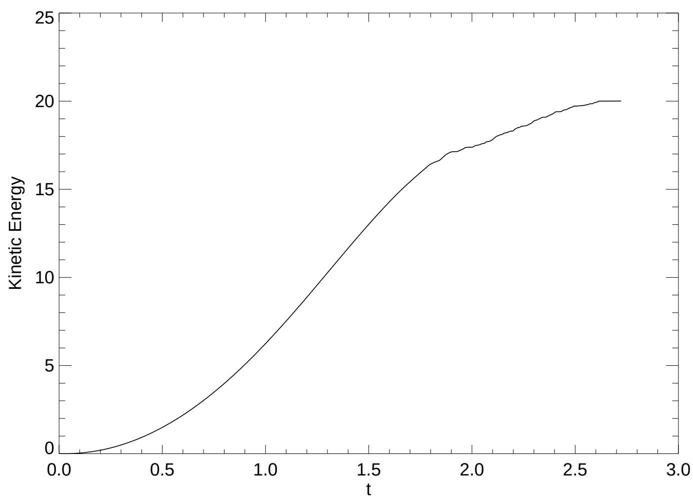

(b) Energy profile using the GCA code.

Figure 5.28: Energy profile comparison for a particle placed initially at the origin. Both look quit similar with an increase in error at the final step.

the magnetic island (portion of the particle trajectory shown in figure 5.12) shows more difference as it experiences more instability and high change in electric field (figure 5.29). The error at the final step is $\sim 0.35\%$, which means that the bound between GCA and full trajectory is the weakest at closed magnetic field regions among other regions.

Now we consider the other case where we choose a specific position and vary the

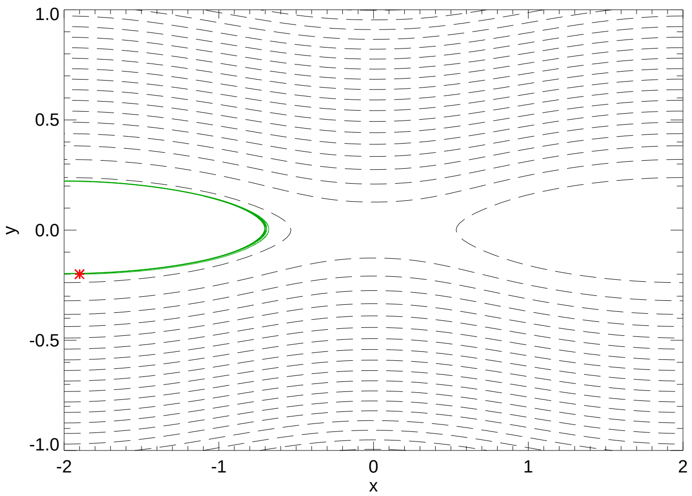

(a) The particle trajectory being trapped in the magnetic island.

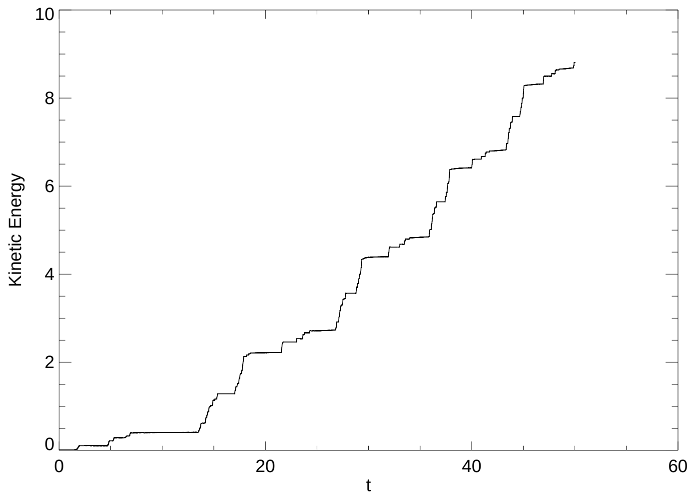

(b) Energy profile using the full code.

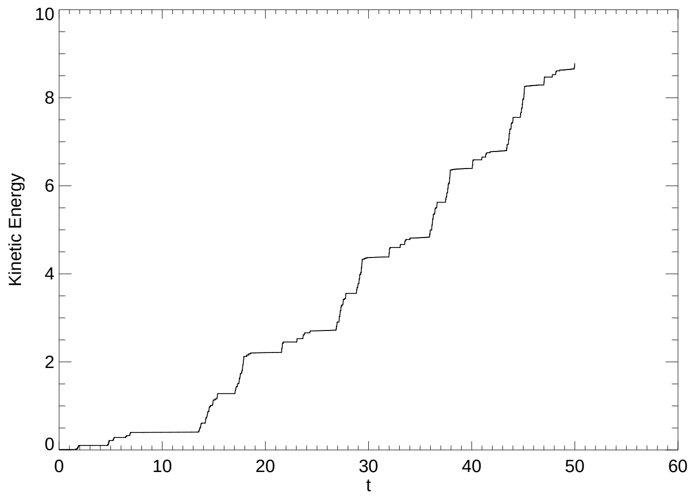

(c) Energy profile using the GCA code.

Figure 5.29: Energy profile comparison for a particle trapped in the left magnetic island. The error at this region is the highest among other regions (open magnetic field regions and near the origin).

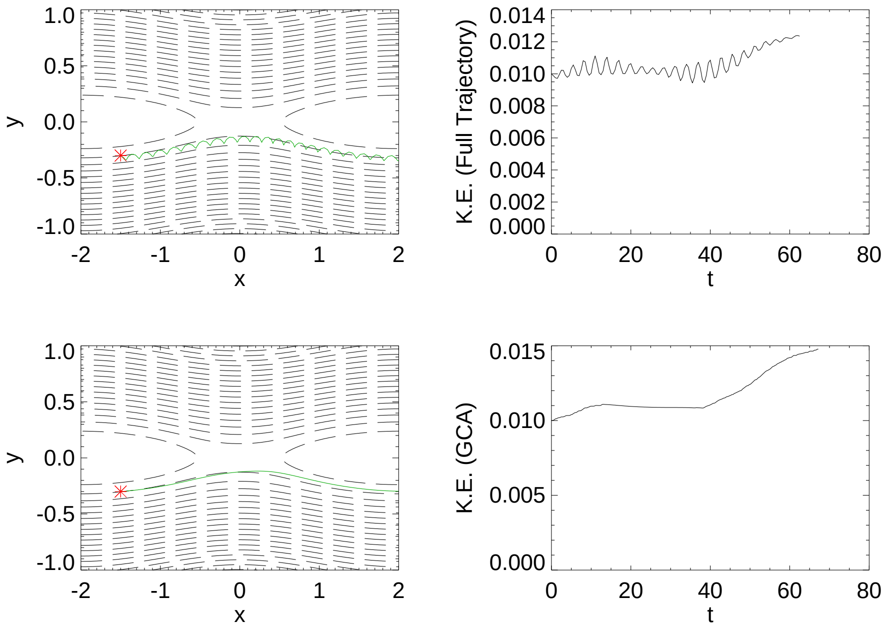

Figure 5.30: Energy profiles for a non-adiabatic heavy particle for full (upper panel) and GCA (lower panel) codes. The full profile will of course show fluctuation as that for trajectory. The final step energy in the two codes is different as expected with a huge error.

mass of the particle. This is an interesting case as it will give us a limitation to what extent can we increase the mass of a particle and the difference of energy remains acceptable. We choose the same position used for the "far from the origin" region as shown in figure 5.27a and increase α by 3 orders of magnitude from 4.4×10^{-3} till 4.4×10^{-1}. The error increased gradually with increasing α having values of 0.49%, 7.47%, and 16.4% respectively. The last 2 experiments can be considered to be in the non-applicable GCA regime and plotting their trajectories from the full code shows their gyrations on the field lines with such a large difference as expected in their final energy between the two approaches. We should note that there is nothing in common between full trajectory data and GCA one for these 2 experiments i.e. time and position are different at the final iteration hence we choose this step to compare energies just because it is the final step. Figure 5.30 shows plots for trajectory and energy profile for the last experiment ($\alpha = 4.4 \times 10^{-1}$) for both calculations (Full and GCA). Gyrations in the full trajectory appear obviously causing gyrations as well in the energy profile.

Chapter 6

Conclusions

We have investigated through our work almost all essential similarities and differences between Full Trajectory and Guiding Centre Approximation test particle approaches using analytical, analytical with numerical tool, and numerical electromagnetic field models to fully compare both approaches. Mainly our aim was to determine the conditions under which it is valid to use guiding centre approximation to calculate particles trajectories on a reconnected current sheet analogous to that formed in solar flares and also when it is acceptable to use electromagnetic field values from a discrete grid. On our way to making such a comparison, we draw out some computational remarks that could be useful in later numerical work. First, we can say that using linear interpolation to calculate different field values is reliable even for quite coarse grids. We used it in all our experiments and it gave small numerical errors, so there is no need to consider more complicated interpolation methods, such as polynomials, at least in similar work like ours. Secondly, as our full code contains two different numerical methods for solving differential equations (Runge-Kutta and Adams-Bashforth, both 4th order), this allow us to compare between them and conclude which is better and more accurate. To judge the efficiency of a numerical method, two things should be taken into account of the following priority, accuracy and time efficiency. When we were testing the full code, we noticed that Runge-Kutta method is more accurate than Adams-Bashforth at certain time steps by 2 orders of magnitude. Concerning time consumption, both methods show similar speeds with differences by fraction of a second, at least in the testing procedure. This leads us to conclude that it is better to use the RK numerical method when solving differential equations.

We developed both relativistic and non-relativistic modules and compared the results. Protons need very high energies (not expected in flare particles) for the relativistic effects to be taken into account while electrons are more sensitive at lower energies. Protons, in most simulations, end up with kinetic energy at most of order of hundreds of MeV, which is comparable with there rest mass of 938.27 MeV/c^2 (relatively massive), thus for protons and heavier particles, only the highest energy particles may be significantly affected by relativistic effects. Alternatively, electrons having light rest masses (0.511 MeV/c^2) with same initial speeds as that given to protons, are accelerated and gain energy to the order of tens and hundreds of MeV which is greater by 2 or 3 orders of magnitude than their rest mass, so relativistic effects matter much more in case of electrons, therefore electrons should be always treated as relativistic particles.

Studying the drift theory theoretically and numerically made us more certain about the influence of the factor $r_l/L_{\nabla B}$ on the accuracy of GCA in general. Whenever this ratio becomes closer to 1, the GCA is less valid. Several experiments were done for the case where the only drift velocity is the ∇B drift. We vary the value of $r_l/L_{\nabla B}$ from $1.67 \times 10^{-3} \ll 1$ to 0.276, and as a result, the error in calculating the drift velocity between GCA and full trajectory increases from 0.06% to 144%. However, the behaviour still qualitatively follows drift theory even with very large $r_l/L_{\nabla B}$ values. An approximate linear relation between Log(error) and Log($r_l/L_{\nabla B}$) of slope 2 was observed indicating that, $error \propto (r_l/L_{\nabla B})^2$, justified by the basic assumption made when deriving GCA in ignoring the term $(r_l/L_{\nabla B})^2$.

In chapter 4 we studied what effects of using discrete data on grid on the accuracy of particle trajectory. We concluded that using linear interpolation causes the error to be inversely proportional to the squaring of the grid size, as expected from Taylor expansion of any linear method. We used a range of grid sizes varying from 16 till 256. We would say that using a grid of 16 or 32 points at better cases will achieve an error of 4.5×10^{-4} away from using heavy particles. A grid size of 64 would be considered as an intermediate range with errors around 10^{-5}, and grids with 128, 256, and more allow the accuracy to reach values of 10^{-6} or 10^{-7}. We proposed that the minimum Nx_{grid} should be used from an error point of view is 128. This will allow the error between calculations using analytical fields and calculations using the same field forms in discrete grid to be at most 10^{-4} for all range of particles (very light to massive ones). We also noticed from calculating the error in energy between full trajectory and GCA having same grid sizes for the whole range of grid sizes from 16 till 256 that it does not have any effect and the error remains constant between the two approaches. We also investigated the effect of varying α, the normalised mass-to-charge ratio, as an indication for the applicability or non-applicability of GCA from an error point of view. We showed out that error decreases slowly when α increase till GCA becomes invalid where error begin to increase rapidly; however, it would not be expected to use GCA with large α values or in the parameter range between $[10^{-3}, 10^{-1}]$, so this is not a serious restriction.

In chapter 5, a full comparison between both test particle approaches was presented using data from MHD simulations of forced reconnection. A numerical problem was discovered in regions where one of the electric field values (parallel or perpendicular) is very small. The problem was in interpolating this weak field where it show a higher value by many orders of magnitude than what we would expect. This numerical issue may change totally the particle behaviour to a very unrealistic one. This was resolved by creating a corrector electric field that dismisses the field that caused the error before interpolation, and then adding it after performing the interpolation. An important remark when performing interpolation in finite grid for any set of parameters, is that it is always better and more accurate to calculate these parameters on the grid points and then interpolate rather than interpolating basic parameters and then evaluating these parameters.

The comparison between both approaches (full trajectory and GCA) lead us to say that both of them give similar results concerning trajectories and energy values when GCA conditions are satisfied i.e. when the Larmor radius is much smaller then the length scale of the system or when the gyro-period is much smaller then the Alfven time. In this case μ is conserved and the particle behaves adiabatically. Besides, we figure out that drifting velocity can be approximated by a constant value at a very small portion of time together with gyration from the perpendicular velocity. When deliberately violating the conditions of GCA by considering very heavy particles, the latter show different path and energy value when simulated with full code from that of GCA.

Since a major application of test particle models is to calculate particle energy gains, it is important to consider the accuracy of kinetic energy calculations. These calculations are relevant to our work on solar flares modelling, as evaluating the energy gain of particles is the main issue when considering particle trajectories that could be compared with observations to have a better understanding of the picture. We performed simulations using the same particle (Helium-3) initially at the three main regions within our reconnected current sheet, far from the origin, at the origin, and at magnetic islands. We noticed that the difference at the final energy between GCA and full trajectory increased between these three regions from very small far away from the origin ($\sim 0.041\%$), then the error was doubled at the origin ($\sim 0.08\%$), than it increases noticeably at magnetic islands to $\sim 0.35\%$. The error in general is small as the particle behaves adiabatically, but this difference in error lead us to say that the accuracy between GCA and full trajectory depend on the initial particle position as well as the nature of this particle. In another set of experiments we choose the first region, far from the origin region, and perform experiments with different values of α ranging from 4.4×10^{-4} till 4.4×10^{-1} with a spacing of one order of magnitude. The error increased as follows: 0.041%, 0.49%, 7.47%, 16.4% respectively. Hence to get an error in final energy below $\sim 0.5\%$ between full trajectory and GCA, the mass of the particle should not exceed 30 times the mass of a proton, at least in regions which are far from origin and magnetic islands which for sure should have less particle mass to be in this range.

To sum up, the overall comparison between full trajectory and GCA leads us to say that in the whole picture full trajectory should be always used when considering particle trajectories. This method performs under any conditions, and has no limitations. On top of that, concerning codes time consumption, there was no such a big difference. Of course GCA is faster (finally it is an approximation method) but also the time taken to evaluate a single particle trajectory using the full code is not that much. Quantitatively, GCA code in worst cases (simulating heavy particles and outputting all time steps), take up to 10 seconds to evaluate the particle trajectory, while full trajectory, with our own version, performing under same conditions as that of GCA could take up to 2 or 3 minutes to complete the same trajectory, which is still acceptable taking into account the difference in equations solved and accuracy. Maybe when considering thousands of particles, things will add up to change this fact but at least we are talking about single particles. Does this mean that there is no point of using GCA? No, one can not ignore the fact that GCA give us more insight on how does specific terms (parallel acceleration, drifting terms, etc...) affect the trajectory as they are fully evaluated separately. This allows us to fully understood different particle motions (following field lines, bouncing, accelerating, etc...) at each step. On the other hand, full code uses approximated methods to calculate these effects, like the one we used to evaluate the drift by averaging over gyrations. It is an argumentative issue, on one side full trajectory is full motion with high accuracy, and GCA fully diagnose each term of motion!!!

6.1 Future Work

During the previous 12 months we investigated individual particle motion in different magnetic and electric field configurations using the two test particle approaches, full trajectory and GCA. On one hand, time was enough to formulate and establish pre-experiment tools to perform several experiments and compare main aspects between the 2 approaches. On the other hand, if more time is given, we could perform the same work but with different numerical tools and physical concepts. For example, considering non-linear interpolation method (e.g. polynomial interpolation), other numerical methods for solving differential equations (e.g. the method of collocation, which is unlike any of the single-step or multi-step methods outputting a function rather than a discrete set of values), perform relativistic experiments using electrons instead of protons as GCA is more useful for electrons and light particles, other analytical fields (e.g. with or without transverse and longitudinal magnetic fields with all possible combinations, weak and strong guiding fields, models more convenient to the case of current sheet in solar flares, etc...) formulating analytical expressions and comparing with simulations, other stages of reconnection rather than the X-point (e.g. pre-reconnection or O-point stage), and many others. This will allow us to extract more computational and physical conclusions, derive more restrictions and limitations for the GCA theory, and to see to what extent they could explain observed features of particle acceleration like energy spectrum. Last but not least, we could simulate large number of particles rather than single particle, which contain a lot of extra physics (Hall term, partial ionisation, Cowling resistivity, parallel thermal conductivity, etc...), and discuss their energy spectrum and compare it with GCA and observational data.

Appendix A

A.1 Important MHD Parameter's Equations

η, the magnetic diffusivity is defined such that:

$$\eta = \frac{1}{\mu_0 \sigma} \tag{A.1}$$

where σ is the conductivity related to collisions between ions and electrons which is related to the plasma temperature. σ is given in the following formula:

$$\sigma = 7 \times 10^{-4}\, T^{3/2} \tag{A.2}$$

The $equation\ of\ state$:

$$p = nk_B T \tag{A.3}$$

for hydrogen plasma we get:

$$p = 2n_e k_B T \tag{A.4}$$

Some dimensionless parameters can be defined to reveal basic properties of the studied plasma, as the plasma beta (β) and magnetic Reynolds number (R_n).

$$\beta = \frac{thermal\,pressure}{magnetic\,pressure} = \frac{p}{B^2/2\mu_0} = \frac{2\mu_0 p}{B^2} \tag{A.5}$$

Coronal plasma is a low beta plasma as it is highly magnetised, thus magnetic pressure dominates the thermal pressure.

$$R_n = \frac{L_0 V_0}{\eta} \tag{A.6}$$

where L_0 and V_0 are the length and velocity scales of the plasma respectively.

Diffusion timescale:

$$\tau_d = L_0^2/\eta. \tag{A.7}$$

Magnetic field lines are wave carriers as they have tension $T = B^2/\mu_0$, so the information will propagate within the plasma at a speed:

$$V_A = \sqrt{T/\rho} = \sqrt{B^2/\mu_0\rho} \tag{A.8}$$

where ρ is the mass density and V_A is termed by the Alfven speed. The timescale of propagation of Alfven waves is:

$$t_A = \frac{L_0}{V_A} \tag{A.9}$$

We can also define a new dimensionless parameter L_u, the Landquist number as:

$$L_u = \frac{\tau_d}{t_A} = \frac{\mu_0 L_0 V_A}{\eta} \tag{A.10}$$

Which is always a very high number in the solar corona.

A.2 Relativistic GCA Equations

$$\frac{d\mathbf{r}}{dt} = \mathbf{u} + \frac{\gamma(v_\parallel)}{\gamma}\mathbf{b} \tag{A.11}$$

$$\mathbf{u} = \mathbf{u}_E + \frac{m}{q}\frac{(\gamma v_\parallel)^2}{\gamma\kappa^2 B}[\mathbf{b}\times(\mathbf{b}\cdot\nabla)\mathbf{b}] + \frac{m}{q}\frac{\mu}{\gamma\kappa^2 B}[\mathbf{b}\times(\nabla(\kappa B))] + \frac{m}{q}\frac{(\gamma v_\parallel)}{\kappa^2 B}[\mathbf{b}\times(\mathbf{b}\cdot\nabla)\mathbf{u}_E]$$

$$+\frac{m}{q}\frac{(\gamma v_\parallel)}{\kappa^2 B}[\mathbf{b}\times(\mathbf{u}_E\cdot\nabla)\mathbf{b}] + \frac{m}{q}\frac{\gamma}{\kappa^2 B}[\mathbf{b}\times(\mathbf{u}_E\cdot\nabla)\mathbf{u}_E] + \frac{1}{\gamma c^2}\frac{E_\parallel}{\kappa^2 B}(\gamma v_\parallel)[\mathbf{b}\times\mathbf{u}_E] \tag{A.12}$$

$$\frac{d(\gamma v_\parallel)}{dt} = \frac{q}{m}\mathbf{E}\cdot\mathbf{b} - \frac{\mu}{\gamma}(\mathbf{b}\cdot\nabla(\kappa B)) + (\gamma v_\parallel)\mathbf{u}_E\cdot((\mathbf{b}\cdot\nabla)\mathbf{b}) + \gamma\mathbf{u}_E\cdot((\mathbf{u}_E\cdot\nabla)\mathbf{b}) \quad (A.13)$$

$$\gamma = \sqrt{\frac{c^2 + (\gamma v_\parallel)^2 + 2\mu B}{c^2 - u^2}} \quad (A.14)$$

$$\frac{d\mu}{dt} = 0 \quad (A.15)$$

$\mathbf{r}$(t) is the position vector, $\mathbf{u}$ is the particle drift velocity perpendicular to the magnetic field, $v_\parallel$ is the particle velocity parallel to the magnetic field, $\mathbf{u}_E = \frac{\mathbf{E}\times\mathbf{b}}{B}$ is the local $\vec{E}\times\vec{B}$ drift velocity, and $\mathbf{b}$ is the magnetic field direction vector $\mathbf{b} = \mathbf{B}$/B. γ is the relativistic factor, $\gamma = \frac{c}{\sqrt{c^2-v^2}}$, where v is the absolute particle velocity and κ is the coefcient reducing the field value to the particle frame of reference, $\kappa = \sqrt{1 - u_E^2/c^2}$. Finally, μ is the particle magnetic moment, $\mu = u_g^2/2B$.

A.3 Resistive MHD Equations

$$\frac{\partial\rho}{\partial t} = -\boldsymbol{\nabla}\cdot(\rho\boldsymbol{v}) \quad (A.16)$$

$$\frac{\partial\boldsymbol{v}}{\partial t} = -(\boldsymbol{v}\cdot\boldsymbol{\nabla})\boldsymbol{v} - \frac{1}{\rho}\boldsymbol{j}\times\boldsymbol{B} - \frac{1}{\rho}\boldsymbol{\nabla}p \quad (A.17)$$

$$\frac{\partial w}{\partial t} = -(\boldsymbol{v}\cdot\boldsymbol{\nabla})w - (\gamma-1)w\,\boldsymbol{\nabla}\cdot\boldsymbol{v} + \frac{\eta}{\rho}j^2 \quad (A.18)$$

$$\frac{\partial\boldsymbol{B}}{\partial t} = \boldsymbol{\nabla}\times[\boldsymbol{v}\times\boldsymbol{B}] - \boldsymbol{\nabla}\times(\eta\boldsymbol{j}) \quad (A.19)$$

$$\boldsymbol{j} = \frac{1}{\mu_0}[\boldsymbol{\nabla}\times\boldsymbol{B}] \quad (A.20)$$

where w is the specific internal energy density related to pressure and density as $p = (\gamma$ - 1)ρw, and μ_0 is the magnetic permeability. All other parameters with their standard definitions.

A.4 Analytical Form Derivation

The main equation to be solved is the Lorentz equation given as:

$$\frac{dv}{dt} = \frac{q}{m}(\mathbf{E} + \mathbf{v}\times\mathbf{B}) \quad (A.21)$$

In our case:

$$\vec{v} \times \vec{B} = (B_z v_y - B_y v_z)\vec{i} - B_z v_x \vec{j} + B_y v_x \vec{k} \tag{A.22}$$

and so:

$$\frac{dv_x}{dt} = \frac{q}{m}(B_z v_y - B_y v_z) \tag{A.23}$$

$$\frac{dv_y}{dt} = -\frac{q}{m}(B_z v_x) \tag{A.24}$$

$$\frac{dv_z}{dt} = \frac{q}{m}(E_z + B_y v_x) \tag{A.25}$$

or in other words we would say (dot represent a derivative with respect to time):

$$\ddot{x} = \frac{q}{m}(B_z \dot{y} - B_y \dot{z}) \tag{A.26}$$

$$\ddot{y} = -\frac{qB_z}{m}\dot{x} \tag{A.27}$$

$$\ddot{z} = \frac{q}{m}(E_z + B_y \dot{x}) \tag{A.28}$$

so

$$\dot{y} = -\frac{qB_z}{m}(x - x_0) + \dot{y_0} \tag{A.29}$$

$$\dot{z} = \frac{q}{m}(E_z t + B_y(x - x_0)) + \dot{z_0} \tag{A.30}$$

Thus

$$\ddot{x} = \frac{q}{m}\Big[B_z\Big[-\frac{qB_z}{m}x + \frac{qB_z}{m}x_0 + \dot{y_0}\Big] - B_y\Big[\frac{qE_z}{m}t + \frac{qB_y}{m}x - \frac{qB_y}{m}x_0 + \dot{z_0}\Big]\Big] \tag{A.31}$$

Hence

$$\ddot{x} = -\Big(\frac{qB_z}{m}\Big)^2 x + \Big(\frac{qB_z}{m}\Big)^2 x_0 + \frac{qB_z}{m}\dot{y_0} - \frac{q^2 B_y E_z}{m^2}t - \Big(\frac{qB_y}{m}\Big)^2 x + \Big(\frac{qB_y}{m}\Big)^2 x_0 - \frac{qB_y}{m}\dot{z_0} \tag{A.32}$$

a little bit of arranging

$$\ddot{x} + \Big[\Big(\frac{qB_z}{m}\Big)^2 + \Big(\frac{qB_y}{m}\Big)^2\Big]x = \Big[\Big(\frac{qB_z}{m}\Big)^2 + \Big(\frac{qB_y}{m}\Big)^2\Big]x_0 + \frac{qB_z}{m}\dot{y_0} - \frac{qB_y}{m}\dot{z_0} - \frac{q^2 B_y E_z}{m^2}t \tag{A.33}$$

now assuming

$$\omega^2 = \left(\frac{qB_z}{m}\right)^2 + \left(\frac{qB_y}{m}\right)^2 \tag{A.34}$$

using the auxiliary solution

$$r^2 + \omega^2 = 0 \tag{A.35}$$

$$r = \pm i\omega \tag{A.36}$$

and so

$$x_1 = Ae^{iwt} + Ce^{-iwt} \tag{A.37}$$

taking just the real parts

$$x_1 = Ucos(\omega t) + Vsin(\omega t) \tag{A.38}$$

the second solution would be linear such that:

$$x_2 = Pt + Q \tag{A.39}$$

x_1 and x_2 both satisfy the equation and hence their addition is also a solution, thus

$$x = x_1 + x_2 \tag{A.40}$$

as x_2 is a solution then we can substitute to get the constants P and Q, i.e.:

$$\omega^2(Pt + Q) = -\frac{q^2 B_y E_z}{m^2} t + \omega^2 x_0 + \frac{qB_z}{m}\dot{y}_0 - \frac{qB_y}{m}\dot{z}_0 \tag{A.41}$$

by comparison:

$$P = -\frac{B_y E_z}{B_z^2 + B_y^2} \tag{A.42}$$

and

$$Q = x_0 + \frac{B_z \dot{y}_0 - B_y \dot{z}_0}{\frac{q}{m}(B_z^2 + B_y^2)} \tag{A.43}$$

Therefore:

$$x = Ucos(\omega t) + Vsin(\omega t) - \frac{B_y E_z}{B_z^2 + B_y^2} t + \frac{B_z \dot{y}_0 - B_y \dot{z}_0}{\frac{q}{m}(B_z^2 + B_y^2)} + x_0 \tag{A.44}$$

initially at $t = 0$, $x = x_0$ and thus we get:

$$U = \frac{B_y \dot{z}_0 - B_z \dot{y}_0}{\frac{q}{m}(B_y^2 + B_z^2)} \tag{A.45}$$

now differentiating x and substituting at $t = 0$, we get

$$V = \frac{m\dot{x}_0}{q(B_y^2 + B_z^2)^{\frac{1}{2}}} + \frac{mB_y E_z}{q(B_y^2 + B_z^2)^{\frac{3}{2}}} \tag{A.46}$$

Finally we can substitute to get the final answer for positions and velocities as follows:

$$x = \frac{m(B_y \dot{z}_0 - B_z \dot{y}_0)}{q(B_y^2 + B_z^2)} cos(\omega t) + \Big[\frac{m\dot{x}_0}{q(B_y^2 + B_z^2)^{\frac{1}{2}}} + \frac{mB_y E_z}{q(B_y^2 + B_z^2)^{\frac{3}{2}}}\Big] sin(\omega t) - \frac{B_y E_z}{B_y^2 + B_z^2} t$$

$$+ \frac{m(B_z \dot{y}_0 - B_y \dot{z}_0)}{q(B_y^2 + B_z^2)} + x_0 \tag{A.47}$$

$$y = \frac{mB_z(B_z \dot{y}_0 - B_y \dot{z}_0)}{q(B_y^2 + B_z^2)^{\frac{3}{2}}} sin(\omega t) + \Big[\frac{mB_z \dot{x}_0}{q(B_y^2 + B_z^2)} + \frac{mB_y B_z E_z}{q(B_y^2 + B_z^2)^2}\Big] cos(\omega t) + \frac{qB_y B_z E_z}{2m(B_y^2 + B_z^2)} t^2$$

$$- \frac{B_z(B_z \dot{y}_0 - B_y \dot{z}_0)}{B_y^2 + B_z^2} t + \dot{y}_0 t - \frac{mB_z \dot{x}_0}{q(B_y^2 + B_z^2)} - \frac{mB_y B_z E_z}{q(B_y^2 + B_z^2)} + y_0 \tag{A.48}$$

$$z = \frac{qE_z}{2m} t^2 + \frac{mB_y(B_y \dot{z}_0 - B_z \dot{y}_0)}{q(B_y^2 + B_z^2)^{\frac{3}{2}}} sin(\omega t) - \Big[\frac{mB_y \dot{x}_0}{q(B_y^2 + B_z^2)} + \frac{mB_y^2 E_z}{q(B_y^2 + B_z^2)^2}\Big] cos(\omega t) - \frac{qB_y^2 E_z}{2m(B_y^2 + B_z^2)} t^2$$

$$+ \frac{B_y(B_z \dot{y}_0 - B_y \dot{z}_0)}{B_y^2 + B_z^2} t + \dot{z}_0 t + \frac{mB_y \dot{x}_0}{q(B_y^2 + B_z^2)} + \frac{mB_y^2 E_z}{q(B_y^2 + B_z^2)^2} + z_0 \tag{A.49}$$

$$vx = -\frac{(B_y \dot{z}_0 - B_z \dot{y}_0)}{(B_y^2 + B_z^2)^{\frac{1}{2}}} sin(\omega t) + \Big[\dot{x}_0 + \frac{B_y E_z}{B_y^2 + B_z^2}\Big] cos(\omega t) - \frac{B_y E_z}{B_y^2 + B_z^2} \tag{A.50}$$

$$vy = \frac{B_z(B_z \dot{y}_0 - B_y \dot{z}_0)}{B_y^2 + B_z^2} cos(\omega t) - \Big[\frac{B_z \dot{x}_0}{(B_y^2 + B_z^2)^{\frac{1}{2}}} + \frac{B_y B_z E_z}{(B_y^2 + B_z^2)^{\frac{3}{2}}}\Big] sin(\omega t) + \frac{qB_y B_z E_z}{m(B_y^2 + B_z^2)} t$$

$$- \frac{B_z(B_z \dot{y}_0 - B_y \dot{z}_0)}{B_y^2 + B_z^2} + \dot{y}_0 \tag{A.51}$$

$$vz = \frac{qE_z}{m}t + \frac{B_y(B_y\dot{z_0} - B_z\dot{y_0})}{B_y^2 + B_z^2}cos(\omega t) + \Big[\frac{B_y\dot{x_0}}{(B_y^2 + B_z^2)^{\frac{1}{2}}} + \frac{B_y^2 E_z}{(B_y^2 + B_z^2)^{\frac{3}{2}}}\Big]sin(\omega t) - \frac{qB_y^2 E_z}{m(B_y^2 + B_z^2)}t$$
$$+ \frac{B_y(B_z\dot{y_0} - B_y\dot{z_0})}{B_y^2 + B_z^2} + \dot{z_0} \tag{A.52}$$

A.5 RK4 Method

Runge-Kutta methods are a family of implicit and explicit iterative methods that solves ordinary differential equations of the form:

$$\frac{dy}{dx} = f(x, y)$$

$$y(0) = y_0 \tag{A.53}$$

Runge-Kutta 4th order method is a member of this family based on the following numerical scheme:

$$y_{i+1} = y_i + (a_1k_1 + a_2k_2 + a_3k_3 + a_4k_4)h \tag{A.54}$$

where knowing the value of $y = y_i$ at x_i, allow us to find the value of $y = y_{i+1}$ at x_{i+1}, and $h = x_{i+1} - x_i$. Expanding equation A.54 to the first five terms of Taylor series and substituting $dy/dx = f(x, y)$ and h, one can get:

$$y_{i+1} = y_i + f(x_i, y_i)h + \frac{1}{2!}f^{'}(x_i, y_i)h^2 + \frac{1}{3!}f^{''}(x_i, y_i)h^3 + \frac{1}{4!}f^{'''}(x_i, y_i)h^4 \tag{A.55}$$

One of the popular solutions used for equation A.55 is:

$$y_{i+1} = y_i + \frac{1}{6}(k_1 + 2k_2 + 2k_3 + k_4)h$$

$$k_1 = f(x_i, y_i)$$

$$k_2 = f(x_i + \frac{1}{2}h, y_i + \frac{1}{2}k_1h)$$

$$k_3 = f(x_i + \frac{1}{2}h, y_i + \frac{1}{2}k_2h)$$

$$k_4 = f(x_i + h, y_i + k_3 h) \tag{A.56}$$

Our Full Trajectory code uses the presented numerical scheme for solving the Lorentz equation of motion.

A.6 A-B4 Method

Adams-Bashforth methods are also a family for numerically solving ordinary differential equations of the same form as in equation A.53 where A-B4 is a one member of this family. Instead of taking some intermediate steps (e.g. half step as in RK4), A-B4 uses a linear multi-step process that uses previous calculated steps rather than discarding them as in RK to calculate the next step. The numerical scheme for A-B4 is:

$$y_{i+4} = y_{i+3} + h\Big[\frac{55}{24}f(t_{i+3}, y_{i+3}) - \frac{59}{24}f(t_{i+2}, y_{i+2}) + \frac{37}{24}f(t_{i+1}, y_{i+1}) - \frac{3}{8}f(t_i, y_i)\Big]. \tag{A.57}$$

Mainly, just one initial condition is given for the problem, so the other three initial needed values for this method to operate can be computed using other methods like Euler or RK. In our programmed full trajectory code, we evaluate these three values using RK4 and then A-B4 continue normally.

A.7 Analytical Expressions For Some GCA Values

Following up from § 4.1 in chapter 4 we present the analytical expressions for $\nabla|\vec{B}|$, $(\vec{b}.\vec{\nabla})\vec{b}$, $\frac{\vec{E}\times\vec{B}}{B^2}$, and $\vec{E}.\vec{b}$ for the chosen magnetic and electric configuration.

$$\frac{\partial|B|}{\partial x} = \frac{B_0}{b^2}\Big[\Big(\frac{y}{a}\Big)^2 + \Big(\frac{x}{b}\Big)^2 + 1\Big]^{-1/2} x \tag{A.58}$$

$$\frac{\partial|B|}{\partial y} = \frac{B_0}{a^2}\Big[\Big(\frac{y}{a}\Big)^2 + \Big(\frac{x}{b}\Big)^2 + 1\Big]^{-1/2} y \tag{A.59}$$

$$\frac{\partial|B|}{\partial z} = 0 \tag{A.60}$$

$$[(\vec{b}.\vec{\nabla})\vec{b}]_i = -y^2\Big[y^2+\Big(\frac{x}{b}\Big)^2+1\Big]^{-2}\frac{x}{b^2}+x\Big[y^2+\Big(\frac{x}{b}\Big)^2+1\Big]^{-1/2}\Big[\Big(\frac{y}{a}\Big)^2+x^2+1\Big]^{-1/2}$$
$$-xy^2\Big[y^2+\Big(\frac{x}{b}\Big)^2+1\Big]^{-3/2}\Big[\Big(\frac{y}{a}\Big)^2+x^2+1\Big]^{-1/2} \tag{A.61}$$

$$[(\vec{b}.\vec{\nabla})\vec{b}]_j = y\Big[x^2+\Big(\frac{y}{a}\Big)^2+1\Big]^{-1/2}\Big[y^2+\Big(\frac{x}{b}\Big)^2+1\Big]^{-1/2}-yx^2\Big[x^2+\Big(\frac{y}{a}\Big)^2+1\Big]^{-3/2}\Big[\Big(y^2+\frac{x}{b}\Big)^2+1\Big]^{-1/2}$$
$$-\frac{x^2y}{a^2}\Big[x^2+\Big(\frac{y}{a}\Big)^2+1\Big]^{-2} \tag{A.62}$$

$$[(\vec{b}.\vec{\nabla})\vec{b}]_k = \frac{xy}{b^2}\Big[\Big(\frac{y}{a}\Big)^2+\Big(\frac{x}{b}\Big)^2+1\Big]^{-3/2}\Big[y^2+\Big(\frac{x}{b}\Big)^2+1\Big]^{-1/2}-\frac{xy}{a^2}\Big[\Big(\frac{y}{a}\Big)^2+\Big(\frac{x}{b}\Big)^2+1\Big]^{-3/2}$$
$$\Big[x^2+\Big(\frac{y}{a}\Big)^2+1\Big]^{-1/2} \tag{A.63}$$

$$\Big[\frac{\vec{E}\times\vec{B}}{B^2}\Big]_i = \frac{E_0x}{bB_0}\frac{1}{[(\frac{y}{a})^2+(\frac{x}{b})^2+1]} \tag{A.64}$$

$$\Big[\frac{\vec{E}\times\vec{B}}{B^2}\Big]_j = -\frac{E_0y}{aB_0}\frac{1}{[(\frac{y}{a})^2+(\frac{x}{b})^2+1]} \tag{A.65}$$

$$\Big[\frac{\vec{E}\times\vec{B}}{B^2}\Big]_k = 0 \tag{A.66}$$

$$\vec{E}.\vec{b} = \frac{E_0}{\sqrt{(\frac{y}{a})^2+(\frac{x}{b})^2+1}} \tag{A.67}$$

A.8 Magnetic Field and Velocity Stream Lines Derivation

There are 2 ways to plot magnetic field lines on a current sheet laying on the $x-y$ plane. The first is by calculating the equation of field lines such that:

$$\frac{dx}{B_x} = \frac{dy}{B_y} \tag{A.68}$$

Assuming $a = b$ in equations 4.1 and 4.2, one can find:

$$xdx = ydy \tag{A.69}$$

integrating both sides and rearranging we get:

$$\frac{1}{2}(x^2 - y^2) = constant \tag{A.70}$$

These field lines are magnetic field lines. The second way of doing it, is to calculate magnetic potential, in our case we have:

$$\frac{\partial A_z}{\partial y} = B_x = B_0 \frac{y}{a}$$

$$\frac{\partial A_z}{\partial x} = -B_y = -B_0 \frac{x}{b} \tag{A.71}$$

integrating, we get:

$$A_z = \frac{B_0 y^2}{2a} + f(x)$$

$$A_z = \frac{-B_0 x^2}{2b} + f(y) \tag{A.72}$$

comparing and knowing that we choose $a = b$, therefore:

$$A_z = \frac{B_0}{2a}(y^2 - x^2) \tag{A.73}$$

One interesting thing we can do here, is evaluating velocity stream lines and overplot them on magnetic field lines to now how inflow and outflow of plasma would happen. The plasma is driven to the current sheet by the $\vec{E} \times \vec{B}$ drift such that:

$$\vec{V}_{E\times B} = \frac{\vec{E} \times \vec{B}}{B^2} \tag{A.74}$$

evaluating and arranging, we get:

$$\vec{V}_{E\times B}|_x = -\frac{E_0 x}{B_0 b} \frac{1}{(\frac{y}{a})^2 + (\frac{x}{b})^2 + 1}\,\vec{i}$$

$$\vec{V}_{E\times B}|_y = \frac{E_0 y}{B_0 a} \frac{1}{(\frac{y}{a})^2 + (\frac{x}{b})^2 + 1}\,\vec{j}$$

$$\vec{V}_{E\times B}|_z = 0\,\vec{k} \tag{A.75}$$

Now to calculate equations of field lines we set:

$$\frac{dx}{V_x} = \frac{dy}{V_y} \tag{A.76}$$

which gives:

$$\frac{x}{dx} = -\frac{y}{dy} \tag{A.77}$$

integrating and arranging yields:

$$xy = constant \tag{A.78}$$

which is the simple equation of a stagnation point.

Bibliography

Arber, T. D., Longbottom, A. W., Gerrard, C. L., & Milne, A. M. 2001, Journal of Computational Physics, 171, 151

Aschwanden, M. J. 2002, Space Sci.Rev., 101, 1

Aurass, H., Vršnak, B., & Mann, G. 2002, A&A, 384, 273

Battaglia, M., Fletcher, L., & Benz, A. O. 2009, A&A, 498, 891

Benz, A., ed. 2002, Astrophysics and Space Science Library, Vol. 279, Plasma Astrophysics, second edition

Benz, A. O. 2008, Living Reviews in Solar Physics, 5, 1

Birdsall, C. K. 1991, IEEE Transactions on Plasma Science, 19, 65

Birn, J., & Priest, E. R. 2007, Reconnection of magnetic fields : magnetohydrodynamics and collisionless theory and observations, ed. Birn, J. & Priest, E. R.

Biskamp, D. 1986, Physics of Fluids, 29, 1520

Borrero, J. M., & Ichimoto, K. 2011, Living Reviews in Solar Physics, 8, 4

Brown, J. C. 1971, Solar Phys., 18, 489

Browning, P. K., & Vekstein, G. E. 2001, Journal of Geophysical Research, 106, 18677

Carrington, R. C. 1859, MNRAS, 20, 13

Cary, J. R., & Brizard, A. J. 2009, Reviews of Modern Physics, 81, 693

Chen, F. 2010, Introduction to Plasma Physics and Controlled Fusion, ed. Chen, F.

Chupp, E. L., Forrest, D. J., Higbie, P. R., Suri, A. N., Tsai, C., & Dunphy, P. P. 1973, Nature, 241, 333

Cowley, S. W. H. 1978, Planetary Space Science, 26, 539

Dalla, S., & Browning, P. K. 2006, ApJ, 640, L99

Drake, J. F., Shay, M. A., Thongthai, W., & Swisdak, M. 2005, Physical Review Letters, 94, 095001

Ellison, D. C., & Ramaty, R. 1985, ApJ, 298, 400

Fairfield, D. H. 1979, Journal of Geophysical Research, 84, 1950

Fan, Y. 2009, Living Reviews in Solar Physics, 6, 4

Feynman, J., & Martin, S. F. 1995, Journal of Geophysical Research, 100, 3355

Forbes, T. G. 1992, in Lecture Notes in Physics, Berlin Springer Verlag, Vol. 399, IAU Colloq. 133: Eruptive Solar Flares, ed. Z. Svestka, B. V. Jackson, & M. E. Machado, 79

Forbes, T. G., & Priest, E. R. 1987, Reviews of Geophysics, 25, 1583

Foukal, P. V., & Behr, B. B. 1995, Solar Phys., 156, 293

Giovanelli, R. G. 1946, Nature, 158, 81

Gorbachev, V. S., Kelner, S. R., Somov, B. V., & Shvarts, A. S. 1988, Soviet Ast., 32, 308

Gordovskyy, M., Browning, P. K., & Vekstein, G. E. 2010a, A&A, 519, A21

—. 2010b, ApJ, 720, 1603

Güdel, M. 2007, Living Reviews in Solar Physics, 4, 3

Hahm, T. S., & Kulsrud, R. M. 1985, Physics of Fluids, 28, 2412

Hale, G. E. 1908, ApJ, 28, 315

Hannah, I. G., & Fletcher, L. 2006, Solar Phys., 236, 59

Harra, L. K., & Sterling, A. C. 2001, ApJ, 561, L215

Heerikhuisen, J., Litvinenko, Y. E., & Craig, I. J. D. 2002, ApJ, 566, 512

Hey, J. S. 1983, The radio universe (3rd edition)

Heyvaerts, J., Priest, E. R., & Rust, D. M. 1977, ApJ, 216, 123

Hodgson, R. 1859, MNRAS, 20, 15

Holman, G. D. 1985, ApJ, 293, 584

Hoyle, F. 1949, Some recent researches in solar physics.

Hoyng, P., et al. 1981, ApJ, 246, L155

Hudson, H. S. 2011, Space Sci.Rev., 158, 5

Jackson, J. D. 1998, Classical Electrodynamics, 3rd Edition

Jain, R., Browning, P., & Kusano, K. 2005a, in ESA Special Publication, Vol. 596, Chromospheric and Coronal Magnetic Fields, ed. D. E. Innes, A. Lagg, & S. A. Solanki

Jain, R., Browning, P., & Kusano, K. 2005b, Physics of Plasmas, 12, 012904

Jess, D. B., Mathioudakis, M., Browning, P. K., Crockett, P. J., & Keenan, F. P. 2010, ApJ, 712, L111

Karlicky, M. 2008, in European Solar Physics Meeting, Vol. 12, European Solar Physics Meeting, ed. H. Peter, 3

Kiplinger, A. L., Dennis, B. R., Frost, K. J., & Orwig, L. E. 1984, ApJ, 287, L105

Klein, K.-L., & MacKinnon, A. 2007, in Lecture Notes in Physics, Berlin Springer Verlag, Vol. 725, Lecture Notes in Physics, Berlin Springer Verlag, ed. K.-L. Klein & A. L. MacKinnon, 1

Kliem, B. 1994, ApJS, 90, 719

Lang, K. R., ed. 2000, The sun from space

Lin, R. P. 2006, Space Sci.Rev., 124, 233

Litvinenko, Y. E. 1996, ApJ, 462, 997

Litvinenko, Y. E., & Somov, B. V. 1993, Solar Phys., 146, 127

Mandrini, C. H., & Machado, M. E. 1992, Solar Phys., 141, 147

Mann, G., Aurass, H., & Warmuth, A. 2006, A&A, 454, 969

Martin, S. F., Dezso, L., Antalova, A., Kucera, A., & Harvey, K. L. 1982, Advances in Space Research, 2, 39

Masuda, S., Kosugi, T., Hara, H., Tsuneta, S., & Ogawara, Y. 1994, Nature, 371, 495

Masuda, S., Kosugi, T., Tsuneta, S., & Hara, H. 1996, Advances in Space Research, 17, 63

McAllister, A., et al. 1992, PASJ, 44, L205

Melrose, D. B. 1990, Australian Journal of Physics, 43, 703

Miller, J. A., et al. 1997, Journal of Geophysical Research, 102, 14631

Moreton, G. F. 1964, AJ, 69, 145

Mullan, D. 2010, Physics of the Sun:A First Course, ed. Basu, D.

Nakariakov, V. M., & Verwichte, E. 2005, Living Reviews in Solar Physics, 2, 3

Ness, N. F. 1965, Journal of Geophysical Research, 70, 2989

Northrop, T. G. 1966, in Astrophysics and Space Science Library, Vol. 5, Radiation Trapped in the Earth's Magnetic Field, ed. B. M. McCormac, 26

Oka, M., Phan, T.-D., Krucker, S., Fujimoto, M., & Shinohara, I. 2010, ApJ, 714, 915

Parker, E. N. 1979, Cosmical magnetic fields: Their origin and their activity

—. 1988, ApJ, 330, 474

Peterson, L. E., & Winckler, J. R. 1959, Journal of Geophysical Research, 64, 697

Petkaki, P., & MacKinnon, A. L. 2007, A&A, 472, 623

Petrosian, V., Yan, H., & Lazarian, A. 2006, ApJ, 644, 603

Petschek, H. E. 1964, NASA Special Publication, 50, 425

Piana, M., Massone, A. M., Kontar, E. P., Emslie, A. G., Brown, J. C., & Schwartz, R. A. 2003, ApJ, 595, L127

Priest, E., & Forbes, T., eds. 2000, Magnetic reconnection : MHD theory and applications

Ramaty, R., & Murphy, R. J. 1987, Space Sci.Rev., 45, 213

Sato, T., & Hayashi, T. 1979, Physics of Fluids, 22, 1189

Sato, T., Matsumoto, H., & Nagai, K. 1982, Journal of Geophysical Research, 87, 6089

Schindler, K. 2010, Physics of Space Plasma Activity

Schlickeiser, R., & Miller, J. A. 1998, ApJ, 492, 352

Schmidt, G. 1979, Physics of high temperature plasmas /2nd edition/

Scholer, M. 1989, Journal of Geophysical Research, 94, 8805

Schrijver, C. J., & Siscoe, G. L. 2009, Heliophysics: Plasma Physics of the Local Cosmos, ed. Schrijver, C. J. & Siscoe, G. L. (Cambridge University Press)

Shibata, K., & Magara, T. 2011, Living Reviews in Solar Physics, 8, 6

Shibata, K., Masuda, S., Shimojo, M., Hara, H., Yokoyama, T., Tsuneta, S., Kosugi, T., & Ogawara, Y. 1995, ApJ, 451, L83

Shiota, D., Isobe, H., Chen, P. F., Yamamoto, T. T., Sakajiri, T., & Shibata, K. 2005, ApJ, 634, 663

Siversky, T. V., & Zharkova, V. V. 2009, Journal of Plasma Physics, 75, 619

Sonnerup, B. U. Ö. 1971, Journal of Geophysical Research, 76, 8211

Speiser, T. W. 1965, Journal of Geophysical Research, 70, 4219

Sterling, A. C., & Hudson, H. S. 1997, ApJ, 491, L55

Tsiklauri, D., & Haruki, T. 2007, Physics of Plasmas, 14, 112905

Tsuneta, S. 1996, ApJ, 456, 840

Tsuneta, S., Hara, H., Shimizu, T., Acton, L. W., Strong, K. T., Hudson, H. S., & Ogawara, Y. 1992a, PASJ, 44, L63

Tsuneta, S., & Naito, T. 1998, ApJ, 495, L67

Tsuneta, S., Takahashi, T., Acton, L. W., Bruner, M. E., Harvey, K. L., & Ogawara, Y. 1992b, PASJ, 44, L211

Ugai, M., & Tsuda, T. 1977, Journal of Plasma Physics, 17, 337

Vekstein, G. E., & Jain, R. 1998, Physics of Plasmas, 5, 1506

Veronig, A. M., Karlický, M., Vršnak, B., Temmer, M., Magdalenić, J., Dennis, B. R., Otruba, W., & Pötzi, W. 2006, A&A, 446, 675

Watanabe, T., et al. 1992, PASJ, 44, L199

Wood, P., & Neukirch, T. 2005, Solar Phys., 226, 73

Yan, X.-L., Qu, Z.-Q., & Kong, D.-F. 2011, MNRAS, 414, 2803

Yashiro, S., Gopalswamy, N., Michalek, G., St. Cyr, O. C., Plunkett, S. P., Rich, N. B., & Howard, R. A. 2004, Journal of Geophysical Research (Space Physics), 109, 7105

Zharkova, V. V., & Gordovskyy, M. 2004, ApJ, 604, 884

Zhu, Z., & Parks, G. 1993, Journal of Geophysical Research, 98, 7603

Zwaan, C. 1985, Solar Phys., 100, 397